Clays and Clay Minerals, Vol. 61, No. 1, 34–56, 2013.

WEATHERING OF ALMANDINE GARNET: INFLUENCE OF SECONDARY MINERALS ON THE RATE-DETERMINING STEP, AND IMPLICATIONS FOR REGOLITH-SCALE Al MOBILIZATION

JASON R. PRICE[1,*], DEBRA S. BRYAN-RICKETTS[2,3], DIANE ANDERSON[1,4], AND MICHAEL A. VELBEL[2]

[1] Department of Earth Sciences, P.O. Box 1002, Millersville University, Millersville, PA 17551-0302, USA
[2] Department of Geological Sciences, 206 Natural Science Building, Michigan State University, East Lansing, Michigan 48824-1115, USA
[3] Environmental Protection Division, Los Alamos National Laboratory, Box 1663, Los Alamos, NM 87544, USA
[4] Celerity, 4720 Gettysburg Rd., Suite 204, Mechanicsburg, PA 17055, USA

Abstract—Secondary surface layers form by replacement of almandine garnet during chemical weathering. This study tested the hypothesis that the kinetic role of almandine's weathering products, and the consequent relationships of primary-mineral surface texture and specific assemblages of secondary minerals, both vary with the solid-solution-controlled variations in Fe and Al contents of the specific almandine experiencing weathering.

Surface layers are protective (PSL) when the volume of the products formed by replacement is greater than or equal to the volume of the reactants replaced. Under such circumstances, reaction kinetics at the interface between the garnet and the replacing mineral are transport controlled and either transport of solvents or other reactants to, or products from, the dissolving mineral is rate limiting. Beneath PSLs, almandine garnet surfaces are smooth, rounded, and featureless. Surface layers are unprotective (USL) when the volume of the products formed by replacement is less than the volume of the reactants replaced. Under such circumstances, reaction kinetics at the interface between the garnet and the replacing mineral are interface controlled and the detachment of ions or molecules from the mineral surface is rate limiting. Almandine garnet surfaces beneath USLs exhibit crystallographically oriented etch pits. However, contrary to expectations, etch pits occur on almandine garnet grains beneath some layers consisting of mineral assemblages consistent with PSLs.

Based on the Pilling-Bedworth criterion, surface layers are more likely to be protective over a broad range of reactant-mineral compositions when they contain goethite, kaolinite, and pyrolusite. However, this combination requires specific ranges of Fe and Al content of the natural reacting almandine garnet. To form a PSL of goethite and kaolinite, an almandine garnet must have a minimum Al stoichiometric coefficient of ~3.75 a.p.f.u., and a minimum Fe stoichiometric coefficient of ~2.7 a.p.f.u.

Product minerals also influence the mobility of the least-mobile major rock-forming elements. A PSL consisting of goethite, gibbsite, and kaolinite yields excess Al for export during almandine garnet weathering. As the quantity of kaolinite present in the PSL decreases, the amounts of Al available for export increases.

Key Words—Almandine Garnet, Chemical Weathering, Coweeta Hydrologic Laboratory, Gibbsite, Goethite, Hematite, Kaolinite, Protective Surface Layers, Saprolite, Unprotective Surface Layers.

INTRODUCTION

Weathering products are widely believed to exert an influence on the rates and mechanisms of primary-mineral weathering (Berner, 1978, 1981; Velbel, 1984a, 1993). However, specific examples of relationships between individual product minerals and distinctive alteration textures indicative of particular weathering mechanisms are not common. This is especially true when different weathering products are associated with different alteration textures. For example, denticulated (sawtooth, hacksaw, or 'cockscomb') terminations on naturally weathered pyroxenes and amphiboles appear identical regardless of whether the weathering product being formed is a 2:1 clay or an assemblage of hydroxides (*e.g.* Velbel, 1989, 2007; Velbel and Barker, 2008; Velbel *et al.*, 2009). These same textures also occur regardless of whether the environment of alteration is pedogenic or burial diagenetic (*e.g.* Berner *et al.*, 1980; Velbel, 2007).

Previous workers have reported almandine garnet weathering to various products, including gibbsite, goethite, and hematite (Embrechts and Stoops, 1982; Parisot *et al.*, 1983; Velbel, 1984a; Graham *et al.*, 1989a,b; Robertson and Butt, 1997). Additional studies have reported a great variety of garnet surface textures on both naturally weathered (Embrechts and Stoops, 1982; Parisot *et al.*, 1983; Velbel, 1984a, Ghabru *et al.*, 1989; Robertson and Butt, 1997) and diagenetically altered (Hansley, 1987; Salvino and Velbel, 1989) grains.

* E-mail address of corresponding author:
Jason.Price@millersville.edu
DOI: 10.1346/CCMN.2013.0610104

Velbel (1993) hypothesized that during subaerial weathering, the formation of surface layers composed of gibbsite and goethite should have different kinetic consequences and produce different dissolution and replacement textures than surface layers composed of gibbsite and hematite. A surface layer composed of gibbsite and goethite formed by replacement of almandine garnet is predicted to have a volume greater than the volume of the parent almandine garnet replaced (Velbel, 1993). In such a scenario the surface layer has negligible porosity. Negligible porosity requires that transport of soluble species to or from the almandine's surface is restricted to grain-boundary diffusion between product-mineral crystals or volume diffusion through the product-mineral crystal structures. Such a layer thereby inhibits continued garnet dissolution. Reaction kinetics in which the rate-determining process is diffusion of mobile reactant or product species through the medium surrounding the primary mineral are referred to as transport-controlled or transport-limited kinetics, and primary-mineral surfaces affected by transport-limited kinetics are smooth and rounded (Berner, 1978). Solid material through which diffusion is rate limiting is referred to as a protective surface layer (Velbel, 1993; abbreviated herein as PSL). Following previous work using the Pilling-Bedworth criterion, Velbel (1993) defined a surface layer as being protective when the volume of the product(s) formed by replacement of a primary mineral is greater than or equal to the volume of the reactant mineral replaced ($V_p/V_r \geqslant 1$). In contrast, a surface layer composed of gibbsite and hematite formed by replacement of almandine garnet will have a volume significantly less than the volume of the parent almandine garnet replaced (Velbel, 1993) ($V_p/V_r < 1$). In such a scenario the resulting high porosity in, and/or cracks and other voids through, the surface layer allow movement of solvent and solutes to and from the reacting almandine garnet surface. The surface layer has no restricting effect of solvent on solute transport, and does not protect the primary-mineral surface from access by mobile species. Reaction kinetics in which the rate-determining process is reaction at the interface (slower than diffusion of mobile reactant or product species through the medium surrounding the primary mineral) are referred to as surface-controlled or interface-limited kinetics. Primary-mineral surfaces affected by surface-controlled kinetics exhibit crystallographically controlled etch pits (Berner, 1978). A layer of products with these characteristics is referred to here as an unprotective surface layer (USL).

Four tests exist for distinguishing transport-limited from interface-limited kinetics (Berner, 1978) but three apply only to laboratory experiments. Examination of primary-mineral surfaces for smooth or pitted surfaces is the only one of the four tests that can be applied to naturally weathered mineral grains as well as experimental kinetic data (Velbel, 2004). Velbel (1993) tested the hypothesis that different combinations of secondary Fe- and Al-bearing minerals have different consequences for mineral–water reaction kinetics and primary-mineral surface textures. He found broad agreement between the product-reactant volume ratios (V_p/V_r) and textural observations. Specifically, of the major rock-forming silicates, only almandine garnet exhibited both kinetic mechanisms. The product-reactant volume ratios indicated that gibbsite-goethite layers which had been reported by previous workers (*e.g.* Velbel, 1984b, and references therein) formed PSLs over smooth almandine surfaces in saprolites beneath soils. In contrast, products were absent from etched surfaces in soils. Both phenomena had been reported by previous workers; *e.g.* Velbel, 1984b, and references therein. The amount (volume) of product that can be formed upon replacement of a primary mineral by its secondary weathering products depends on the abundances of product-forming elements in the primary mineral. Therefore, the product volume varies with compositional variations in the primary mineral due to elemental substitution in solid-solution. To date Velbel's (1993) hypothesis has not been extended beyond end-member compositions of natural almandine garnets.

The purpose of this study was to test the hypothesis that the kinetic role of almandine garnet's weathering products varies with the composition of the specific almandine experiencing weathering. This hypothesis is tested by calculating the product-reactant volume ratios for natural almandine garnets from Coweeta Hydrologic Laboratory (CHL) in western North Carolina, USA, using the Pilling-Bedworth criterion (Velbel, 1993). In support of this, the formation and nature of surface layers on naturally occurring almandine garnets, including observations of underlying garnet surface textures, are initially characterized. Second, the possible temporal changes in surface layer mineralogy are considered based on the surface textures of naturally weathered almandine garnets in the observational portion of the study. Finally, the possibility of exporting Al derived during almandine garnet surface layer formation, as a function of the different secondary minerals in the surface layer, is presented following work by Velbel *et al.* (2009). Aluminum budgets for the system are determined from the stoichiometric coefficients of Al and Fe in the parent almandine garnet and secondary PSL minerals. Production of PSLs and, subsequently, possible excess Al available for export is a function of the primary almandine garnet's Al and Fe stoichiometric coefficients, molar mass, and specific gravity.

BACKGROUND

Previous work

The rate-determining step of the hydrolysis of silicate minerals during chemical weathering may occur by one of three mechanisms: (1) transport control in which

either transport of solvents and/or other reactants to, or products from, the dissolving mineral is rate limiting; (2) reaction-, surface-, or interface-control whereby the detachment of ions or molecules from the mineral surface is rate limiting; or (3) a combination of transport- and interface-control (Berner, 1978, 1981; Blum and Lasaga, 1987; Schott and Petit, 1987; Velbel, 2004). In pure transport-controlled dissolution, ions are detached so rapidly from the surface of a crystal that they become concentrated in the solution adjacent to the mineral surface (Berner, 1978, 1981). As a result, dissolution is regulated by transport of these ions *via* advection or diffusion away from the mineral surface. Transport-controlled kinetics includes reactions whose rates are limited by diffusion through a 'leached' layer. The surfaces of minerals dissolving by transport control are smooth, rounded, and featureless (Berner, 1978, 1981; Velbel, 2004). In contrast, during pure interface-controlled dissolution, ion detachment from the mineral surface is so slow that the relatively rapid transport of solutes away from the mineral prevents an increase in ion concentration adjacent to the crystal surface (Berner, 1978, 1981; Schott and Petit, 1987). Under such circumstances, increased advection or diffusion away from the mineral surface has no effect on the dissolution rate (Berner, 1978, 1981). Interface-limited mechanisms result in etch pit formation on mineral surfaces, reflecting the site-selective nature of the interfacial reaction (Wilson, 1975; Berner and Holdren, 1977; 1979; Berner, 1978, 1981; Berner *et al.*, 1980; Berner and Schott, 1982; Brantley *et al.* 1986; Lasaga and Blum, 1986; Blum and Lasaga, 1987). Interface-limited kinetics are now widely accepted for most major rock-forming silicates, including feldspars, pyroxenes, amphiboles, and olivine (Velbel, 1993; Blum and Stillings, 1995; Brantley and Chen, 1995; Brantley, 2005, 2008; Lüttge and Arvidson, 2008).

Velbel (1984a, 1993) described almandine garnet replacement textures and the formation of PSLs developed during chemical weathering. Velbel (1993) determined that protective surface layers can only form if: (1) the immobile elements (*e.g.* Al and Fe) behave conservatively at the scale of the garnet-grain surface; and (2) the volume of product(s) formed during weathering are equal to or greater than the volume of the reacting garnet replaced. Velbel (1984a, 1993) suggested that an almandine with a PSL composed of goethite and gibbsite would experience diffusion-limited dissolution. That is, the rate-determining step during weathering reflects transported-controlled kinetics in the form of diffusion of ions through the PSL, with diffusion being the slowest form of transport (Berner, 1978, 1981). The almandine garnet grains that develop PSLs weather more slowly than the grains which do not (Embrechts and Stoops, 1982; Velbel, 1984a). Almandine garnet surfaces beneath the PSL are smooth and featureless, with rounding of grain corners, reflecting uniform attack on the surface (Berner, 1978, 1981). In contrast, if the surface layer is significantly permeable and unprotective (USL), then diffusion through the open pore network is not sufficiently slow to affect garnet dissolution. Under such circumstances, interface-controlled kinetics is favored with the rate-determining step being processes occurring at the mineral–solution interface, and etch pits form (Berner, 1978, 1981).

Velbel's (1984a, 1993) work on almandine garnet weathering reflects observations for the regolith of the Appalachian Southern Blue Ridge Physiographic Province, USA. In addition to goethite and gibbsite weathering products identified by Velbel (1984a, 1993), hematite has also been observed (Graham *et al.*, 1989a, 1989b, 1990a, 1990b). To date, hematite, goethite, and gibbsite are the only weathering products for almandine garnet reported for the Southern Blue Ridge (Graham *et al.*, 1989a, 1989b, 1990a, 1990b; Velbel 1984a, 1984b, 1993). Despite the release of Si and Al during almandine dissolution, no studies to date have identified kaolinite as a weathering product.

The formation of USLs on hornblende in the Southern Appalachian Blue Ridge Mountains of northeastern Georgia, USA, was investigated by Velbel *et al.* (2009). From hornblende-product molar volume calculations, these authors found that Al must be imported to the hornblende-surface layer system during early-stage weathering. Although Al is typically considered negligibly mobile during weathering, some previous work identified instances of substantial Al mobilization (*e.g.* Gardner, 1992). Velbel *et al.* (2009) suggested that the source of the imported Al in the weathering products of hornblende they studied is from garnet weathering known to occur in the same rock unit. For the textbook end-member almandine garnet composition, Velbel (1993) showed that a PSL may form while up to 15% of the Al and Fe produced during almandine garnet dissolution may be exported from the almandine garnet-PSL microenvironment.

Study area

The study area is the U.S. Forest Service Coweeta Hydrologic Laboratory (CHL) located in the southeastern Blue Ridge Physiographic Province of western North Carolina (Figure 1). The Coweeta Basin is underlain by amphibolite-facies metamorphosed sediments of the Coweeta Group (mid-Ordovician; Miller *et al.*, 2000) and the Otto Formation (Upper Precambrian; Hatcher 1980, 1988). The Coweeta Group is subdivided into three lithostratigraphic units. The basal Persimmon Creek Gneiss is predominantly a massive quartz diorite orthogneiss with interlayers of metasandstone, quartz-feldspar gneiss, and pelitic schist (Hatcher, 1980). The overlying Coleman River Formation is characterized by metasandstone and quartz-feldspar gneiss with lesser pelitic schist and calc-silicate quartzite. The Coleman River Formation is overlain by the Ridgepole Mountain

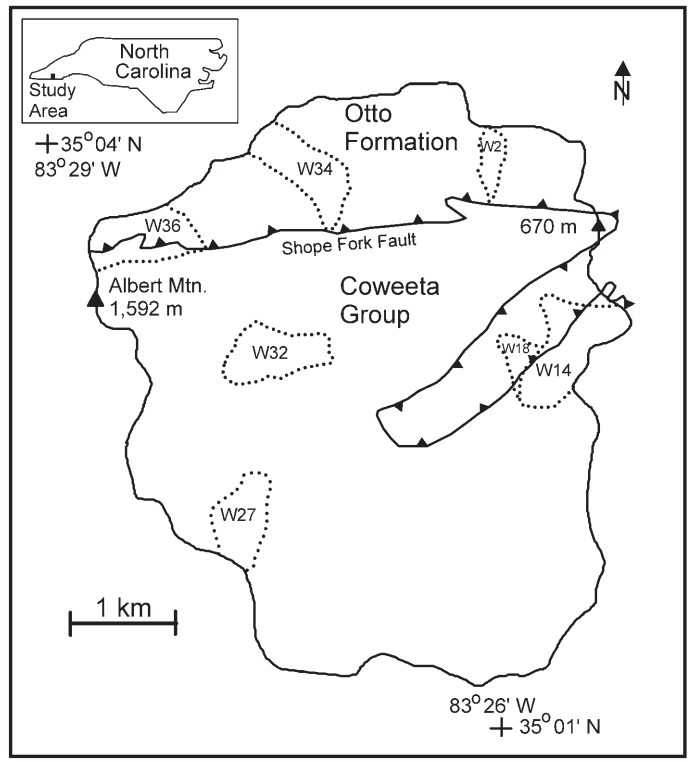

Figure 1. Map of Coweeta Hydrologic Laboratory showing the locations of control watersheds.

Formation; a mineralogically more mature coarse biotite-garnet schist, pelitic schist, metaorthoquartzite, garnetiferous metasandstone, and muscovite-chlorite quartzite (Hatcher, 1980). In contrast to the maturity of the Coweeta Group protolith sediments (*e.g.* arkoses and quartz arenites), the Otto Formation is derived from sedimentary protoliths of low compositional maturity (*e.g.* greywackes) and is feldspar- and biotite-rich (Hatcher, 1980, 1988).

The average weathering profile (saprolite and soil) at Coweeta is ~6 m thick (Berry, 1976; Yeakley *et al.*, 1998). The saprolite at Coweeta is not an ancient, relict, deep weathering profile, as shown by its great thickness (up to 18 m; Berry, 1976; Ciampone, 1995) despite residing on very steep slopes (average slope of ~45%/23°; Velbel, 1985). On such steep slopes, ancient weathering profiles would probably have succumbed to mass wasting and not have survived to the present. Coweeta soils are mostly Ultisols and Inceptisols (Velbel, 1988). Coweeta soils are typically limited in thickness to the uppermost 30 cm of the profile and differ from the underlying saprolite in that they are friable and the residual parent rock structure and fabric have been destroyed by soil forming processes, including transformation or neoformation of soil minerals, mass-wasting, slope creep, root throw, and bioturbation (Velbel, 1985). Soil textures range from fine/coarse loamy, micaceous to fine/coarse loamy, mixed (Browning and Thomas, 1985) and most Coweeta soils are well to extremely well drained. Umbric Dystrochrepts occur at high elevations on steep, rocky north- and south-facing slopes, Typic Dystrochrepts occur on south-facing slopes underlain by the Otto Formation, and Typic Haplumbrepts (Inceptisols) occur on colluvium in hollows and coves. Ultisols have formed in residuum of weathered schists and gneisses and include Typic Hapludults and Humic Hapludults. Typic Hapludults are the most prevalent soil type at Coweeta and are found on sloping ridges and side slopes. Humic Hapludults are found on cooler, steep, north-facing slopes (Swank and Crossley, 1988).

METHODS

Application of the Pilling-Bedworth Rule

The Pilling-Bedworth method was established by metallurgists to explain and predict oxidation products on metals (*e.g.* Kubaschewski and Hopkins, 1962; Hauffe, 1965). Velbel (1993) and Velbel *et al.* (2009) adapted the criterion for application to the chemical weathering of silicate minerals and their possible secondary products, including garnets. The Pilling-Bedworth rule may be important for reaction products in which diffusion of matter is from the outer surface of the product toward the metal–product interface (Kubaschewski and Hopkins, 1962; Fromhold, 1976).

This geometry is analogous to observed centripetal garnet replacement textures characterized by Velbel (1984a, 1993).

The Pilling-Bedworth criterion applied to the weathering of rock-forming minerals involves calculation of the ratio of the volume of the secondary weathering products (V_p) replacing a primary weathering mineral to the volume of primary mineral replaced (V_r). When $V_p/V_r \geqslant 1$, the surface layer of secondary minerals will occupy at least the same volume as the portion of the reactant mineral replaced. Such a surface layer is pore free and thus a PSL (Kubaschewski and Hopkins, 1962; Hauffe, 1965; Velbel, 1993). Diffusion through a PSL (by grain-boundary diffusion between product-mineral crystals or volume diffusion through the product-mineral crystal structures) is rate determining for the chemical weathering of the reactant mineral. With a PSL the kinetics of the weathering primary mineral are transport- (diffusion)-limited, the mineral grains exhibit sharp, smooth contact with the PSL, and primary grain edges and corners become rounded (Velbel, 1984a, 1993). When $V_p/V_r < 1$, the surface layer of secondary minerals is of insufficient volume to be continuous and uninterrupted, and is, therefore, an USL. An USL yields a primary mineral surface that is vulnerable to direct attack by reacting fluids. Also, with an USL the kinetics of the weathering primary mineral are interface limited, and the mineral grains exhibit etched surfaces (Velbel, 1984a, 1993).

Following the Pilling-Bedworth criterion, as presented by Velbel (1993), the total number of moles of a given element (e) in any arbitrary volume of reactant or product mineral is given by

$$m_{e,i} = \frac{n_{e,i} V_i}{V_i^o} \quad (1)$$

where,

$m_{e,i}$ = total number of moles of element e in mineral i

$n_{e,i}$ = stoichiometric coefficient of element e in mineral i

V_i = volume of mineral i

V_i^o = molar volume of mineral i

Writing equations for i = reactant mineral, r, and for i = product mineral, p, setting $m_{e,r} = m_{e,p}$ (that is, conserving element e such that all of element e present in the reactant mineral is incorporated into the product mineral), and combining the equations for reactant and product minerals, and rearranging, yields:

$$V_p/V_r = \frac{n_{e,r} V_p^o}{n_{e,p} V_r^o} \quad (2)$$

where,

V_p/V_r = the volume of product mineral produced per unit volume of reactant mineral if element e is conserved.

By analogy with the Pilling-Bedworth rule, for a primary rock-forming silicate mineral to form a PSL by replacement, conservation of the least mobile elements such as Fe, Al, and Mn must be assumed (Velbel, 1993).

Molar volumes for reactant garnets (V_r^o) were calculated by dividing the molar mass of a mineral by its specific gravity. In the absence of analytically determined primary-mineral chemistries, molar volumes are available from Smyth and Bish (1988). However, using calculated molar volumes determined from site-specific analyzed mineral chemistries yield more meaningful results for the system being investigated. Molar volumes for secondary products (V_p^o) included in this study (Table 1) are from Smyth and Bish (1988), reported by Velbel (1993, table 1). Secondary products investigated in this study are hematite, goethite, gibbsite, kaolinite, and pyrolusite. These minerals are ubiquitous in the CHL regolith (*e.g.* Velbel, 1984a, 1984b; Price, 2003; Price *et al.*, 2005), and some of these have been reported to be associated with garnet weathering in the southern Appalachian Blue Ridge Physiographic Province (*e.g.* Graham *et al.*, 1989a, 1989b, 1990a, 1990b; Velbel, 1984a, 1984b, 1993) and elsewhere (*e.g.* Embrechts and Stoops, 1982; Parisot *et al.*, 1983; Robertson and Butt, 1997).

Published data for natural almandine garnets

Chemical data from Deer *et al.* (1997) were used to establish a conceptual framework for surface layer formation on natural almandine garnets. These data are ideally suited as Deer *et al.* (1997) not only provide analyses spanning a wide range of natural almandine

Table 1. Stoichiometric coefficients and molar volumes for secondary weathering products characteristic of well leached oxidizing conditions.

Mineral	Formula	Element conserved (e)	n_e	V^o	V^o/n_e
Hematite	Fe_2O_3	Fe	2	30.388	15.194
Goethite	FeOOH	Fe	1	20.693	20.693
Gibbsite	$Al(OH)_3$	Al	1	32.222	32.222
Kaolinite	$Al_2Si_2(OH)_5O_4$	Al	2	99.236	49.618
Pyrolusite	MnO_2	Mn	1	16.708	16.708

Data from Smyth and Bish (1988) and reported by Velbel (1993; his table 1).

garnet compositions, but also include the garnets' specific gravities with many of their chemical analyses. A total of 18 garnet analyses and associated specific gravities (Table 2) were used in the present study.

All surface-layer calculations in this study assumed conservation of Fe in hematite or goethite, and conservation of Al in gibbsite and/or kaolinite (Velbel, 1993; Table 1). For a PSL composed solely of goethite and kaolinite when $V_p/V_r = 1$ the following equation applies:

$$V_r = V_p = Fe_{Grt}V^o_{Gt} + 0.5Al_{Kln}V^o_{Kln} \quad (3)$$

where,

Fe_{Grt} = Fe stoichiometric coefficient of the garnet; assume that all Fe conserved in PSL goethite

V^o_{Gt} = molar volume of goethite

Al_{Kln} = moles of Al in kaolinite of PSL

V^o_{Kln} = molar volume of kaolinite

All subscripts are the standard mineral symbols of Kretz (1983). Rearranging equation 3 yields

$$Al_{Kln} = (V_r - Fe_{Grt}V^o_{Gt})/0.5V^o_{Kln} \quad (4)$$

In order to determine the quantity of Al needed to form a PSL of goethite, gibbsite, and kaolinite when $V_p/V_r = 1$, a gibbsite term must be added to equation 3 as follows:

$$V_r = V_p = Fe_{Gt}V^o_{Gt} + 0.5Al_{Kln}V^o_{Kln} + Al_{Gbs}V^o_{Gbs} \quad (5)$$

where,

Al_{Gbs} = moles of Al in gibbsite of PSL

Rearranging equation 5 yields

$$Al_{Kln} = (V_r - Fe_{Gt}V^o_{Gt} - Al_{Gbs}V^o_{Gbs})/0.5V^o_{Kln} \quad (6)$$

The excess Al available for export is the difference between the number of moles of Al needed to produce a PSL of goethite, gibbsite, and kaolinite when $V_p/V_r = 1$, and the Al stoichiometric coefficient of the parent garnet.

Almandine garnets from Coweeta Hydrologic Laboratory

Three different almandine garnet compositions have been collected from CHL (Figure 1) (Velbel, 1984a, 1984b; Price, 2003; Price *et al.*, 2005), all of which form PSLs during weathering (Velbel, 1984a, 1984b; Bryan, 1994; Price, 2003; Price *et al.*, 2005). Evaluation of these grains permits further exploration of the conceptual framework for surface-layer formation, direct observations of garnet-surface textures, and production of excess Al associated with almandine garnet weathering.

Pilling-Bedworth criterion. The specific gravity of CHL almandine garnets could not be measured so the average of those reported by Deer *et al.* (1997) of 4.05 was used. Calculations were also made using a specific gravity from Klein and Hurlbut (1999) of 4.32. However, the exact specific gravity value used does not appreciably influence the results, and has no influence on the conclusions of this study.

Field sampling and petrography. Almandine garnet samples examined were collected and described by Velbel (1984a, 1984b), Bryan (1994), Price (2003), and Price *et al.* (2005). Parent rock was collected from outcrops, and regolith samples were collected from roadcuts and hand-augered cores. Samples were collected from saprolite (>60 cm below surface grade (b.s.g.)),

Table 2. Almandine garnet analyses from Deer *et al.* (1997) utilized in the present study (n = 18).

Sample	Si	Al	Al	Fe^{3+}	Ti	Mg	Fe^{2+}	Mn	Ca	O	Specific gravity	Molar mass	V_r
3	5.974	0.026	3.879	0.1	0.014	0.917	4.86	0.116	0.07	24	4.235	966	228
11	5.879	0.121	3.872	0.057	0.062	0.951	4.506	0.247	0.277	24	4.09	962	235
12	6.052	0	3.891	0.083	0.081	0.621	4.29	0.295	0.507	24	4.1	959	234
15	5.789	0.211	3.628	0.227	0.143	0.277	4.414	0.399	0.882	24	4.03	980	243
20	5.984	0.016	3.944	0.082	0.002	0.299	4.1	0.297	1.211	24	4.13	965	234
23	5.984	0.016	3.914	0.061	0.012	1.827	3.929	0.049	0.153	24	3.967	935	236
24	5.937	0.063	3.994	0.103	0	1.51	3.808	0.208	0.301	24	4.08	939	230
25	5.901	0.099	3.837	0.13	0.012	0.44	3.943	0.169	1.465	24	4.067	963	237
26	6	0	3.795	0.217	0.007	0.573	3.698	0.597	1.03	24	4.1	962	235
28	5.923	0.077	3.783	0.232	0.004	1.827	3.664	0.084	0.376	24	3.99	936	235
30	5.871	0.129	3.955	0.056	0.024	2.1	3.541	0.154	0.143	24	4.04	926	229
32	5.948	0.052	3.771	0.19	0.044	0.731	3.4	0.078	1.729	24	3.99	948	238
36	5.942	0.058	3.782	0.208	0.011	0.992	3.172	0.044	1.76	24	3.97	941	237
38	5.843	0.157	3.766	0.206	0.015	0.216	3.16	1.571	1.086	24	4.06	978	241
42	5.937	0.063	3.933	0.036	0	1.065	2.751	0.563	1.6	24	3.99	935	234
43	6.017	0	3.866	0.12	0.018	1.782	2.664	0.085	1.361	24	3.93	916	233
44	5.911	0.089	3.686	0.274	0.03	0.513	2.658	2.331	0.485	24	4.14	977	236
48	5.992	0.008	3.614	0.32	0.017	0.539	1.942	1.487	2.048	24	3.971	954	240

middle soil horizons (17−60 cm b.s.g.), and upper soil horizons (0−10 cm b.s.g.). Samples were thin sectioned and examined with polarized-light microscopy with weathering textures being photographed with a 35 mm film camera mounted on a petrographic microscope.

Weathered almandine garnets were hand-picked from the >1 mm fraction of the saprolite and soil samples. Samples were washed with deionized water through a 1 mm sieve and the >1 mm fraction dried at 60ºC for 24 h. Almandine garnet grains from the >1 mm regolith fraction and from rock outcrops were hand picked under a binocular microscope.

X-ray diffractometry (XRD). Separation into the <2 mm size fraction was performed by gravity settling, with the <2 mm size fraction being separated with a pipette, and the aliquots being filtered onto a 0.45 μm Millipore™ filter following rapid-suction mounting techniques (production of oriented mounts; also termed the Millipore™ Filter Transfer Method of Drever (1973); this method was described thoroughly by Moore and Reynolds (1997)). Almandine garnet samples and clay minerals in the <2 μm size fraction were initially analyzed by XRD at Michigan State University utilizing a Philips APD (Automated Powder Diffraction) 3720 X-ray diffractometer equipped with an APD 3521 goniometer, a Philips goniometer with CuKα radiation (35 kV, 20 mA), a 1º divergence slit, a 0.2 mm receiving slit, a 1º anti-scatter slit, and a graphite monochromator on the diffracted beam. Almandine garnet samples were step-scanned for various intervals at 0.05º2θ steps using a counting time of 2 s per step.

Additional scans were completed at Franklin and Marshall College, Lancaster, Pennsylvania, using a fully computer-controlled PANalytical X'Pert Pro XRD. Radiation was CuKα (45 kV, 40 mA), with an automated preprogrammed divergence slit that allowed for a constant sample irradiation length of 10 mm, and a 2º anti-scatter slit. Six detectors operated throughout the scan and the sample was rotated continuously during measurement.

Electron microscopy. Hand-picked almandine garnet grains from one or two intermediate points in each profile were mounted to scanning electron microscopy (SEM) stubs with press-on adhesive tabs designed for SEM work. Whole and fractured (by gentle crushing) garnet grains were prepared in the same manner. Grains prepared in this manner were examined by scanning electron microscopy (SEM) in secondary electron imaging (SEI) mode. Polished thin sections of Coweeta bedrock and regolith were imaged using SEM in backscattered-electron imaging (BEI) mode, and energy-dispersive X-ray spectroscopy (EDS). The SEM stubs were gold-coated, and thin sections were either carbon- or gold-coated. Gold-coating of thin sections was often necessary because carbon-coating did not always provide adequate conductivity to prevent sample charging. Imaging and analyses were performed at Michigan State University's Center for Advanced Microscopy (CAM) using a JEOL JSM-35CF SEM. More than 200 micrographs were taken of garnet weathering textures, with the most informative images included herein. Additional photomicrographs may be found in Bryan (1994).

Electron microprobe phase analyses (EMPA). Electron microprobe analyses of Otto Formation, Coleman River Formation, and Ridgepole Mountain Formation garnets in thin section were completed at the University of Michigan's Electron Microbeam Analysis Laboratory (EMAL), using a wavelength dispersive Cameca SX 100 electron microprobe analyzer. The accelerating voltage and beam current were 15 keV and 10 nA, respectively, and a beam diameter of 2 μm was used. Calibration standards for Si, Al, Mg, Fe, Mn, Ti, and Ca were tanzanite (natural), andalusite (natural), enstatite (synthetic), ferrosilite (synthetic), rhodonite (natural Broken Hill), geikielite (natural), and tanzanite (natural), respectively. All garnet formulae reported in this study were reported on an anion basis of O_{24}.

RESULTS

Application of Pilling-Bedworth rule to naturally occurring almandine garnet compositions

None of the 18 almandine garnet samples reported by Deer *et al.* (1997) would produce a PSL of hematite and gibbsite (Table 3). Hematite has a relatively low molar volume per mole of Fe, with V^o/n_e = 30.388/2 = 15.194 (Table 1). Because goethite has V^o/n_e = 20.693, having goethite as the Fe host is more likely to yield a PSL than one in which hematite is the Fe host. Similarly, kaolinite has a greater V^o/n_e value (49.618) than does gibbsite (32.222) (Table 1). Thus, a surface layer in which kaolinite is the Al host is more likely to be protective than one in which gibbsite is the Al host. The importance of the presence of kaolinite in a surface layer is reflected in the fact that 89% of the almandine garnets (Table 3) could form a PSL composed of hematite and kaolinite, despite hematite being the Fe host. To weather to a PSL of hematite and kaolinite, almandine garnet would have to possess minimum Fe and Al stoichiometric coefficients of ~2.8 a.p.f.u. and ~3.78 a.p.f.u., respectively (anion basis of O_{24}) (Figure 2a). Most of the almandine garnets investigated satisfied this criterion (Table 2). In contrast, only one of the 18 almandine garnet samples (6%) reported by Deer *et al.* (1997) (sample 3) had an appropriate chemistry to produce a PSL of solely goethite and gibbsite (Table 3; Figure 2b). Sample 3 producing a PSL of goethite and gibbsite did so because of the garnet's relatively high Fe stoichiometric coefficient (Table 2). This Fe stoichiometric coefficient is above an approximate minimum of ~4.7 (anion basis of O_{24})

Table 3. Results of surface-layer calculations for garnet compositions and specific gravities, as reported by Deer *et al*. (1997).

Sample	V_p/V_r								Moles of Al needed for $V_p/V_r = 1$ (PSL of goethite + kaolinite)	Excess Al when $V_p/V_r = 1$ (PSL of goethite + kaolinite)
	Hematite + Gibbsite	Hematite + Kaolinite	Goethite + Gibbsite	Goethite + Kaolinite	Hematite + Gibbsite + Pyrolusite	Hematite + Kaolinite + Pyrolusite	Goethite + Gibbsite + Pyrolusite	Goethite + Kaolinite + Pyrolusite		
3	0.88	1.18	1.00	1.30	0.89	1.19	1.01	1.31	2.53	1.38
11	0.84	1.14	0.95	1.24	0.86	1.15	0.97	1.26	2.87	1.12
12	0.82	1.11	0.92	1.21	0.84	1.13	0.94	1.23	2.92	0.97
15	0.80	1.07	0.90	1.18	0.83	1.10	0.93	1.21	3.00	0.84
20	0.82	1.11	0.92	1.21	0.84	1.13	0.94	1.23	2.99	0.97
23	0.79	1.08	0.89	1.18	0.80	1.09	0.89	1.18	3.11	0.82
24	0.83	1.13	0.92	1.23	0.84	1.15	0.93	1.24	3.03	1.02
25	0.80	1.09	0.89	1.18	0.81	1.10	0.90	1.19	3.10	0.84
26	0.77	1.06	0.87	1.15	0.82	1.10	0.91	1.19	3.12	0.67
28	0.78	1.07	0.87	1.16	0.79	1.07	0.88	1.17	3.13	0.73
30	0.81	1.12	0.90	1.21	0.82	1.13	0.91	1.22	3.15	0.94
32	0.75	1.03	0.83	1.11	0.75	1.03	0.84	1.12	3.32	0.51
36	0.74	1.02	0.82	1.10	0.74	1.02	0.82	1.10	3.39	0.45
38	0.74	1.02	0.81	1.10	0.85	1.13	0.92	1.21	3.47	0.45
42	0.73	1.03	0.80	1.09	0.77	1.07	0.84	1.13	3.58	0.42
43	0.72	1.00	0.78	1.07	0.72	1.01	0.79	1.08	3.56	0.31
44	0.70	0.98	0.77	1.05	0.87	1.15	0.94	1.22	3.55	0.22
48	0.63	0.89	0.68	0.94	0.73	0.99	0.78	1.05	Not applicable	
% Forming PSL	0	89	6	94	0	94	6	100		

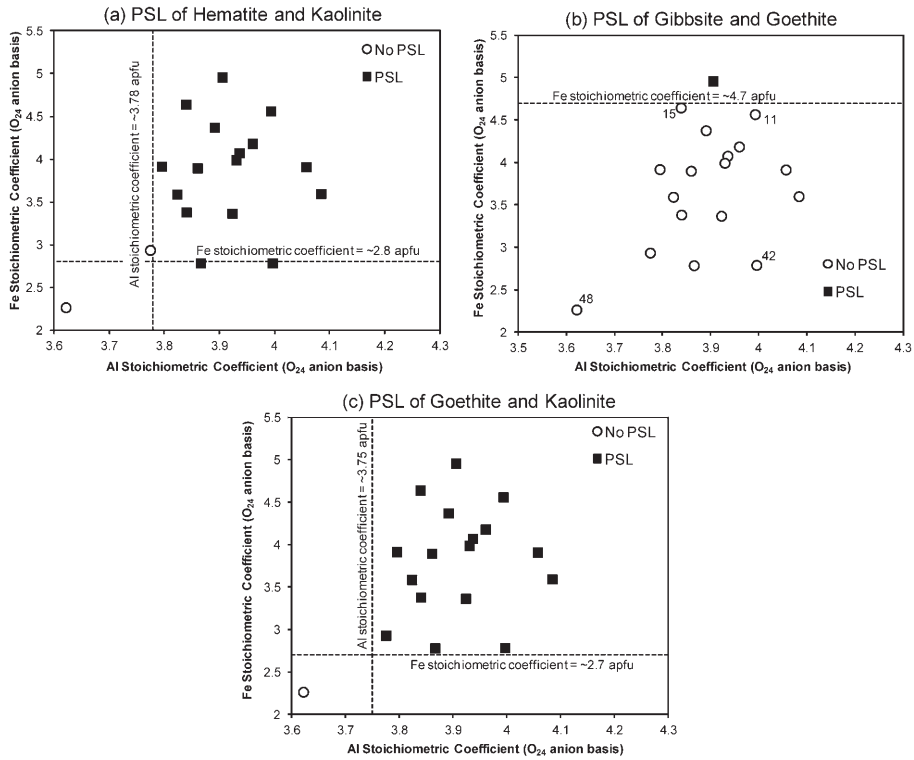

Figure 2. Results of almandine garnet surface-layer calculations for surface layers composed of (a) hematite and kaolinite, (b) goethite and gibbsite, and (c) goethite and kaolinite. 'PSL' indicates that the surface layer is protective, with $V_p/V_r \geqslant 1$. Minimum Fe and Al stoichiometric coefficients needed to produce a PSL are provided.

required for PSL formation (Figure 2b). This is consistent with the V_p/V_r calculations of Velbel (1993) for end-member almandine garnet. Of the remaining samples, all but one (sample 48) would produce a PSL of goethite and kaolinite (Table 3; Figure 2c). This illustrates that formation of PSLs on most naturally occurring almandine garnets requires more complicated combinations of actual primary-mineral compositions and product assemblages than the end-member almandine garnet invoked by Velbel (1993). To form a PSL of goethite and kaolinite an almandine garnet would have to possess a minimum Fe stoichiometric coefficient of ~2.7 a.p.f.u. and a minimum Al stoichiometric coefficient of ~3.75 a.p.f.u. (anion basis of O_{24}) (Figure 2c). These stoichiometric coefficients are only slightly lower than those reported for a PSL composed of hematite and kaolinite (Figure 2a). Adding pyrolusite to the surface layer only increases V_p/V_r to $\geqslant 1$ for one sample (44) when the other product minerals are hematite and kaolinite, and one additional sample (48) when the other product minerals are goethite and kaolinite (Table 3). Therefore, including the volume of pyrolusite formed if Mn behaves conservatively in a surface layer will only modify it from a USL to a PSL for a relatively small number of almandine garnets which host substantial quantities of Mn. However, the only product mineralogy that allows for formation of a PSL on all of the almandine garnets (Table 3) is goethite, kaolinite, and pyrolusite. The influence of the Mn stoichiometric coefficient on formation of PSL is probably far more significant for spessartine garnets which are not evaluated in this study.

All but two of the V_p/V_r values for a surface layer of hematite and kaolinite are >1, and all but one of V_p/V_r values for a surface layer of goethite and kaolinite are >1 (Table 3; Figure 2). V_p/V_r values >1 imply that typically not all of the Fe and/or Al released during garnet weathering is required to be incorporated in the PSL. To address the production of excess Al during almandine garnet weathering (Velbel *et al.*, 2009) and PSL formation, focus was placed on surface layers in which all of the Fe was conserved in the PSL, and the Fe-host was goethite, as this combination had the largest V_p/V_r values (Table 3). Sample 48 had $V_p/V_r < 1$ for a surface layer that included either gibbsite or kaolinite as the Al-host (Table 3) and, thus, has not been included in the evaluation that follows. Using equation 4 above, the minimum number of moles of Al needed to produce a PSL of goethite and kaolinite has been calculated (second to the last column on the right of Table 3). The difference between this value and the Al stoichiometric coefficient of the parent almandine garnet yields the number of moles of Al available for export away from the almandine garnet while the PSL is still preserved (far right column of Table 3). In all 17 samples investigated, the maximum number of moles

of Al in excess of that required for PSL formation with $V_p/V_r = 1$ was substantial, ranging from 0.22 to 1.38.

The moles of Al released by almandine garnet weathering in excess of that needed to form a PSL using equation 4 was based on a PSL consisting of goethite and kaolinite (Table 3). However, XRD analyses of almandine garnet PSLs reported by Velbel (1984a, 1993) from western North Carolina indicated that gibbsite was ubiquitous in the PSL. Equation 6 was used to explore the relative proportions of gibbsite and kaolinite in a PSL at $V_p/V_r = 1$ in which all of the Fe was conserved in goethite. This relationship was investigated using four Deer *et al.* (1997) samples which represented the following parent garnet scenarios: (1) high Al and high Fe stoichiometric coefficients; (2) low Al and high Fe stoichiometric coefficients; (3) low Fe and high Al stoichiometric coefficients; and (4) low Al and low Fe stoichiometric coefficients. The samples used were 11 (high Al and high Fe stoichiometric coefficients), 15 (low Al and high Fe stoichiometric coefficients), 42 (low Fe and high Al stoichiometric coefficients), and 48 (low Al and low Fe stoichiometric coefficients) (Figures 2b, 3). The almandine garnet Fe stoichiometric coefficient exerted a strong influence on the formation of PSLs (Figure 3, Tables 3, 4). A relatively high almandine garnet Fe stoichiometric coefficient is capable of counteracting a relatively low Al stoichiometric coefficient by creating a PSL relatively rich in goethite and/or hematite. Specifically, sample 15 had a relatively high V_p/V_r value despite having a relatively low Al stoichiometric coefficient.

Using equation 6, the relative proportions of Al hosted by gibbsite and kaolinite were included in the PSL for samples 11, 42, and 15 (Table 4, Figure 4). Sample 48 was not included because it does not form a PSL even when kaolinite is substituted for gibbsite in the PSL (Table 3). As the proportion of gibbsite in a PSL increases relative to kaolinite, the quantity of excess Al available for export decreases (Table 4, Figure 4). For sample 11 with a PSL at $V_p/V_r = 1$, when ~0.70 moles of Al were consumed by kaolinite, and 3.30 moles of Al were consumed by gibbsite, the quantity of excess Al available for export was approximately zero (Table 4, Figure 4). Almandine garnets with relatively high Fe and low Al stoichiometric coefficients (*e.g.* sample 15) were capable of yielding more excess Al than an almandine garnet with relatively high Al and low Fe stoichiometric coefficients (*e.g.* sample 42) (Table 4, Figures 2 and 4).

	High Al	Low Al
High Fe	**DHZ Sample: 11** V_p/V_r: High PSL: Goethite + kaolinite Excess Al: High	**DHZ Sample: 15** V_p/V_r: High PSL: Goethite + kaolinite Excess Al: High
Low Fe	**DHZ Sample: 42** V_p/V_r: Intermediate PSL: Goethite + kaolinite Excess Al: Low to intermediate	**DHZ Sample: 48** V_p/V_r: Low PSL: None Excess Al: None

Figure 3. Matrix displaying the relationship of V_p/V_r, PSL formation, and excess Al available for export as a function of parent almandine garnet relative to Al and Fe stoichiometric coefficients.

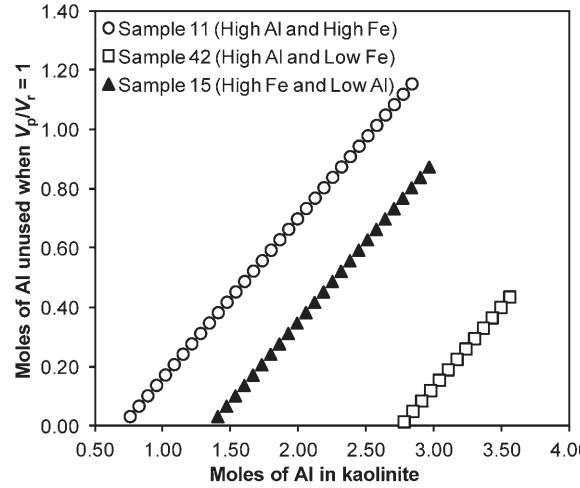

Figure 4. Relationship between Al stoichiometric coefficient of PSL kaolinite and the quantity of excess Al available for export from the almandine garnet-PSL microenvironment. Calculations (Table 4) based on almandine garnet data from Deer *et al.* (1997) (Table 2).

Garnets from Coweeta Hydrologic Laboratory

Mineralogy. Composition data on almandine garnets from the Upper Precambrian Otto Formation and the Mid-Ordovician Coleman River and Ridgepole Mountain Formations are provided in Table 5. X-ray diffractograms of weathered Coweeta almandine garnets displayed peaks indicative of quartz and gibbsite (all samples), hematite (in samples from the warmer, lower elevation Watershed 2), and goethite (in samples from Watersheds 18, 34, and 36) (Bryan, 1994). With the exception of hematite, these results compare favorably with those reported by Velbel (1984a, 1985, 1993). X-ray diffractograms generated as part of this study also yielded peaks for the aforementioned minerals, but also displayed peaks for kaolinite and pyrolusite (Figure 5). Consistent with Bryan (1994), hematite peaks for the Watershed 2 sample (Otto Formation) were taller, sharper, and generally more evident than those for the Watershed 27 sample (Coleman River Formation) (Figures 1 and 5). The same trend was observed for kaolinite.

Pilling-Bedworth Calculations. The methods and Pilling-Bedworth-based concepts outlined above may be applied to almandine garnets found at CHL (Table 5). The results for the CHL garnets are very comparable to

Table 4. Calculations of excess Al available for export for almandine garnet samples, taken from Deer *et al*. (1997).

– 11 (High Al and high Fe) –			– 42 (High Al and low Fe) –			– 15 (High Fe and low Al) –		
Al_{Gbs}	Al_{Kln}	Excess Al when $V_p/V_r = 1$	Al_{Gbs}	Al_{Kln}	Excess Al when $V_p/V_r = 1$	Al_{Gbs}	Al_{Kln}	Excess Al when $V_p/V_r = 1$
0.00	2.84	1.15	0.00	3.56	0.43	0.00	2.97	0.87
0.10	2.77	1.12	0.10	3.50	0.40	0.10	2.90	0.84
0.20	2.71	1.08	0.20	3.43	0.36	0.20	2.84	0.80
0.30	2.64	1.05	0.30	3.37	0.33	0.30	2.77	0.77
0.40	2.58	1.013	0.40	3.30	0.29	0.40	2.71	0.73
0.50	2.51	0.978	0.50	3.24	0.26	0.50	2.64	0.70
0.60	2.45	0.943	0.60	3.17	0.22	0.60	2.58	0.66
0.70	2.38	0.908	0.70	3.11	0.19	0.70	2.51	0.63
0.80	2.32	0.873	0.80	3.04	0.15	0.80	2.45	0.59
0.90	2.25	0.838	0.90	2.98	0.12	0.90	2.38	0.56
1.00	2.19	0.803	1.00	2.91	0.08	1.00	2.32	0.52
1.10	2.13	0.768	1.10	2.85	0.05	1.10	2.25	0.49
1.20	2.06	0.733	1.20	2.78	0.01	1.20	2.19	0.45
1.30	2.00	0.698	1.30	2.72	−0.02	1.30	2.12	0.42
1.40	1.93	0.663		1.40	2.06	0.38		
1.50	1.87	0.628		1.50	1.99	0.35		
1.60	1.80	0.593		1.60	1.93	0.31		
1.70	1.74	0.558		1.70	1.86	0.28		
1.80	1.67	0.522		1.80	1.80	0.24		
1.90	1.61	0.487		1.90	1.73	0.21		
2.00	1.54	0.452		2.00	1.67	0.17		
2.10	1.48	0.417		2.10	1.60	0.14		
2.20	1.41	0.382		2.20	1.54	0.10		
2.30	1.35	0.347		2.30	1.47	0.07		
2.40	1.28	0.312		2.40	1.41	0.03		
2.50	1.22	0.277		2.50	1.34	0.00		
2.60	1.15	0.242						
2.70	1.09	0.207						
2.80	1.02	0.172						
2.90	0.96	0.137						
3.00	0.89	0.102						
3.10	0.83	0.067						
3.20	0.76	0.032						
3.30	0.70	−0.003						

those of Deer *et al.* (1997) in that the formation of a PSL is very uncommon when the surface layer is composed solely of hematite and gibbsite, or solely of goethite and gibbsite (Table 6). However, a PSL did form in two of three garnets when composed of hematite and kaolinite, and all of the CHL garnets formed a PSL composed of goethite and kaolinite. When V_p/V_r values were above unity, excess Al was available for export. With the exception of the Ridgepole Mountain Formation, adding pyrolusite to a surface layer composed of hematite and kaolinite was insufficient to increase product volume to render an otherwise unprotective layer protective (Table 6). Calculations may also be made when Fe is conserved in goethite and V_p/V_r values are thereby highest, and Al is distributed between gibbsite and kaolinite in a PSL when $V_p/V_r = 1$. The results of these calculations demonstrate that the CHL garnets can possess a PSL of goethite, gibbsite, and kaolinite, and still have significant Al available for export (Table 7, Figure 6). For the Otto Formation garnet, no excess Al will be present when approximately equal molar quantities of Al (~2.0) are distributed between gibbsite and kaolinite (Table 7). Garnet of the Coleman River Formation would have more of the Al hosted by gibbsite than kaolinite when excess Al is zero. The Otto Formation and Coleman River Formation have identical Al stoichiometric coefficients, nearly identical molar masses, and the same specific gravity is used for garnets from both bedrock units. The higher excess Al for the Coleman River Formation reflects its higher Fe stoichiometric coefficients relative to that of the Otto Formation (Table 5). This again illustrates the strong influence of Fe stoichiometry on PSL formation and excess Al when all of the Fe is conserved in a weathering product. The Ridgepole Mountain Formation garnet has the lowest stoichiometric coefficients of both Al and Fe, and would require a PSL relatively rich in kaolinite to yield any excess Al (Table 7).

Table 5. Data on garnets collected from Coweeta Hydrologic Laboratory. Mineral chemistry for the Otto Formation and the Coleman River Formation from Price *et al.* (2005). Specific gravity reflects an average of 18 samples reported by Deer *et al.* (1997).

Rock unit	Age	Si	Al	Fe	Mg	Mn	Ca	O	Specific gravity	Molar mass	V_r
Otto Formation	Upper Precambrian	6	4	3.52	0.72	1.0	0.82	24	4.05	962	238
Coleman River Formation	Mid-Ordovician	6	4	4.26	0.88	0.44	0.60	24	4.05	968	239
Ridgepole Mountain Formation	Mid-Ordovician	6	3.72	2.82	0.74	0.9	1.74	24	4.05	948	234

Table 6. Results of surface-layer calculations for Coweeta Hydrologic Laboratory almandine garnets.

	V_p/V_r							
Rock unit	Hematite + Gibbsite	Hematite + Kaolinite	Goethite + Gibbsite	Goethite + Kaolinite	Hematite + Gibbsite + Pyrolusite	Hematite + Kaolinite + Pyrolusite	Goethite + Gibbsite + Pyrolusite	Goethite + Kaolinite + Pyrolusite
Otto Formation	0.77	1.06	0.85	1.14	0.84	1.13	0.92	1.21
Coleman River Formation	0.81	1.10	0.91	1.20	0.84	1.13	0.94	1.23
Ridgepole Mountain Formation	0.70	0.97	0.76	1.04	0.76	1.04	0.83	1.10

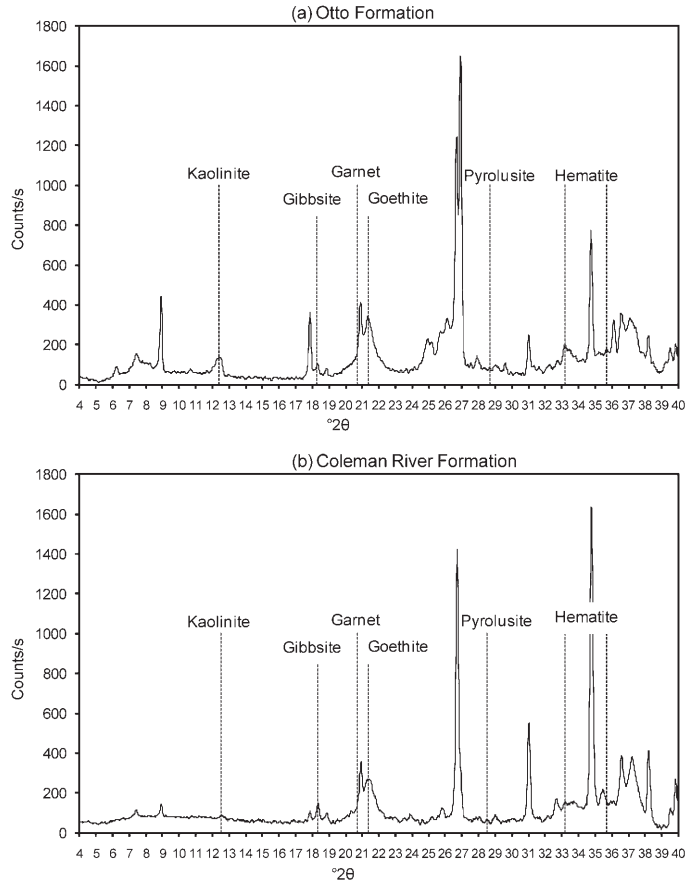

Figure 5. XRD patterns for hand-picked weathered garnet grains from Coweeta regolith. The unlabeled larger peaks include micas (10 Å) and their weathering products and quartz, all of which may be intergrown with garnet grains. Otto Formation samples W2-10, and Coleman River Formation sample W27-7.

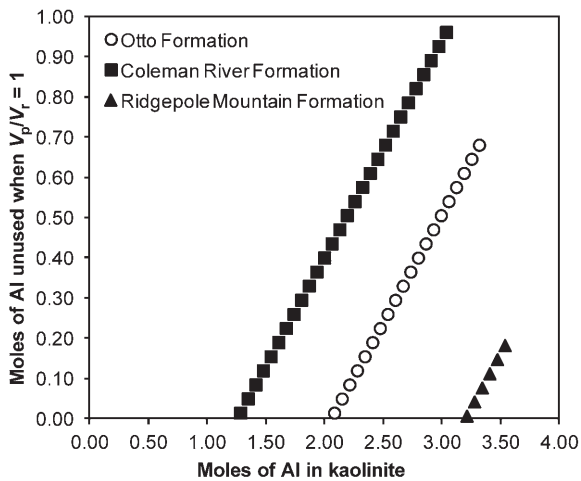

Figure 6. Relationship between Al stoichiometric coefficient of PSL kaolinite and the quantity of excess Al available for export from the almandine garnet-PSL microenvironment for almandine garnets at the Coweeta Hydrologic Laboratory (Table 7).

Energy-dispersive X-ray spectra for CHL almandine garnet from the Otto Formation (Figures 7 and 8) revealed that Si is present in all PSL EDS spectra, probably reflecting the presence of kaolinite identified by XRD (Figure 5). The relative abundance of Si varies depending on the sample and location of the analysis, but variation in brightness of the PSL in a backscattered-electron image indicated that the PSL was not mineralogically homogeneous (Figure 8).

The influence of pyrolusite (Figure 5) on the protectiveness of a surface layer was demonstrated for Coweeta garnets (Table 8). The presence of pyrolusite in the PSL reduces the percentage of Al needing to be hosted by kaolinite by up to 46% (for the Otto Formation; Table 8). Therefore, while pyrolusite in a surface layer may not greatly increase the likelihood of the layer being protective, the presence of pyrolusite does significantly decrease the quantity of kaolinite needed to make a surface layer protective.

Micromorphology of garnets and their surface layers. Garnet grains from CHL exhibited a variety of textures and shapes in thin section. Most garnet grains were

Table 7. Calculations of excess Al (a.p.f.u.) available for export for almandine garnet samples collected at Coweeta Hydrologic Laboratory.

—— Otto Formation ——			– Coleman River Formation –			Ridgepole Mountain Formation		
Al_{Gbs}	Al_{Kln}	Excess Al when $V_p/V_r = 1$	Al_{Gbs}	Al_{Kln}	Excess Al when $V_p/V_r = 1$	Al_{Gbs}	Al_{Kln}	Excess Al when $V_p/V_r = 1$
0.00	3.32	0.68	0.00	3.04	0.96	0.00	3.54	0.18
0.10	3.26	0.64	0.10	2.98	0.92	0.10	3.47	0.15
0.20	3.19	0.61	0.20	2.91	0.89	0.20	3.41	0.11
0.30	3.13	0.57	0.30	2.85	0.85	0.30	3.34	0.08
0.40	3.06	0.54	0.40	2.78	0.82	0.40	3.28	0.04
0.50	3.00	0.50	0.50	2.72	0.78	0.50	3.21	0.01
0.60	2.93	0.47	0.60	2.65	0.75	0.60	3.15	−0.03
0.70	2.87	0.43	0.70	2.59	0.71			
0.80	2.80	0.40	0.80	2.52	0.68			
0.90	2.74	0.36	0.90	2.46	0.64			
1.00	2.67	0.33	1.00	2.39	0.61			
1.10	2.61	0.29	1.10	2.33	0.57			
1.20	2.54	0.26	1.20	2.26	0.54			
1.30	2.48	0.22	1.30	2.20	0.50			
1.40	2.41	0.19	1.40	2.13	0.47			
1.50	2.35	0.15	1.50	2.07	0.43			
1.60	2.28	0.12	1.60	2.00	0.40			
1.70	2.22	0.08	1.70	1.94	0.36			
1.80	2.15	0.05	1.80	1.87	0.33			
1.90	2.09	0.01	1.90	1.81	0.29			
2.00	2.02	−0.02	2.00	1.74	0.26			
			2.10	1.68	0.22			
			2.20	1.61	0.19			
			2.30	1.55	0.15			
			2.40	1.48	0.12			
			2.50	1.42	0.08			
			2.60	1.35	0.05			
			2.70	1.29	0.01			
			2.80	1.22	−0.02			

embayed or euhedral, and highly fractured. Large crystals were inclusion rich (poikiloblastic), containing (in order of decreasing abundance) quartz, magnetite, biotite, muscovite, chlorite, and epidote. Many internal fractures originated near inclusions (Embrechts and Stoops, 1982) and radial fractures (Wendt *et al.*, 1993) occurred near some quartz inclusions. Other fractures occurred across embayments in rocks with strong preferred orientation and compositional banding. The fractures were perpendicular to foliation and are parallel to each other.

Ferruginous surface layers formed on most weathered almandine garnet grains. Continuous surface layers were more prevalent on euhedral, inclusion-poor grains and on grains that were extremely weathered. Discontinuous surface layers were more prevalent on embayed, inclusion-rich grains and on grains which border iron-rich phyllosilicates (chlorite or biotite). In these instances, weathering products were "co-mingled" with those from the surrounding chlorite or biotite minerals. Orange, red, and yellow-brown ferruginous deposits formed surface layers and boxworks along internal

Table 8. Calculations illustrating the influence of pyrolusite on Al distribution in PSLs ($V_p/V_r = 1$) for almandine garnet samples collected at Coweeta Hydrologic Laboratory.

Rock Unit	% Al in kaolinite for PSL of goethite + gibbsite + kaolinite	% Al in kaolinite for PSL of goethite + gibbsite + kaolinite + pyrolusite	% Difference
Otto Formation	52	28	46
Coleman River Formation	32	21	34
Ridgepole Mountain Formation	86	63	27

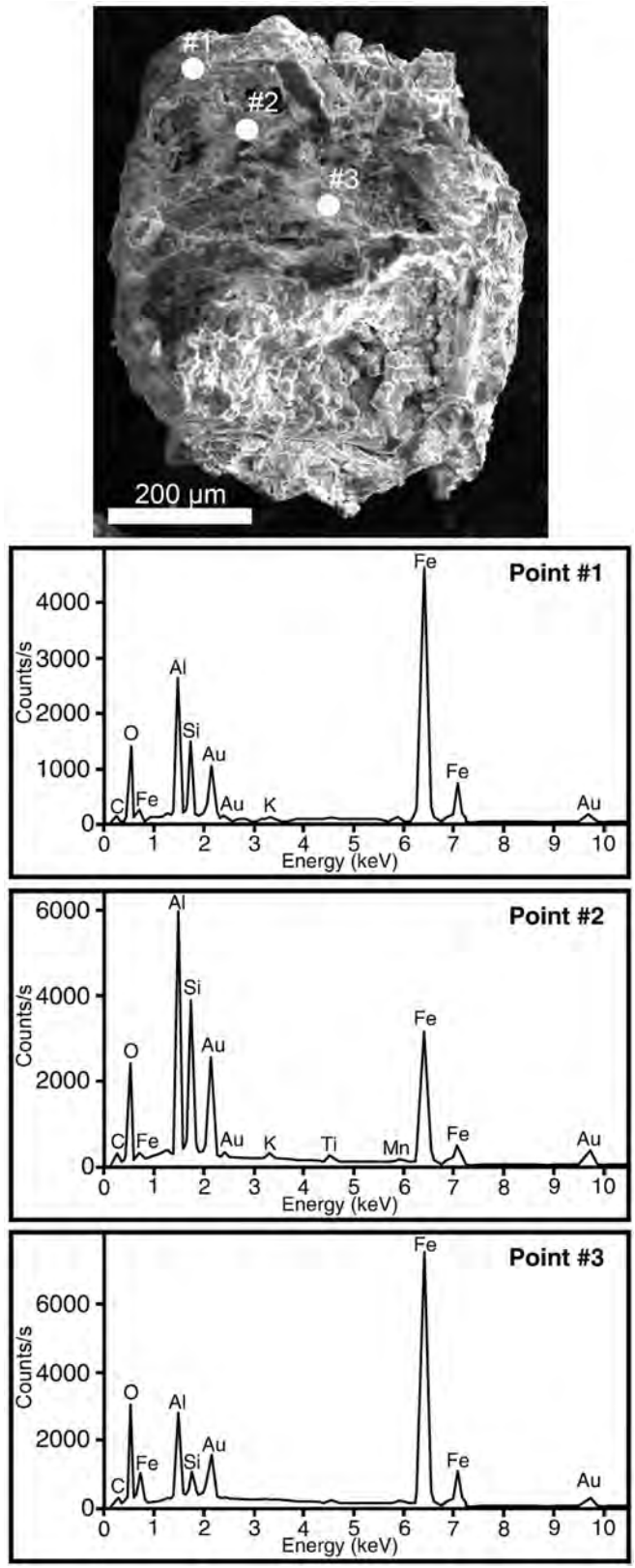

Figure 7. SEM-SEI image and EDS spectra of an Otto Formation garnet with surface layer hand picked from the regolith. Note the presence of Si in all spectra. Sample W34-6.

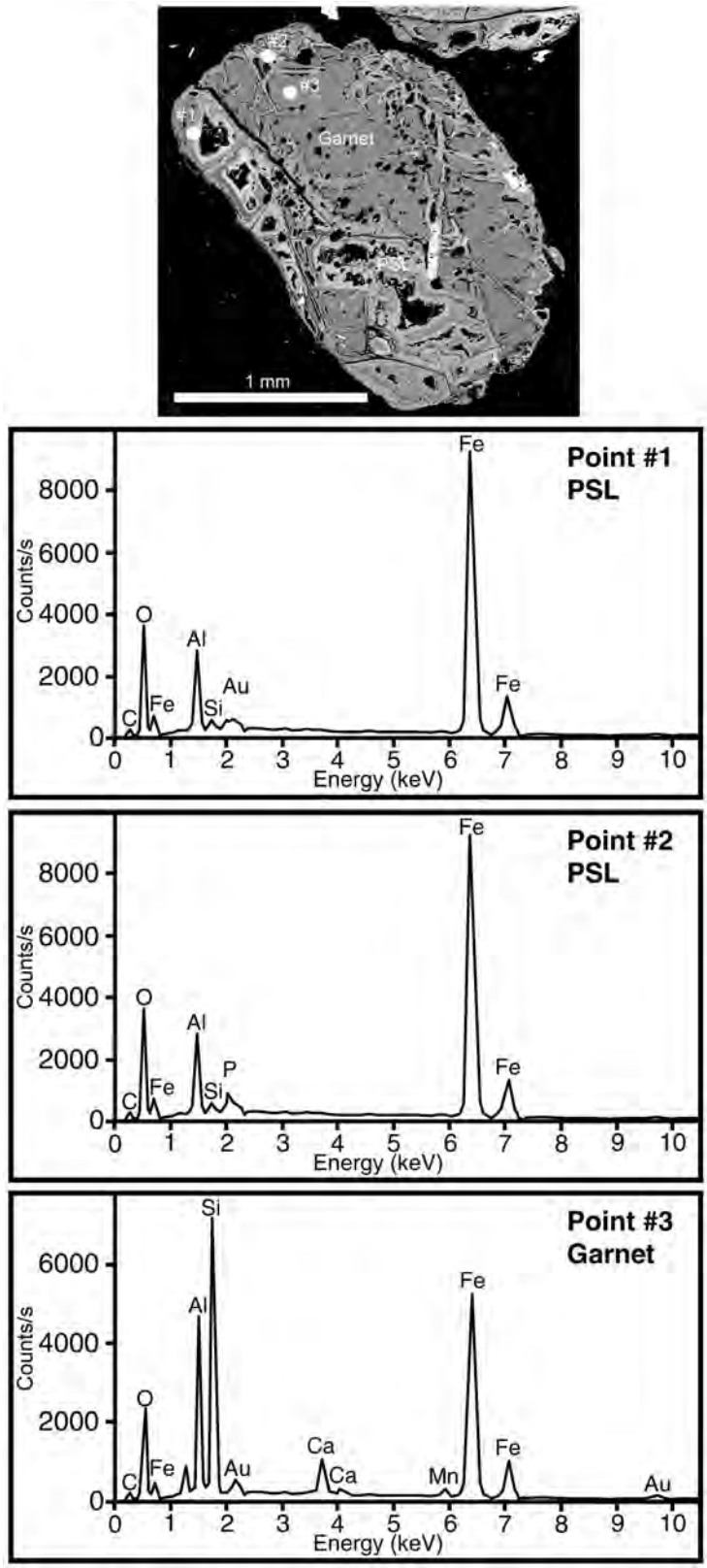

Figure 8. SEM-BEI image and EDS spectra of an Otto Formation garnet with surface layer. Points #1 and #2 are from the PSL and Point #3 is the unweathered garnet. Note the presence of Si in both PSL spectra. Sample W2-5.

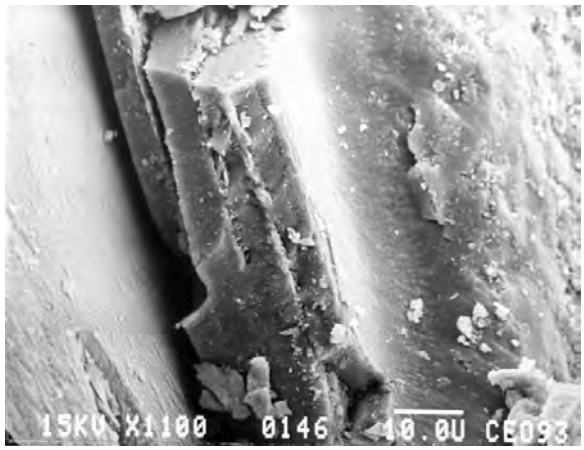

Figure 9. SEM-SEI image of 'onion skin-like' appearance of PSL on almandine garnet. Scale bar is 10 μm.

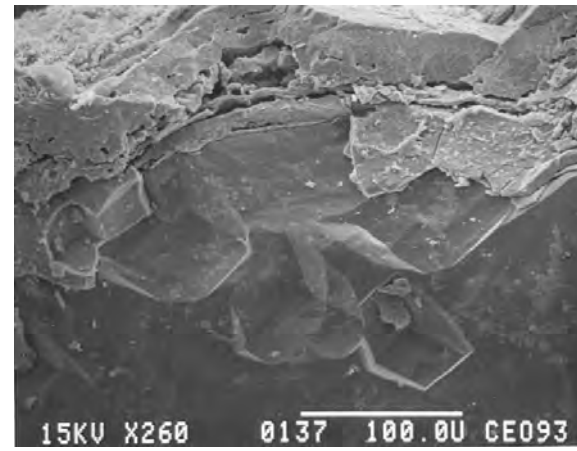

Figure 11. SEM-SEI image of dodecahedral etch pits on almandine garnet preserved in negative relief directly beneath a PSL. Scale bar is 100 μm.

fractures. In some thin sections, ferruginous deposits originating from a garnet occurred in rock fractures and stain surrounding unweathered minerals, suggesting that some garnet weathering products were being transported away from garnet grain boundaries.

Weathered almandine garnets from Coweeta exhibited both PSLs and USLs depending on sample locality and depth. Protective surface layers were the most common, exhibited minimal porosity, and were thickest in the saprolite and decreased in thickness higher in the soil profile. Protective surface layers were continuous over the entire grain surface and had no microporosity perpendicular to grain surfaces, no microporosity parallel to grain surfaces in outcrop samples, and minor (0.8–>5.0 mm in width) microporosity parallel to grain surfaces in profile samples. A PSL may become discontinuous and/or separated from the garnet's surface, probably due to dissolution and abrasion and have an 'onion skin-like' appearance in which successive layers are deposited in contact with previous layers (Figure 9).

Despite being protective as determined from V_p/V_r ratios, some occurrences of surface layers were found covering euhedral (dodecahedral) etch pits on subjacent garnets. Some etch pits were directly observable (Figures 10 and 11), others were preserved as casts on the undersides of the product layers (Figure 12). Unprotective surface layers only occurred in the warmer, dryer Watershed 2 (Figure 1), were more porous, and may have contained relatively high concentrations of hematite (Figure 5). An USL was continuous over the entire grain surface and had microporosity perpendicular to grain surfaces (pores of 8.0–10.0 mm in diameter) and little or no microporosity parallel to the grain surface. Unprotective surface layers were thickest in the upper

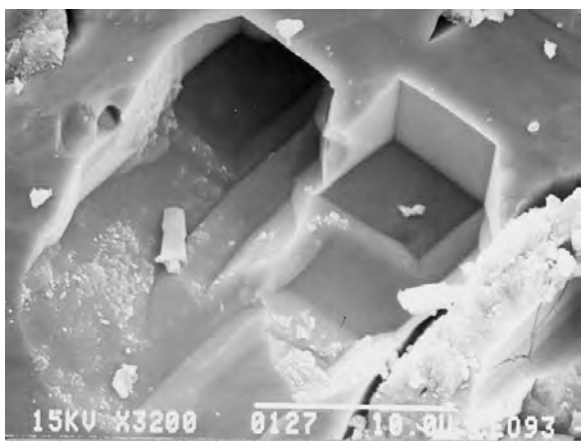

Figure 10. SEM-SEI image of dodecahedral etch pits on almandine garnet. Scale bar is 10 μm.

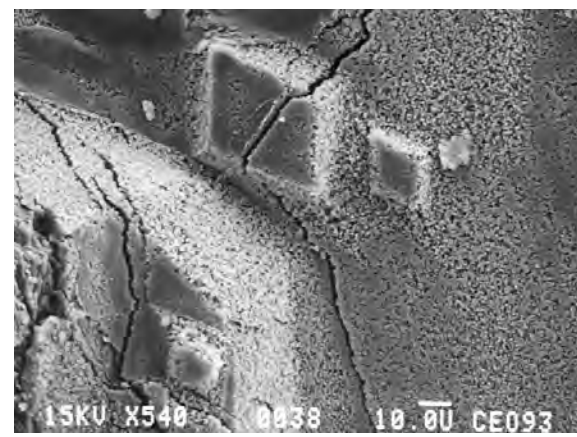

Figure 12. SEM-SEI image of casts of euhedral etch pits preserved in positive relief on the base of PSL separated from an almandine garnet–PSL interface by sample preparation. Scale bar is 10 μm.

horizons and decreased in thickness lower in the soil profile.

DISCUSSION

Application of Pilling-Bedworth rule to natural almandine garnet compositions

The results above indicate that very few natural almandine garnets have compositions sufficiently close to end-member almandine to allow the formation of PSL consisting of only goethite and gibbsite as suggested by Velbel (1984a, 1993). Based on the findings of the present study, in nearly all naturally occurring almandine garnets, some kaolinite likely must be present in a surface layer to make it protective. The addition of pyrolusite to the surface layer is capable of dramatically lowering the fraction of kaolinite required to make a PSL (Table 8). However, the addition of pyrolusite does not appear to be capable of completely eliminating the need for kaolinite within a PSL.

Micromorphology of CHL garnets and their surface layers

Ferruginous weathering products on naturally weathered saprolite almandine garnets exhibiting rounded and featureless surfaces and having calculated $V_p/V_r \geqslant 1$ have been interpreted as being a PSL. In contrast, etch pits on naturally weathered soil almandines have been interpreted to indicate interface-limited reaction processes (Velbel, 1984a, 1993; Velbel *et al.*, 2007). Garnet etch pits (*e.g.* Figure 10) formed in the absence of PSLs occur in a variety of soil types, apparently where pedogenic complexing agents mobilize Al and/or Fe, and thereby prevent the formation of PSLs (Velbel, 1984a; Ghabru *et al.*, 1989; Velbel *et al.*, 2007). The occurrence of etch pits (Figure 11) and etch-pit casts (Figure 12) in association with surface layers reported here for the first time requires reexamination of the relationship between specific secondary minerals and the rate-determining processes associated with those minerals. Two possible explanations for the presence of PSL-associated etch pits and etch-pit casts are offered: (1) almandine garnet weathers first to a USL followed by mineralogical changes yielding a PSL (*e.g.* hematite hydrating to goethite; Schwertmann, 1971; Campbell and Schwertmann, 1984); or (2) almandine weathers to a surface layer in a mixed-kinetic regime. Each of these possible scenarios is explored below.

Conversion of a USL to a PSL. The presence of a PSL covering etch pits (Figures 11, 12) implies that the surface layer was not diffusion limiting at the time of etch-pit formation, but rather almandine garnet weathering was interface limited. These observations, combined with the Pilling-Bedworth calculations permit the hypothesis that secondary hematite formed at the onset of garnet weathering, forming a USL that allowed rapid solute transport. In the cooler, wetter localities found at the higher elevations of CHL, the early-formed hematite subsequently hydrated to form (tertiary) goethite in a PSL. In virtually all CHL sample sites, almandine garnet is weathering to predominantly goethite (*e.g.* Figure 5). Goethite has also been identified as a predominant weathering product of almandine garnet at other sites (Embrechts and Stoops, 1982; Parisot *et al.*, 1983; Velbel, 1984a; Graham *et al.* 1989a; Robertson and Butt, 1997). The molar volume per Fe is greater for goethite than for hematite (Table 1), and the hydration of Fe products caused a volume increase. This volume increase allowed the hydrated products to occupy formerly vacant space, reducing porosity and thereby filling etch pits and forming casts (Figure 12). The increase in product volume as the goethitic surface layer became protective caused by the hydration process would fill or cover pre-existing etch pits and would prevent additional etch pits from forming.

Based on the discussion above, drawing mechanistic inferences from product mineralogy alone (without information on textural relationships, *e.g.* centripetal replacement textures) is hazardous. For instance, hematite is believed to form from almandine garnet in at least some Southern Blue Ridge weathering profiles (Graham *et al.*, 1989a, 1989b, 1990a, 1990b), and has been identified in the Coweeta PSLs (Figure 5). If almandine garnet weathered directly to secondary hematite, Velbel's (1993) calculations and those as part of this study (Table 6) would suggest that the hematite-bearing product is far less likely to yield a PSL, especially in combination with gibbsite as the sole Al-bearing product. In the present study, etch-pit casts occur only with a PSL containing goethite as the dominant ferruginous product. While no direct evidence of a hematite precursor for these specific goethites was observed, such transformations between hydrous and anhydrous iron oxides are common in weathering environments (*e.g.* Schwertmann, 1971; Campbell and Schwertmann, 1984), and hematite has formed during the weathering history of CHL saprolites (*e.g.* Figure 5). Textural evidence such as etch-pit casts preserve remnant reactant garnet surface textures and suggest, in such instances, both the pathway of goethite formation and the change over time in the rate-determining role of the product. Thus, in the absence of information from replacement textures, the present mineralogy alone of a product assemblage with $V_p/V_r < 1$ is not a sufficient criterion for dismissing the protective surface layer hypothesis, or for confirming that the product itself was not rate determining.

Temporal changes in surface layer mineralogy and kinetic regime are not limited to the Fe-bearing phases hematite and goethite. The Pilling-Bedworth calculations indicate that a PSL is unlikely to form in the absence of kaolinite when gibbsite is the sole aluminous phase. Gibbsite has also been identified as a weathering

product of garnet by previous workers (Velbel, 1984a; Graham *et al.*, 1989a, 1989b, 1990b). However, to transition from interface-controlled to diffusion-controlled kinetics would require the silication of a 0:1 clay (*i.e.* gibbsite). Typically, with progressive weathering, kaolinite will desilicate to gibbsite. Following this premise, kaolinite would probably form at the beginning of garnet weathering, although some desilication could occur afterwards as long as adequate kaolinite remained to maintain the PSL. Excess Si associated with garnet weathering to a PSL (discussed in the next section) would be available for silication of gibbsite. However, conservation of Si in the almandine garnet-surface layer system would probably only occur with a PSL already present, *i.e.* when Si loss was inhibited by diffusion through the PSL. Based on this reasoning, a conversion from a USL to a PSL, and associated change from interface-controlled to transport-controlled kinetics, would be the more likely result of hematite hydrating to goethite with some kaolinite already present in the surface layer.

Mixed-kinetic control. Weathering regimes which form both etch pits and protective surface layers might be intermediate between transport- and interface-limited kinetic regimes (the mixed-kinetics regime of Berner, 1978, 1981). Where a PSL is slightly discontinuous (Figure 9), interface-limited weathering reactions operate and etch pits form (Figure 11).

Unprotective surface layers increase in thickness higher in the weathering profile. This observation indicates that garnets with USLs weather by centripetal replacement. Almandine garnet grains with USLs appear to have no dissolution features (*e.g.* etch pits) on their surfaces, although the etch pits may be covered by the oxides which form a USL. As reported by Velbel (1984a) and Embrechts and Stoops (1982), regardless of type of surface layer that may form by weathering in the saprolite prior to pedogenesis, almandine garnet weathering in soil horizons proceeds with the formation of a USL which is commonly removed completely with continued pedogenesis in soil horizons (Velbel, 1984a; Ghabru *et al.*, 1989; Velbel *et al.*, 2007).

The two aforementioned explanations of the occurrence of etch pits under a PSL offer plausible explanations for the previously unreported and unexpected weathering texture of etch pits covered by a subsequent layer of secondary (or tertiary) products (Figure 11). The almandine garnet grain was removed directly from rock outcrop. The almandine garnet surface layer is discontinuous and may be so because of mechanical separation from the surrounding matrix or because the surface layer is still forming. The surface layer did form well below the rooting zone and is not discontinuous due to biochemical dissolution. Also, because the almandine garnet was removed from outcrop, the etch pits were not covered by products as a result of direct introduction into the rooting zone followed by reburial. The most probable explanations are that the etch pits formed during preliminary dissolution of the almandine garnet surface and were later filled by the products of the replacement process, or formed while the almandine garnet surface was covered by a porous, hematitic surface layer and were later filled by goethite as the hematite hydrated. The morphological consequences of the last part of this proposed sequence of phenomena may be expressed and preserved at the inner margin of a PSL where it is in direct contact with, and forms a cast of, the etched almandine surface (Figure 12).

Elemental imports and exports for the CHL almandine garnet-PSL system

A surface layer composed of goethite, gibbsite, and kaolinite would probably be protective. Furthermore, an excess of Al is feasible and thus available for export. Velbel (1993) determined that up to 15% of the Al and Fe produced during almandine garnet weathering could be exported from the garnet-PSL microenvironment. For the almandine garnet compositions from Deer *et al.* (1997) used in the present study, up to 35% of the Al produced during almandine garnet weathering may be exported. Such a large value is only possible if all of the Fe is conserved and substantial quantities of kaolinite are present in the PSL. However, petrographic observations reveal that occasionally ferruginous material will extend from a garnet grain into fractures and around adjacent minerals. Migration of Fe from a garnet grain indicates that the assumption of conservation of all almandine garnet-derived Fe in the surface layer may not be valid for some grains. If the quantity of Fe available for surface layer is reduced, then the proportion of kaolinite in a PSL would have to increase relative to gibbsite. This relative increase in PSL kaolinite would also reduce the quantity of Al available for export from the almandine garnet-surface layer microenvironment.

Velbel *et al.* (2009) investigated the formation of USL on hornblende sampled from regolith of the southern Appalachian Blue Ridge of northeastern Georgia, USA. Using similar molar volume calculations as this study, these authors determined that Al must be imported into early-stage weathering products of the hornblende. During the early stages for weathering, considerable mobilization of Al occurred while Si was immobile, despite Al typically being considered minimally mobile during weathering. Velbel *et al.* (2009) suggested that Al is mobilized from shallow depths to greater depths in the weathering profile where incipient weathering is occurring. Further, Velbel *et al.* (2009) proposed that the source of the imported Al is from almandine garnet weathering known to occur in their rock unit of study, although no unweathered almandine garnet was observed in their specific sample. Velbel *et al.* (2009) showed how the proposed Al mobility is consistent with the results of Gardner (1992), White *et*

al. (1998), and Schroeder *et al.* (2000) based on bulk-sample-scale and profile-scale mineralogical data, solid-phase bulk-chemical analyses of saprolitic weathering profiles, and solute-phase chemical data from soil solutions, groundwater, and modern surface water associated with deeply weathered landscapes.

The possibility of import of element(s) into the almandine garnet-PSL system also warrants investigation. For Coweeta almandine garnets, the balanced weathering reactions for a PSL of goethite and kaolinite, thereby reflecting the maximum production of excess Al (Tables 3 and 7), are as follows:

Otto Formation.

$$Ca_{0.82}Mg_{0.72}Mn_{1.0}Fe_{3.52}Al_4Si_6O_{24} + 7.88\ H_2O + 5.12\ H^+ + 1.41\ O_2 \rightarrow 3.52\ FeOOH + 1.66\ Al_2Si_2O_5(OH)_4 + 2.68\ H_4SiO_4 + 1.0\ MnO_2 + 0.82\ Ca^{2+} + 0.72\ Mg^{2+} + 0.68\ Al^{3+} \quad (7)$$

Coleman River Formation.

$$Ca_{0.60}Mg_{0.88}Mn_{0.44}Fe_{4.26}Al_4Si_6O_{24} + 8.17\ H_2O + 5.84\ H^+ + 1.38\ O_2 \rightarrow 4.26\ FeOOH + 1.52\ Al_2Si_2O_5(OH)_4 + 2.96\ H_4SiO_4 + 0.44\ MnO_2 + 0.60\ Ca^{2+} + 0.88\ Mg^{2+} + 0.96\ Al^{3+} \quad (8)$$

Ridgepole Mountain Formation.

$$Ca_{1.74}Mg_{0.74}Mn_{0.90}Fe_{2.82}Al_{3.72}Si_6O_{24} + 7.12\ H_2O + 5.50\ H^+ + 1.05\ O_2 \rightarrow 2.82\ FeOOH + 1.77\ Al_2Si_2O_5(OH)_4 + 2.46\ H_4SiO_4 + 0.90\ MnO_2 + 1.74\ Ca^{2+} + 0.74\ Mg^{2+} + 0.18\ Al^{3+} \quad (9)$$

These balanced reactions for the formation of a goethite and kaolinite PSL demonstrate that no other major elements need be imported into the PSL-garnet system at Coweeta. However, significantly more Si than Al is released, providing the elements needed to form kaolinite. For the Al to be exported rather than consumed as either kaolinite and/or gibbsite precipitate, the pore solutions must be undersaturated with respect to these phases.

Evaluation of the hypothesis and unresolved issues

The hypothesis for this study was that the role of the kinetics of almandine garnet's weathering products varies with the composition of the specific almandine experiencing weathering. The results of the Pilling-Bedworth calculations and microtextural observations of naturally weathered garnet surfaces from all levels in the CHL weathering profile are consistent with this hypothesis.

The findings of this study yield numerous additional unresolved issues regarding the formation of surface layers on garnets during chemical weathering. The temporal changes in surface-layer mineralogy that may result in etch pits occurring beneath PSLs requires additional investigation. This includes the hypothesized conversion of early-formed hematite to goethite, and the potential role of Si in conversions between gibbsite and kaolinite. Such mineralogical changes should be related directly to the surface microtextures of the dissolving garnet and Pilling-Bedworth calculations. The generation and mobility of Al during incipient garnet weathering, and the potential uptake of that Al by the weathering products of other primary minerals, also warrant further investigation. All of the methods and unresolved questions outlined in this study for almandine garnets may also be applied to garnets representing a wider range of compositions (*e.g.* other garnet solid-solution series) and environmental settings.

SUMMARY AND CONCLUSIONS

The mineralogy of surface layers exerts a major influence on the chemical weathering kinetics of almandine garnet; different product minerals occupy different proportions of the replacement volume and thereby influence the solute-transport properties of the product. During chemical weathering, almandine garnet grains can develop either protective or unprotective surface layers depending on the almandine garnet's Al and Fe stoichiometric coefficients, molar mass, specific gravity, mineralogy of secondary products, and environmental conditions. The results of this study are consistent with the hypothesis that the role of the kinetics of almandine garnet's weathering products varies with the composition of the specific almandine garnet experiencing weathering. Most natural almandine garnets lack adequate Fe and Al to form PSLs composed only of goethite and gibbsite. Having kaolinite in a surface layer dramatically increases the probability of a surface layer being protective. At CHL for almandine garnets from the three units studied, in order to form a PSL, kaolinite must be a weathering product. The lack of kaolinite being reported in the literature may be due to inadequacy of XRD. Energy-dispersive X-ray spectra and XRD analyses as part of this study support the presence of kaolinite in Coweeta almandine garnet PSLs. The greatest likelihood that a surface layer will be protective is when it contains goethite, kaolinite, and pyrolusite. With adequate Mn in the parent garnet and if pyrolusite precipitates in the PSL, the V_p/V_r value will increase. However, pyrolusite in a surface layer may not increase greatly the likelihood of the layer being protective; the presence of pyrolusite does significantly decrease the quantity of kaolinite needed to make a surface layer protective.

Based on an almandine garnet anion basis of O_{24}, to form a PSL composed of hematite and kaolinite, an almandine garnet must have a minimum Al stoichiometric coefficient of ~3.78 a.p.f.u. and a minimum Fe stoichiometric coefficient of ~2.8 a.p.f.u. To form a PSL of goethite and kaolinite, an almandine garnet must have a minimum Al stoichiometric coefficient of

~3.75 a.p.f.u. and a minimum Fe stoichiometric coefficient of ~2.7 a.p.f.u. A relatively large parent garnet Fe stoichiometric coefficient is more important in PSL formation and determination of excess Al than is the parent almandine garnet Al stoichiometric coefficient.

Almandine garnet and ferruginous product(s) in thin section form three distinct textures: (1) grains in which ferruginous product is in contact with the garnet remnant; (2) grains in which ferruginous product is not in contact with the almandine garnet remnant (formation of a peripheral void around remnant); and (3) grains in which ferruginous product has formed a porous pseudomorph after garnet. Almandine garnet grains in environments dominated by biochemical processes and advective flow undergo interface-limited reactions. Almandine garnet grains in environments not dominated by these processes experience supersaturation with respect to iron and aluminum products near the grain surface. When the requirements for nucleation are met, the products reprecipitate to form a PSL.

Etch pits occur on almandine garnet grains beneath some PSLs. This association of etch pits (which indicate interface-limited kinetics) and PSLs (which should inhibit transport of mobile species to and/or from the almandine's surface, result in reaction kinetics limited by transport through the product, and thereby prevent the formation of etch pits) is unexpected based on the original formulation of the hypothesis. The Pilling-Bedworth calculations of this study suggest a modification of the hypothesis. Several combinations of changes of secondary minerals into tertiary minerals could result in the newly reported association between etch pits (formed in the kinetic regime influenced by the secondary minerals) and PSLs (consisting of tertiary minerals modified from the secondary minerals after the etch pits formed). Early-formed (secondary) product minerals formed USLs and allowed interface-limited attack upon, and etching of, the underlying almandine garnet's surface. This was followed by modification of the secondary product minerals to tertiary product minerals with increased volume that rendered the surface layers protective of the underlying surface after the etch pits had formed.

Several secondary-tertiary product-mineral paragenetic sequences are consistent with this time-variant extension of the original hypothesis. Filled etch pits under PSLs may be the result of hematitic surface layers hydrating to goethitic surface layers or the result of dissolution-reprecipiation processes. The initial formation of hematite in an USL, followed by hydration of hematite to form goethite, reduces porosity. Consequently, the product's transport properties are reduced such that the previously USL of product becomes a PSL only after the etch pits had formed. Similarly, the silication of gibbsite to kaolinite after initial formation of an USL in which Al was hosted by gibbsite would increase product volume, reduce porosity, and change the rate-determining process only after the etch pits had formed. Alternatively, almandine garnet dissolution processes which form PSLs and etch pits may be intermediate between transport- and interface-limited kinetic regimes (Berner, 1978; 1981). Discontinuous surface layers permit the formation of etch pits.

With a PSL of goethite, gibbsite, and kaolinite, excess Al may reasonably be assumed to be available for export. A reduction in the quantity of kaolinite in a PSL resulting from the presence of pyrolusite increases the quantity of Al available for export from the garnet-PSL system. For CHL garnets with PSL and excess Al, no other element need be imported into the garnet-PSL system to produce the observed weathering-product mineral assemblages.

ACKNOWLEDGMENTS

The authors thank S. Anderson, R. Schaetzl, D. Schulze, E. Danielewicz, S. Flegler, D. Mokma, C. Basso, W. Swank, and the staff at the Coweeta Hydrologic Laboratory. Appreciation is also expressed to S. Sylvester at Franklin & Marshall College for assistance with XRD. The present study was funded in part by a grant from The Clay Minerals Society to D. Bryan. Thanks, too, to Editor-in-Chief J.W. Stucki and Associate Editor W.D. Huff for editorial handling, as well as two anonymous reviewers whose constructive reviews greatly strengthened this manuscript.

REFERENCES

Berner, R. (1978) Rate control of mineral dissolution under earth surface conditions. *American Journal of Science*, **278**, 1235–1252.

Berner, R. (1981) Kinetics of weathering and diagenesis. Pp. 111–134 in: *Kinetics of geochemical processes* (A. Lasaga and R. Kirkpatrick, editors). Reviews in Mineralogy, **8**, Mineralogical Society of America, Washington, D.C.

Berner, R.A. and Holdren, G.R. (1977) Mechanism of feldspar weathering: Some observational evidence. *Geology*, **5**, 369–372.

Berner, R.A. and Holdren, G.R. (1979) Mechanism of feldspar weathering II: Observations of feldspar from soils. *Geochimica et Cosmochimica Acta*, **43**, 1173–7786.

Berner, R. and Schott, J. (1982) Mechanism of pyroxene and amphibole weathering II. Observations of soil grains. *American Journal of Science*, **282**, 1214–1231.

Berner, R., Sjoberg, E., Velbel, M., and Krom, M. (1980) Dissolution of pyroxenes and amphiboles during weathering. *Science*, **207**, 1205–1206.

Berry, J.L. (1976) Study of chemical weathering in the Coweeta Hydrologic Laboratory, Macon County, North Carolina, 62 pp. Unpublished report.

Blum, A.E. and Lasaga, A.C. (1987) Monte Carlo simulations of surface reaction rate laws. Pp. 255–292 in: *Aquatic Surface Chemistry* (W. Stumm, editor). John Wiley & Sons, New York.

Blum, A.E. and Stillings, L.L. (1995) Feldspar dissolution kinetics. Pp. 291–342 in: *Chemical Weathering Rates of Silicate Minerals* (A.F. White and S.L. Brantley, editors). Reviews in Mineralogy **31**, Mineralogical Society of America, Washington, D.C.

Brantley, S.L. (2005) Reaction kinetics of primary rock-forming minerals under ambient conditions. Pp. 73–117

in: *Surface and Ground Water, Weathering, and Soils* (J.I. Drever, editor), Treatise on Geochemistry **5**, Elsevier-Pergamon, Oxford, UK.

Brantley, S.L. (2008) Kinetics of mineral dissolution. Pp. 151–210 in: *Kinetics of Water–Rock Interaction* (S.L. Brantley, J.D. Kubicki, and A.F. White, editors). Springer, New York.

Brantley, S.L. and Chen, Y. (1995) Chemical weathering rates of pyroxenes and amphiboles. Pp. 119–172 in: *Chemical Weathering Rates of Silicate Minerals* (A.F. White and S.L. Brantley, editors). Reviews in Mineralogy, **31**, Mineralogical Society of America, Washington, D.C.

Brantley, S.L., Crane, S.R., Crerar, D.A., Hellmann, R., and Stallard, R. (1986) Dissolution at dislocation etch pits in quartz. *Geochimica et Cosmochimica Acta*, **50**, 2349–2361.

Browning, S. and Thomas, D. (1985) Soil map of Coweeta Hydrologic Laboratory. U.S. Department of Agriculture, Forest Service, Southeastern Forest Experiment Station.

Bryan, D.S. (1994) Factors controlling the occurrence and distribution of hematite and goethite in soils and saprolites derived from schists and gneisses in western North Carolina. M.S. thesis, Michigan State University, East Lansing, Michigan, USA, 125 pp.

Campbell, A. and Schwertmann, U. (1984) Iron oxide mineralogy of placic horizons. *Journal of Soil Science*, **35**, 569–582.

Ciampone, M.A. (1995) Non-systematic weathering profile on metamorphic rock in the southern Blue Ridge Mountains, North Carolina: Petrography, bulk chemistry, and mineral chemistry of biotite. M.S. thesis, University of Cincinnati, Cincinnati, Ohio, USA, 86 pp.

Deer, W.A., Howie, R.A., and Zussman, J. (1997) *Rock-Forming Minerals – Orthosilicates*, **1A**, second edition. The Geological Society, London.

Drever, J.I. (1973) The preparation of oriented clay mineral specimens for X-ray diffraction analysis by a filter-membrane peel technique. *American Mineralogist*, **58**, 553–554.

Embrechts, J. and Stoops, G. (1982) Microscopical aspects of garnet weathering in a humid tropical environment. *Journal of Soil Science*, **33**, 535–545.

Fromhold, A.T., Jr. (1976) *Theory of Metal Oxidation. I. Fundamentals*. Defects in Crystalline Solids Series, **9**. North-Holland, Amsterdam.

Gardner, L.R. (1992) Long-term isovolumetric leaching of aluminum from rocks during weathering: Implications for the genesis of saprolite. *Catena*, **19**, 521–537.

Ghabru, S., Mermut, A., and St. Arnaud, R. (1989) Characterization of garnets in a typic Cryoboralf (Gray luvisol) from Saskatchewan, Canada. *Soil Science of America Journal*, **53**, 575–582.

Graham, R., Weed, S., Bowen, L., and Buol, S. (1989a) Weathering of iron-bearing minerals in soils and saprolite on the North Carolina Blue Ridge Front: I. Sand-size primary minerals. *Clays and Clay Minerals*, **37**, 19–28.

Graham, R., Weed, S., Bowen, L., and Buol, S. (1989b) Weathering of iron-bearing minerals in soils and saprolite of the North Carolina Blue Ridge Front: II. Clay Mineralogy. *Clays and Clay Minerals*, **37**, 29–40.

Graham, R., Daniels, R., and Buol, S. (1990a) Soil geomorphic relations on the Blue Ridge Front: I. Regolith types and slope processes. *Soil Science Society of America Journal*, **54**, 1362–1367.

Graham, R., Daniels, R., and Buol, S. (1990b) Soil geomorphic relations on the Blue Ridge Front: II. Soil Characteristics and Pedogenesis. *Soils Science Society of America Journal*, **54**, 1367–1377.

Hansley, P.L. (1987) Petrologic and experimental evidence for the etching of garnets by organic acids in the Upper Jurassic Morrison Formation, northwestern New Mexico. *Journal of Sedimentary Petrology*, **57**, 666–681.

Hatcher, R.D. (1980) Geologic map of Coweeta Hydrologic Laboratory, Prentiss Quadrangle, North Carolina: State of North Carolina, Department of Natural Resources and Community Development, in Cooperation with the Tennessee Valley Authority, scale 1:14,400, 1 sheet.

Hatcher, R.D. (1988) Bedrock geology and regional geologic setting of Coweeta Hydrologic Laboratory in the Eastern Blue Ridge. Pp. 81–92 in: *Forest Hydrology and Ecology at Coweeta* (W.T. Swank and D.A. Crossley, Jr., editors). Springer-Verlag, New York.

Hauffe, K. (1965) *Oxidation of Metals*. Plenum, New York.

Kretz, R. (1983) Symbols for rock-forming minerals. *American Mineralogist*, **68**, 277–279.

Klein, C. and Hurlbut, C.S. (1999) *Manual of Mineralogy*. John Wiley & Sons, Inc., New York.

Kubaschewski, O. and Hopkins, B.E. (1962) *Oxidation of Metals and Alloys* (2nd edition). Butterworths, London.

Lasaga, A. and Blum, A. (1986) Surface chemistry, etch pits and mineral water reactions. *Geochimica et Cosmochimica Acta*, **50**, 2363–2379.

Lüttge, A. and Arvidson, R.S. (2008) The mineral–water interface. Pp. 73–107 in: *Kinetics of Water–Rock Interaction* (S.L. Brantley, J.D. Kubicki, and A.F. White, editors). Springer, New York.

Miller, C.F., Hatcher, R.D., Jr., Ayers, J.C., Coath, C.D., and Harrison, T.M. (2000) Age and zircon inheritance of eastern Blue Ridge plutons, southwestern North Carolina and northeastern Georgia, with implications for magma history and evolution of the southern Appalachian orogen. *American Journal of Science*, **300**, 142–172.

Moore, D.M. and Reynolds, Jr., R.C. (1997) X-*ray Diffraction and the Identification and Analysis of Clay Minerals*. Oxford University Press, New York.

Parisot, J.C., Delvigne, J., and Groke, M.T.C. (1983) Petrographical aspects of the supergene weathering of garnet in the Serra dos Carajas (Para, Brazil). P. 47 in: *International Colloquium CNRS on the Petrology of Weathering and Soils, Abstracts* (D. Nahon and Y. Noack, editors). Centre National de la Recherche Scientifique, Paris.

Price, J.R. (2003) Allanite weathering and rare earth elements in mass balance calculations of clay genesis rates at the Coweeta Hydrologic Laboratory, western North Carolina, USA: The response times of changes in clay mineral assemblages to fluctuations in climate. Ph.D. thesis, Michigan State University, East Lansing , Michigan, USA, 237 pp.

Price, J.R., Velbel, M.A., and Patino, L.C. (2005) Rates and timescales of clay-mineral formation in the southern Appalachian Mountains from geochemical mass balance, *Geological Society of America Bulletin*, 117, 783–794.

Robertson, I.D.M. and Butt, C.R.M. (1997) *Atlas of Weathered Rocks*. CRC LEME Open File Report **390**, 1st Revision. Cooperative Research Centre for Landscape Evolution and Mineral Exploration, Wembley, Western Australia.

Salvino, J.F. and Velbel, M.A. (1989) Faceted garnets from sandstones of the Munising Formation (Cambrian), northern Michigan: petrographic evidence for origin by intrastratal dissolution. *Sedimentology*, **36**, 371–379.

Schott, J. and Petit, J.-C. (1987) New evidence for the mechanisms of dissolution of silicate minerals. Pp. 255–292 in: *Aquatic Surface Chemistry* (W. Stumm, editor). John Wiley & Sons, New York.

Schroeder, P.A., Melear, N.D., West. L.T., and Hamilton, D.A. (2000) Meta-gabbro weathering in the Georgia Piedmont, USA: implications for global silicate weathering rates. *Chemical Geology*, **163**, 235–245.

Schwertmann, U. (1971) Transformations of hematite to goethite in soils. *Nature*, **232**, 624–625.

Smyth, J.R. and Bish, D.L. (1988) *Crystal Structures and Cation Sites of the Rock-Forming Minerals*. Allen & Unwin, Boston, Massachusetts, USA.

Swank, W. and Crossley, I. (1988) Introduction and site description. Pp. 3–15 in: *Forest Hydrology and Ecology at Coweeta* (W.T. Swank and D.A. Crossley, Jr., editors). Springer-Verlag, New York.

Velbel, M. (1984a) Natural weathering mechanisms of almandine garnet. *Geology*, **12**, 631–634.

Velbel, M. (1984b) Mineral transformations during rock weathering, and geochemical mass-balances in forested watersheds of the Southern Appalachians. Ph.D. thesis, Yale University, New Haven, Connecticut, USA, 175 pp.

Velbel, M. (1985) Geochemical mass balances and weathering rates in forested watersheds of the southern Blue Ridge. *American Journal of Science*, **285**, 904–930.

Velbel, M.A. (1988) Weathering and soil-forming processes, Pp. 93–102 in: *Forest Hydrology and Ecology at Coweeta* (W.T. Swank and D.A. Crossley, Jr., editors). Springer-Verlag, New York.

Velbel, M.A. (1989) Weathering of hornblende to ferruginous products by a dissolution-reprecipitation mechanism: petrography and stoichiometry. *Clays and Clay Minerals*, **37**, 515–524.

Velbel, M.A. (1990) Mechanisms of saprolitization, isovolumetric weathering, and pseudomorphous replacement during rock weathering – a review. *Chemical Geology*, **84**, 17–18.

Velbel, M.A. (1993) Formation of protective surface layers during silicate-mineral weathering under well-leached, oxidizing conditions. *American Mineralogist*, **78**, 408–417.

Velbel, M.A. (2004) Laboratory and homework exercises in the geochemical kinetics of mineral–water reaction: rate law, Arrhenius activation energy, and the rate-determining step in the dissolution of halite. *Journal of Geoscience Education*, **52**, 52–59.

Velbel, M.A. (2007) Surface textures and dissolution processes of heavy minerals in the sedimentary cycle: examples from pyroxenes and amphiboles. Pp. 113–150 in: *Heavy Minerals in Use* (M.A. Mange and D.T. Wright, editors). Developments in Sedimentology, **58**, Elsevier, New York.

Velbel, M.A. and Barker, W.W. (2008) Pyroxene weathering to smectite: Conventional and low-voltage cryo-field emission scanning electron microscopy, Koua Bocca ultramafic complex, Ivory Coast. *Clays and Clay Minerals*, **56**, 111–126.

Velbel, M.A., McGuire, J.T., and Madden, A.S. (2007) Scanning electron microscopy of garnet from southern Michigan soils: Etching rates and inheritance of pre-glacial and pre-pedogenic grain-surface textures. Pp. 413–432 in: *Heavy Minerals in Use* (M.A. Mange and D.T. Wright, editors). Developments in Sedimentology, **58**, Elsevier, New York.

Velbel, M.A., Donatelle, A.R., and Formolo, M.J. (2009) Reactant-product textures, volume relations, and implication for major-element mobility during natural weathering of hornblende, Tallulah Falls Formation, Georgia Blue Ridge, U.S.A. *American Journal of Science*, **309**, 661–688.

Wendt, A., D'Arco, P., Goffé, B., and Oberhänsli, R. (1993) Radial cracks around α-quartz inclusions in almandine: Constraints on the metamorphic history of the Oman Mountains. *Earth and Planetary Science Letters*, **114**, 449–461.

White, A.F., Blum, A.E., Schulz, M.S., Vivit, D.V., Stonestrom, D.A., Larsen, M., Murphy, S.F., and Eberl, D. (1998) Chemical weathering in a tropical watershed, Luquillo Mountains, Puerto Rico: I. Long-term versus short-term weathering fluxes. *Geochimica et Cosmochimica Acta*, **62**, 209–226.

Wilson, M.J. (1975) Chemical weathering of some primary rock-forming minerals. *Soil Science*, **119**, 349–355.

Yeakley, J.A., Swank, W.T., Swift, L.W., Hornberger, G.M., and Shugart, H.H. (1998) Soil moisture gradients and controls on a southern Appalachian hillslope from drought through recharge. *Hydrology and Earth System Sciences*, **2**, 41–49.

(*Received 27 August 2012; revised 18 February 2013; Ms. 706; AE: W.D. Huff*)

Clays and Clay Minerals, Vol. 61, No. 2, 83–97, 2013.

STRUCTURAL CHARACTERIZATION OF REDUCED-CHARGE MONTMORILLONITES. EVIDENCE BASED ON FTIR SPECTROSCOPY, THERMAL BEHAVIOR, AND LAYER-CHARGE SYSTEMATICS

Evangelos N. Skoubris[1], Georgios D. Chryssikos[2], George E. Christidis[1,*], and Vassilis Gionis[2]

[1] Technical University of Crete, Department of Mineral Resources Engineering, Chania, Greece 73100
[2] Theoretical and Physical Chemistry Institute, National Hellenic Research Foundation, 48 Vass. Constantinou Ave., Athens, Greece 11635

Abstract—In the present study, the gradual layer-charge reduction of two Li-saturated smectites, SAz-1 from Arizona, USA, and FEO-G from Troodos, Cyprus, with octahedral charge of 0.54 electrons per half unit cell (e/huc) and 0.39 e/huc, respectively, was monitored by X-ray diffraction of K-saturated, ethylene glycol-solvated samples, by thermogravimetry-differential thermogravimetry, and by mid- and near-Fourier transform infrared spectroscopy after heating at 80−300ºC. With increasing heating temperature, the layer charge and cation exchange capacity (CEC) of both smectites decreased gradually due to Li fixation. At temperatures >200ºC, ~25% residual CEC was observed, suggesting incomplete Li fixation due to kinetic constraints. Dehydration of the original Li-smectites occurred in two steps, one peaking at ~100ºC and another at 175−180ºC. The latter decreased upon progressive Li fixation and vanished from smectites treated above ~125ºC. Dehydroxylation occurred at 635−640ºC in both smectites and was not affected by Li fixation. The second derivative analysis of the infrared spectra showed that Li fixation was manifested in both smectites by the growth of two new sharp OH-stretching fundamentals at ~3640 and 3670 cm^{-1} and their overtones at ~7115 and 7170 cm^{-1}. The new bands constitute pairs of fixed energy and relative intensity which grow simultaneously at the expense of the broad OH-stretching and overtone features of the original smectites. Based on this result, Li fixation is suggested to be accompanied by the simultaneous formation of two distinct trioctahedral-like structural OH species, which is compatible with Li^+ occupying *trans*-octahedral vacancies in both smectites.

Key Words—Attenuated Total Reflectance Spectroscopy, Hofmann-Klemen Effect, Layer Charge, Li Fixation, Near Infrared Spectroscopy, Residual Cation Exchange Capacity, Smectite, *Trans*-vacant.

INTRODUCTION

Smectites are clay minerals with important physical and chemical properties, stemming from their crystal-chemical characteristics, their very small particle size, and the correspondingly large specific surface area. Properties of smectite valued by industry include CEC, swelling and rheological properties, hydration and dehydration, high plasticity, bonding capacity, and the ability to interact with inorganic and organic reagents (Odom, 1984). A key determinant of these properties is the layer charge which is due to substitutions in the tetrahedral and/or the octahedral sheet, or to the existence of vacancies in the octahedral sheet. The layer charge is associated with CEC and ion-exchange selectivity (Maes and Cremers, 1977, 1978; Shainberg *et al.*, 1987; Güven, 1992; Laird, 1999). Layer charge has been shown to be related also to the colloidal properties of smectites such as swelling (Slade *et al.*, 1991; Laird, 2006; Christidis *et al.*, 2006), especially if heterogeneity in charge magnitude and localization is also considered (Christidis and Eberl, 2003). Moreover, the magnitude of the layer charge is related to the adsorption of organic compounds on the smectite surface (Laird *et al.*, 1992).

Reduced-charge smectites result from the thermal treatment of Li-saturated dioctahedral smectites with octahedral charge. The process, known as the Hofmann-Klemen effect (Hofmann and Klemen, 1950), leads to the reduction of the layer charge and is manifested by the decrease in the CEC and the loss of the expandable character of the smectites. Apparently, heating induces the dehydration of Li cations and their migration into the layer structure of the mineral, where they become fixed, *i.e.* resistant to cation exchange. Suggested positions of Li^+ ions in the structure include the vacant octahedral sites (Hofmann and Klemen, 1950; Green-Kelly, 1953; Sposito *et al.*, 1983; Srasra *et al.*, 1994; Muller *et al.*, 1997; Stackhouse and Coveney, 2002; Madejová *et al.*, 2006), the ditrigonal cavities of the tetrahedral sheet (Tettenhorst, 1962; Luca *et al.*, 1989; Alvero *et al.*, 1994; Theng *et al.*, 1997), or both (Brindley and Ertem, 1971; Calvet and Prost, 1971; Madejová *et al.*, 1996; Karakassides *et al.*, 1999). The Hofmann-Klemen effect is specific to smectites with octahedral charge and was initially proposed as a method to distinguish montmorillonite from beidellite, a 2:1 phyllosilicate with tetrahedral layer charge (Green-Kelly, 1953).

* E-mail address of corresponding author:
christid@mred.tuc.gr
DOI: 10.1346/CCMN.2013.0610207

The aforementioned structural interpretations all stem from a remarkably uniform phenomenology of the Hofmann-Klemen effect. The amount of fixed Li^+ increases with temperature (Calvet and Prost, 1971) and reaches a plateau at ~220ºC (Brindley and Ertem, 1971; Komadel *et al.*, 1996). This result is common to many different smectites with variable composition and layer charge (Komadel *et al.*, 1996; Gates *et al.*, 2000; Madejová *et al.*, 2000a, 2000b; Bujdák *et al.*, 2001). In all these studies the reduction of layer charge with Li fixation was monitored indirectly by measuring the CEC of the smectites. Interestingly, Li^+-exchanged montmorillonite samples heated to complete fixation display CEC values that are greater than those expected from the complete reduction of their octahedral charge (Brindley and Ertem, 1971; Lim and Jackson, 1986; Jaynes and Bigham, 1987; Komadel, 2003). For example, a Li^+-exchanged Otay montmorillonite (SCa-2) with ~95% octahedral charge was reported to undergo a reduction of CEC by only 81% as a result of heating at 300ºC (Hrobáriková *et al.*, 2001; Komadel, 2003). The observed discrepancy has been attributed to the existence of mechanisms of Li fixation which do not lead to charge reduction (*e.g.* fixation in the interlayer and/or replacement of the structural OH groups by O^-Li^+, Jaynes and Bigham, 1987) or to the incomplete replacement of exchangeable cations during the initial Li-exchange process (Hrobáriková *et al.*, 2001).

Since the early work of Calvet and Prost (1971), infrared (IR) spectroscopy has been by far the most widely used technique for the structural characterization of reduced-charge smectites. Mid- and near-IR studies on Li-exchanged and heated (>120ºC) montmorillonite samples have linked the Hofmann-Klemen effect to the appearance of new sharp absorption bands corresponding to the stretching, bending, combination, and overtone modes of structural OH groups (Sposito *et al.*, 1983; Madejová *et al.*, 1996; 2000a, 2000b; Hrobáriková *et al.*, 2001; Gates, 2005; Madejová, 2005; Madejová and Komadel, 2005). By analogy to trioctahedral smectites which also exhibit sharp OH bands at similar positions (Russell and Fraser, 1994), the IR spectra of reduced-charge montmorillonites have been interpreted as suggesting the formation of local trioctahedral domains of the AlMgLiOH or AlAlLiOH types (Calvet and Prost, 1971; Srasra *et al.*, 1994; Madejová *et al.*, 2000a, 2000b). Alternatively, based on an earlier study on micas (Besson and Drits, 1997a, 1997b), Zviagina *et al.* (2004) assigned the new OH bands to pyrophyllite-like fragments in the dioctahedral 2:1 phyllosilicates.

The present study revisits the structural aspects of layer-charge reduction of two nearly ideal montmorillonites (*i.e.* with negligible tetrahedral charge) which differ in terms of octahedral charge. In addition to determining the CEC of the samples with progressively reduced charge, Li fixation was monitored by systematic measurements of the layer charge by X-ray diffraction (XRD) after K-saturation (Christidis and Eberl, 2003). In principle, the use of layer charge as a proxy to monitor Li fixation is more appropriate than CEC, as it records directly the outcome of the Hofmann-Klemen effect. The monitoring of Li fixation with layer-charge measurements was reported by Maes *et al.* (1979). However, the alkylammonium method employed by these latter authors has been suggested to underestimate layer charge by up to 40% (Laird and Fleming, 2008).

In addition to layer-charge measurements, the same samples were evaluated by attenuated total reflectance in the mid-IR (ATR-FTIR) range and diffuse reflectance (DRIFT) in the near-IR range. Besides allowing comparisons with previous literature, the aim of this vibrational investigation was to bring forward a more detailed study of the sharp features which develop upon fixation by taking advantage of second derivative analysis (Gionis *et al.*, 2006, 2007). Finally, the study is complemented by thermogravimetric analysis (TGA) to allow for the quantitative assessment of dehydration and dehydroxylation in reduced-charge montmorillonites as a function of heating temperature and to build on early results by Alba *et al.* (1998).

MATERIALS AND METHODS

Preparation of reduced-charge samples

Reduced-charge montmorillonite (RCM) preparations were based on two samples with minimum tetrahedral and different octahedral charge: SAz-1 (The Clay Minerals Society Source Clays Repository) is a typical high-charge montmorillonite and FEO-G (Christidis, 2006) is a low-charge montmorillonite from the Polycanthos area, Cyprus. Both samples have a small Fe content. Their chemical compositions (microprobe analysis, <0.2 μm fraction) and structural formulae are compared in Table 1. According to these analyses, the layer charge of neat SAz-1 and FEO-G are 0.54 and 0.39 e/huc, respectively (Gates, 2005; Christidis, 2006). The RCMs were prepared from the <2 μm fraction of SAz-1 and from a hand-crushed sample of FEO-G, due to the limited availability of the latter stock material. The SAz-1-based RCMs contain minor quartz and feldspar (2.5% in total) and clinoptilolite (1%) and the FEO-G-based RCMs contain minor quartz (4%), kaolinite (~3%), opal-CT, and illite (1−2%) (Christidis, 2006). The two clays were saturated with Li^+ at ambient temperature (for 2×12 h in 1 M LiCl solution, at a 1:100 clay/LiCl solution ratio), washed with ethanol until free of excess salts ($AgNO_3$ test), dried at 60ºC, and crushed with pestle and mortar. This standard experimental approach was assumed to lead to complete Li saturation (Bain and Smith, 1987). Portions (~500 mg) of these Li-saturated samples were heated for 24 h to a temperature in the range 60−300±5ºC. These samples are referred to as LiSAz-1_xxx or LiFEO-G_xxx, where xxx indicates the heating temperature. Due to sample shortage, Li-FEO-G was heated only at 60, 120, 200, and 300ºC.

Table 1. Chemical analysis and structural formulae of the SAz-1 montmorillonite (Gates, 2005) and the FEO-G montmorillonite (Christidis, 2006). The chemical composition of FEO-G was obtained from microprobe analysis. The chemical analysis of SAz-1 was reported on a LOI-free basis.

	FEO-G	SAz-1
SiO_2	60.67	67.59
Al_2O_3	21.05	19.85
Fe_2O_3	0.87	1.71
MgO	3.81	6.508
CaO	0.5	3.919
Na_2O	2.24	0.118
TiO_2	N/A	0.28
MnO	N/A	0.035
K_2O	0	0.074
Total	89.13	100.08
Structural formulae based on $O_{10}(OH)_2$		
Tetrahedral cations		
Si	3.97	3.99
Al^{IV}	0.03	0.01
Octahedral cations		
Al^{VI}	1.60	1.38
Fe^{3+}	0.04	0.07
Mg	0.36	0.56
Interlayer cations		
Ca	0.04	0.25
Mg	0.01	
Na	0.29	0.03
K	0	0
Layer charge	0.39	0.54
Interlayer charge	0.39	0.53
Tetrahedral charge (%)	7.7	2

Determination of layer charge and CEC

Layer charge was determined according to the method described by Christidis and Eberl (2003). The original samples and RCM preparations were K-saturated with 1 M KCl solutions, washed free of excess salts ($AgNO_3$ test), transferred to glass slides to make oriented clay mounts, left to dry at ambient temperature, and finally exposed to ethylene-glycol vapor at 60ºC overnight. The ethylene glycol-solvated samples were examined by XRD (Bruker AXS D8 Advance diffractometer) in the range 2–35º2θ, using CuKα radiation, with a step size of 0.02º2θ and 0.3 s counting time per step. The layer charge was determined on the basis of the XRD data using the *LayerCharge* computer code (Christidis and Eberl, 2003). A conservative estimate of the error associated with this determination of the layer charge is ±0.02 e/huc. The method has a lower threshold for determination of layer charge of 0.39 e/huc, which precluded the study of FEO-G-based RCMs.

The CEC of all samples was determined with a homebuilt Kjeldahl microsteam apparatus, after saturation with 1 M ammonium acetate at pH 7. Approximately 300 mg of each sample was saturated twice overnight with 10 mL of 1 M ammonium acetate, washed free of excess salts, and heated together with excess NaOH (~30 mL, 5 N) in the Kjeldahl reactor. The product of the distillation (ammonia) was collected in a conical flask containing 25 mL of boric acid (1 N) and methyl red and bromocresol green indicators, followed by titration with 0.05 N sulfuric acid. The error associated with this titration is of the order of ±2 cmol/kg, but the error of the overall determination is larger for samples with very low CEC, due to difficulties associated with their expansion and NH_4^+ exchange. The CEC data are expressed per 100 g of clay dried at 260ºC, using the weight-loss results obtained from TGA (see below). Before CEC determination, the samples had been dried at 60ºC. Drying at 105ºC was avoided because Li migration was observed to take place at this temperature.

TGA and IR spectroscopy

Small portions of each sample (~50 mg) were analyzed with an automated TGA system (TGA-6, Perkin Elmer). Both TG and DTG curves were obtained. The samples were heated gradually from 40 to 900ºC at a heating rate of 10ºC/min under a flow of dry N_2 gas. The sample weight was measured at intervals of 1.5ºC. The dehydroxylation temperatures were obtained from the DTG curves.

All IR spectra were measured on neat powder samples equilibrated to ambient temperature (25ºC, 30–35% RH). Mid-IR spectra (525–4000 cm^{-1}) were measured on a Fourier-transform instrument (Equinox 55 by Bruker Optics) equipped with a single-reflection diamond ATR accessory (DuraSamplIR II by SensIR Technologies). Contact between the powder samples and the diamond element was ensured by a suitable press, applying a pressure of ~100 MPa. Each spectrum represents the average of 300 scans recorded at an optical resolution of 2 cm^{-1} (digital resolution 1 cm^{-1}). The spectra are shown in the absorption mode after correction for the wavelength dependence of the penetration depth. The NIR spectra (3600–12000 cm^{-1}) were measured on a Fourier-transform spectrometer (Vector 22/N by Bruker Optics) equipped with an integrating sphere accessory. All spectra were measured against a gold reference and shown in the absorption mode. Each spectrum is the average of 200 scans at an optical resolution of 4 cm^{-1} and digital resolution of 2 cm^{-1}. The 2nd derivatives of the mid- or near-IR absorption spectra were calculated using the Savitzky-Golay algorithm (*Opus* software, Bruker) to allow for the identification of weak sharp features overlapping with broad bands. Typically, a 13-point smoothing window was employed, unless otherwise indicated.

RESULTS AND DISCUSSION

Layer charge and CEC of the reduced-charge smectites

Application of the Greene-Kelly test to SAz-1 at different temperatures resulted in systematic variations of the XRD traces of K-saturated, ethylene glycol-solvated samples (Figure 1). These XRD traces are comparable to those of natural samples and suggest a progressive change from high-charge to low-charge smectite. The first-order reflection peak of the K-saturated LiSAz-1_060 occurred at 6.42º2θ (d_{001} = 13.7 Å), and shifted gradually upon heating at 135ºC to 5.14º2θ (d_{001} = 17.1 Å). The XRD traces of samples LiSAz-1_060-100 exhibited d_{001} spacings of <15 Å and d_{003} spacings at ~4.70 Å. These traces are, therefore, typical of high-charge smectites (layer charge >0.475 e/huc) according to Christidis *et al.* (2006). RCMs heated between 105 and 115ºC exhibited d_{001} at 16.5−15.5 Å and irrational *d* spacings of higher-order basal reflections which are typical of smectites with intermediate layer charge (0.46−0.44 e/huc). Heating at 120−135ºC decreased the layer charge further, as in low layer-charge smectites (0.42−0.39 e/huc) which are characterized by a >16.6 Å 001 diffraction maximum and rational, higher-order basal reflections (Christidis *et al.*, 2006). Above 130ºC, the first-order reflection decreased quickly in intensity while remaining fixed in position (Figure 1). Indeed, the layer charge of

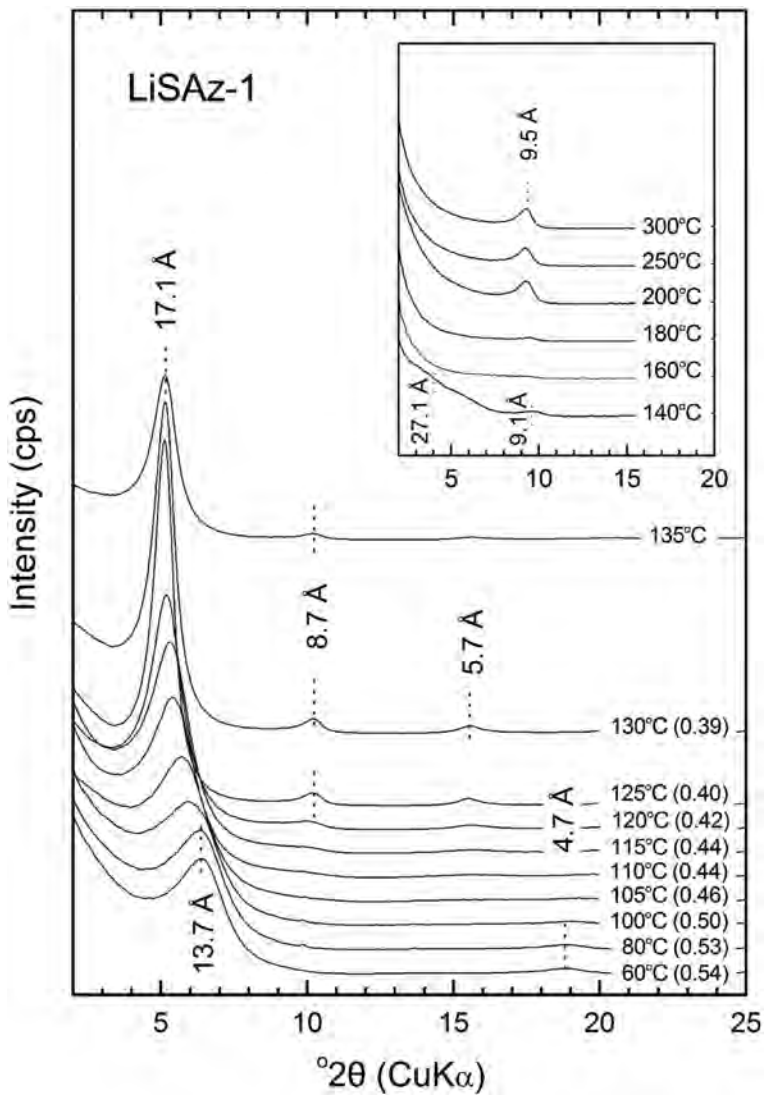

Figure 1. Room-temperature XRD patterns of K-saturated and ethylene glycol-solvated LiSAz-1 samples previously subjected to heating in the 60−135ºC range for 24 h. Note the shift of d_{001} from ~13.7 Å (60ºC) to 17.1 Å (135ºC). Charges (e/huc) calculated according to Christidis and Eberl (2003) are shown in parentheses. The inset shows the patterns of the corresponding samples heated at higher temperatures and up to 300ºC. Note the appearance of a new peak ~9.5 Å which is indicative of collapsed montmorillonite layers.

LiSAz-1_130 and LiSAz-1_135 was found to be 0.39 e/huc (Table 2) and was probably overestimated because this value coincides with the detection limit of the Christidis and Eberl (2003) method. For the same reason, the layer charges of LiFEO-G-based RCMs cannot be estimated correctly. Samples LiSAz-1_140–180 displayed broad diffraction maxima between 4 and 5º2θ and another diffraction maximum at ~9.8º2θ (9.1 Å), indicating the existence of a superstructure due to ordered interstratification of totally collapsed and expandable smectite layers. The progressive appearance of a new diffraction maximum with d = 9.5 Å in samples LiSAz-1_180–300 indicated the presence of completely collapsed montmorillonite layers (Sato *et al.*, 1992). The lack of a diffraction maximum at 5º2θ in these samples was compatible with the negligible tetrahedral charge of SAz-1. This is because montmorillonites with a significant proportion of tetrahedral charge display diffraction maxima both at 5º2θ and at 9.3º2θ, after the completion of the Greene-Kelly test, due to the existence of discrete phases or to mixed-layer montmorillonite-beidellite (Lim and Jackson, 1986; Guisseau *et al.*, 2007). Application of the Greene-Kelly test to FEO-G at 120, 200, and 300ºC yielded identical results to SAz-1 (data not shown). In summary, the position of the 001 diffraction maximum was not affected after heating at 120ºC, but shifted to ~9.3º2θ (9.5 Å) after heating at 200 and 300ºC.

The CEC values of LiSAz-1 sample series (Table 2) displayed a sigmoidal dependence on the heating temperature from ~130 to ~40 cmol/kg with a midpoint at ~120ºC (Figure 2). The overall trend is similar to that reported by Madejová *et al.* (2000a, 2000b) and Bujdák *et al.* (2001), the main difference being the smaller final CEC value reported by the latter authors. Fewer data points exist for the LiFEO-G system, but the observed % reduction of the CEC with heating temperature was comparable to that of LiSAz-1, suggesting that the two montmorillonites respond to Li fixation in a very similar manner despite differences in their initial layer charge.

Measured layer charges follow well the trend of the CEC data up to 120–125ºC, and then level off toward 0.39 e/huc (Figure 2, inset). This value is the lower detection limit of the layer-charge determination method employed, because it corresponds to a material consisting solely of low-charge smectitic layers (Christidis and Eberl, 2003). Interestingly, a similar leveling off was observed in the data of Maes *et al.* (1979) who used the alkylammonium method to measure the layer charges of RCMs based on montmorillonite from Camp Berteau (Morocco).

The CEC of the Li samples heated at temperatures >200ºC was greater than that expected from complete charge reduction and the residual CEC did not depend on the layer charge of the original samples (Figure 2). The compensation of deprotonated hydroxyl groups (Jaynes and Bigham, 1987) and the incomplete replacement of exchangeable cations during Li-exchange (Hrobarikova *et al.*, 2001) might explain the observed trends. However, the former option, while significant in the case of Fe-rich smectites including nontronites (Russell, 1979; Jaynes and Bigham, 1987), is less important in the case of Al-Mg, Fe-poor montmorillonites, especially

Table 2. CEC, layer charge, weight % loss in the 40–260ºC, and dehydroxylation regions of the reduced-charge LiSAz-1 and LiFEO-G samples. Weight loss % data are expressed with reference to the weight of the samples at 260ºC.

Sample	CEC (cmol/kg)	% of CEC_{060}	Layer charge (e/huc)	Weight loss, % (40–260ºC)	Weight loss, % (260–900ºC)
LiSAz-1_060	131.6	100.00	0.54	16.45	4.58
LiSAz-1_080	131.6	100.00	0.53	16.45	4.58
LiSAz-1_100	126.7	96.25	0.50	15.87	4.53
LiSAz-1_105	119.9	91.12	0.46	15.29	4.48
LiSAz-1_110	113.8	86.49	0.44	15.26	4.58
LiSAz-1_115	107.7	81.86	0.44	14.61	4.50
LiSAz-1_120	96.1	73.05	0.42	12.21	4.78
LiSAz-1_125	89.8	68.21	0.40	9.81	5.07
LiSAz-1_130	75.6	57.42	0.39	9.15	5.18
LiSAz-1_135	62.2	47.29	(0.39)	6.94	5.77
LiSAz-1_140	57.7	43.84	–	5.41	5.27
LiSAz-1_160	53.2	40.39	–	3.88	4.92
LiSAz-1_180	46.5	35.37	–	3.01	5.23
LiSAz-1_200	34.8	26.45	–	2.33	5.70
LiSAz-1_250	36.7	27.89	–	1.95	4.83
LiSAz-1_300	39.5	30.04	–	2.11	5.03
LiFEO-G_060	89.2	100.00	0.39	9.09	5.89
LiFEO-G_120	67.7	75.93	–	5.92	5.78
LiFEO-G_200	29.0	32.52	–	2.33	5.37
LiFEO-G_300	24.3	27.25	–	2.15	5.05

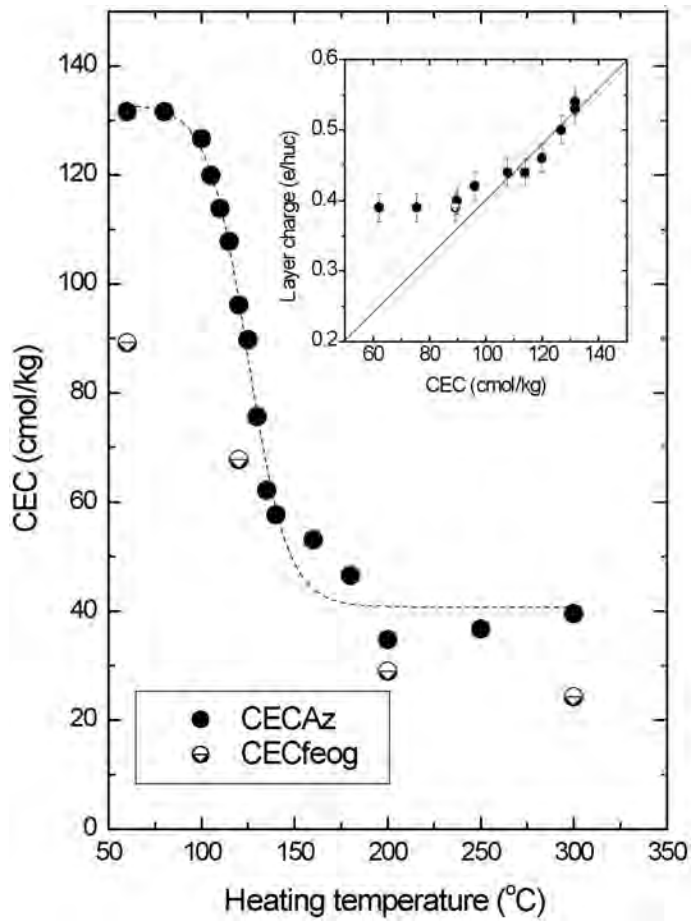

Figure 2. Dependence of CEC on the heating temperature of LiSAz-1 and LiFEO-G. The sigmoidal line is a guide to the eye through the LiSAz-1 dataset. The inset compares the layer charge and CEC data of the same samples (Table 2).

those with low layer charge (Jaynes and Bigham, 1987), such as the FEO-G examined here. Also, incomplete Li exchange is not considered significant because the two smectites studied displayed similar behavior, although they had different layer charge. Indeed, had this been the case, the fraction of the residual CEC would have been smaller in the low-charge FEO-G smectite (*e.g.* Maes and Cremers, 1978).

The possible influence of variable charge on the residual CEC was also examined. The CEC calculated from the structural formulae for the layer charges of the original and the RCMs (Table 1) was compared to the CEC from ammonium acetate. The difference between the two values varied from +7.1 to −7.7% with respect to the ammonium acetate CEC, the average difference being ~+1% of the CEC. The CEC of the original FeO-G determined by ammonium acetate is almost identical to the CEC derived from Table 1, assuming 5% structural H_2O, *i.e.* 99.1 cmol/kg (104.5 cmol/kg on an anhydrous basis). The <2 μm fraction of FeO-G contains ~8−9% impurities (3% kaolinite, 4% quartz, the rest being opal-CT and illite). The CEC of pure smectite determined by ammonium acetate was, therefore, 97−98 cmol/kg (102−103 cmol/kg on an anhydrous basis) *i.e.* almost identical to the value calculated. Similarly, the CEC of SAz-1 calculated from Table 1 was 136.1 cmol/kg (143.3 cmol/kg on an anhydrous basis). The sample contained ~2.5% quartz and feldspar and ~1% clinoptilolite. Clinoptilolite increased the CEC determined by ammonium acetate by ~0.6 cmol/kg. Hence the actual CEC of the SAz-1 smectite as determined by ammonium acetate is 134.4 cmol/kg (141.5 cmol/kg on an anhydrous basis). Therefore, the variable charges in the present case cannot explain the residual CEC. This is expected, as the CEC measurements were performed at pH 7, *i.e.* close to the iep of the edges of smectite (*e.g.* Tombacz and Szekeres, 2004).

An alternative explanation is to consider that the Green-Kelly test does not lead to complete reduction of the octahedral layer charge. By definition, smectites have layer charges of 0.2−0.6 e/huc and swell under addition of glycerol and/or ethylene glycol vapors (Brigatti *et al.*, 2006). Hence, 2:1 phyllosilicates with layer charges of <0.2 e/huc are not expected to swell.

Interstratification between collapsed layers and swelling layers was observed in samples heated at 140ºC but was absent from samples heated at higher temperatures (Figure 1). Hence, in samples heated above 200ºC the possible remaining empty octahedral sites next to Mg-bearing octahedral sites are not clustered in swelling domains but are randomly dispersed. Such an arrangement of octahedra which were not occupied by Li for the SAz-1 montmorillonite (Figure 3) would not cause swelling of the smectite layers. Indeed, if 25% of the available octahedra remained vacant, they would account for residual layer charge of 0.145 e/huc or a CEC of 35 cmol/kg, observed in the present study.

TGA analysis

The DTGA thermograms of the RCMs based on LiSAz-1 exhibited a systematic dependence on the temperature of Li fixation (Figure 4). This dependence was mainly manifested by drastic changes of the low-temperature thermogravimetric envelope (<260ºC) in terms of both complexity and integrated intensity. Events in this range are attributed to dehydration processes. The first event, peaking at ~100ºC in LiSAz-1_060, corresponds to the loss of adsorbed water.

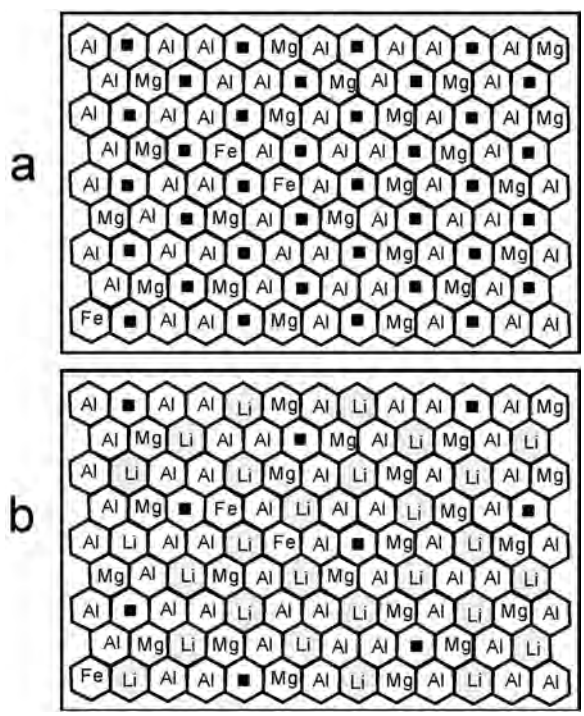

Figure 3. Schematic diagram showing the process of incomplete charge reduction in SAz-1 Li-montmorillonite heated at temperatures >200ºC. (a) Representation of the octahedral sheet of SAz-1 montmorillonite. (b) Representation of the octahedral sheet after charge reduction. 25% of the vacant octahedra were not filled by Li during the Green-Kelly test. The octahedra with black squares are vacant, whereas those shaded are filled with Li.

A second event, centered at 175−180ºC, was observed as a shoulder in samples subjected to low fixation temperatures. Its amplitude decreased abruptly at temperatures exceeding 115ºC and vanished at ~130ºC, *i.e.* a range which coincides with the appearance of interstratified structures between collapsed and swelling smectite layers (Figure 4). A similar high-temperature dehydration event has typically been observed in smectites saturated with Ca^{2+}, Mg^{2+}, or Li^{+} and attributed to H_2O in the coordination sphere of these high field strength interlayer cations (Alba *et al.*, 1998). An alternative explanation to H_2O interacting with localized tetrahedral charge (Koster van Groos and Guggenheim, 1987) should be ruled out in the case of SAz-1 and FEO-G.

The total weight % loss in the 40−260ºC range is expressed against the weight measured at 260ºC and is included in Table 2. This quantity exhibits a sigmoidal dependence on the fixation temperature which is similar to that of CEC (Figure 2) and, therefore, weight % loss and CEC are linearly related (R^2 = 0.97, σ = 1 wt.%, graph not shown). Finally, the high-temperature event in the DTGA data corresponds to the dehydroxylation of the smectite. It was observed (Figure 4) as nearly independent of the Li-fixation temperature in both position (635−640ºC) and integrated intensity (4.9±0.4 wt.%, Table 2). The dehydroxylation temperature of the RCMs based on LiSAz-1 is very similar to that of neat SAz-1 montmorillonite (633−639ºC, Guggenheim and Koster van Groos, 2001) and the corresponding weight % loss was identical to that predicted theoretically (4.8 wt.%). The four RCM samples based on LiFEO-G exhibited very similar phenomenology (Table 2). The greater weight loss observed was compatible with the presence of minor kaolinite.

IR spectroscopy

The ATR and NIR spectra of several RCMs based on LiSAZ-1 and spanning the whole range of fixation temperatures (60−300ºC) are shown in Figure 5. Besides trivial details due to differences in the optical setups employed, these spectra are identical to those published by Madejová *et al.* (2000a, 2000b) for the same system. In agreement with the TGA data, both spectral series are characterized by the very pronounced intensity reduction of H_2O bands upon increasing fixation temperature. These bands dominate the spectra at 1635 cm^{-1}, 3000−3900 cm^{-1}, 4900−5400 cm^{-1}, and 6500−7300 cm^{-1}, and correspond to the bending (δ), stretching (ν_{01}), combination ($\nu_{01}+\delta$), and 1st overtone stretching (ν_{02}) envelopes, respectively (Bishop *et al.*, 1994). Subtler but important changes were also observed in all other frequency ranges, including those of the structural OH-bending vibrations (950−675 cm^{-1}), Si−O stretching vibrations (1175−950 cm^{-1}), OH-stretching vibrations (3500−3700 cm^{-1}), combination modes (4300−4600 cm^{-1}), and overtone modes (7000−7200 cm^{-1}). Overall, Li fixation appeared to

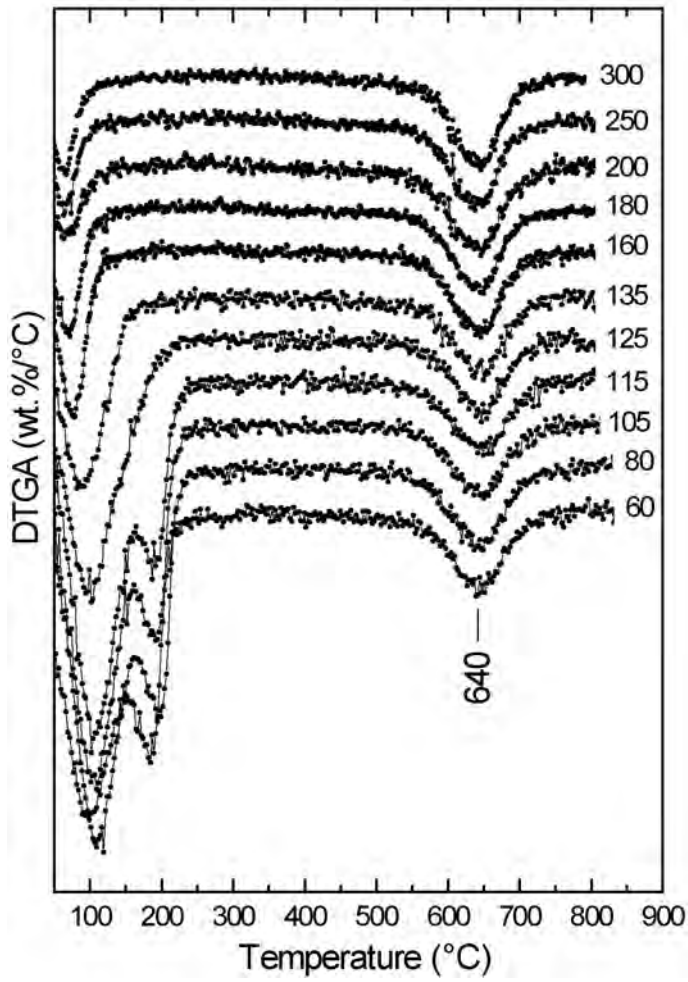

Figure 4. DTGA diagrams of the reduced-charge LiSAz-1 samples series as a function of heating in the 60−300ºC range. The data have been normalized to the weight of the samples at 260ºC and are shown offset for clarity.

involve the emergence of new sharp features. Therefore, their detailed study was based on comparing the 2nd derivative spectra, which offered enhanced sensitivity, especially at low fixation temperatures where these bands are weak and overlapping with the strong and broad envelopes of H_2O modes (Figure 6).

In agreement with previous literature (Sposito *et al.*, 1983; Madejová *et al.*, 1996; Karakassides *et al.*, 1997; Gates, 2005; Madejová and Komadel, 2005), the envelope of Si−O stretching modes shifted to higher temperatures upon increasing fixation temperature. The trend was best monitored *via* the emergence of a sharp feature at 1123 cm^{-1} (similar to a pyrophyllite band at ~1120 cm^{-1}, Russell and Fraser, 1994) at the expense of a mode at ~1110 cm^{-1} (Figure 5) which corresponds to an in-plane Si−O stretching mode (Johnston and Premachandra, 2001).

In the range of OH-bending modes (Farmer, 1974), LiSAz-1_060 exhibited well defined bands at 911, 836, and 787 cm^{-1} which are commonly assigned to AlAlOH, AlMgOH, and possibly FeMgOH species, respectively (Madejová and Komadel, 2005; Gates, 2005). The assignment of the 787 cm^{-1} band may be questionable in the case of LiSAz-1 because of the low Fe content of this clay (Gates, 2005). Instead, this band should be attributed to silicate impurities. Montmorillonite exhibits a variable position of the main AlAlOH stretch fundamental in the range 3615−3630 cm^{-1} (Madejová *et al.* 1994; Bishop *et al.* 2002; Zviagina *et al.* 2004) whereas the first stretching overtone is found at ~7055−7090 cm^{-1} (Clark *et al.*, 1990; Bishop *et al.*, 2002), both overlapping with H_2O modes. Within these ranges, LiSAz-1_060 occupies an end-member position with low-energy positions of the AlAlOH fundamental and overtone modes at 3615 cm^{-1} and 7056 cm^{-1}, respectively (determined from the 2nd derivative spectra). High-wavenumber shoulders to these bands were observed at ~3650 cm^{-1}, as well as at 7125 and 7160 cm^{-1} (Figure 6). Whether these shoulders are due to AlMgOH species (*e.g.* Madejová *et al.* 1994) or to

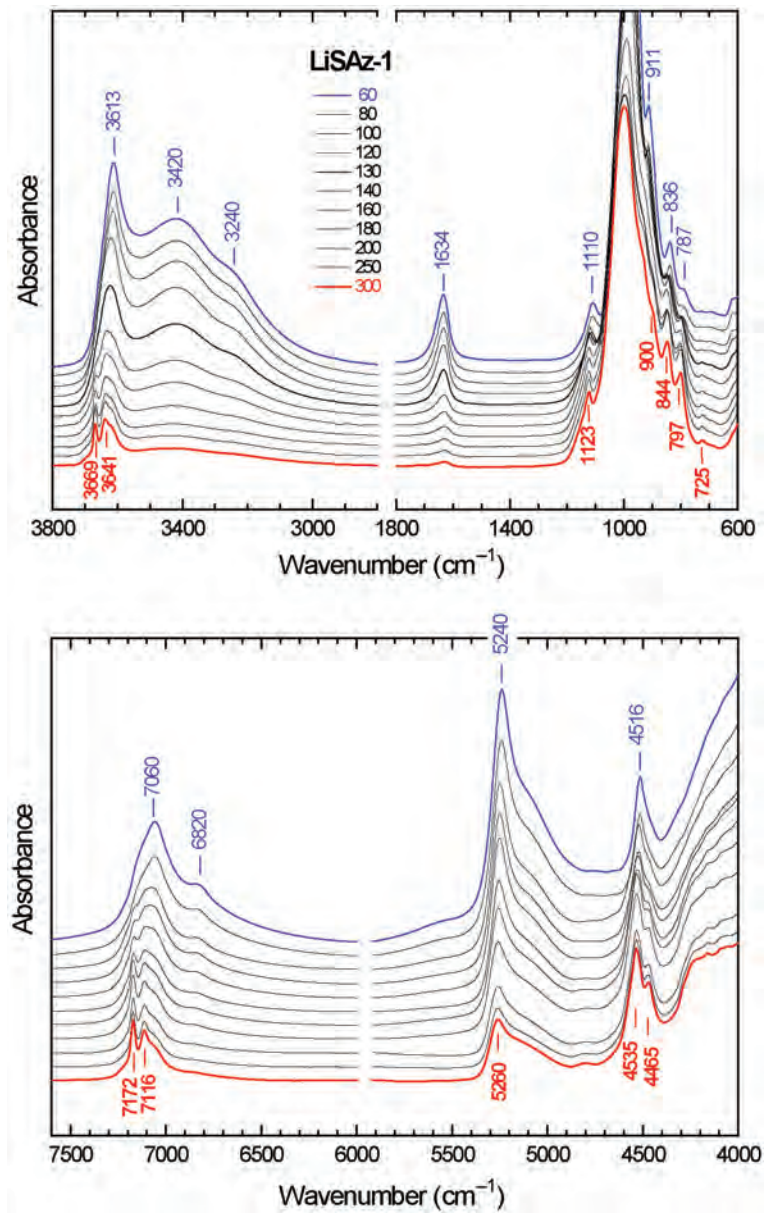

Figure 5. ATR (upper) and NIR (lower) absorption spectra of selected-reduced charge LiSAz-1 montmorillonites prepared by heating at various temperatures and fully equilibrated to ambient temperature. The spectra are offset for clarity and baseline corrected in the 6000−8000 cm^{-1} range.

pyrophyllite-type domains (Zviagina *et al.*, 2004) is not clear. Finally, the AlAlOH stretching-bending combination mode of dioctahedral aluminous smectites is typically observed in the 4520−4550 cm^{-1} range depending on composition (Post and Noble, 1993; Gates, 2005). LiSAz-1_060 exhibited this mode at 4518 cm^{-1} as a combination of the 911 and 3615 cm^{-1} fundamentals. A lower-wavenumber contribution at ~4445 cm^{-1} (Figure 6) is attributed to the corresponding AlMgOH combination mode (Gates, 2005).

Increasing Li fixation induces significant changes to the 2nd derivative spectra (Figure 6). A doublet of new OH-stretching fundamentals at 3641 and 3669 cm^{-1} (Δ = 28 cm^{-1}) grew progressively with increasing fixation temperature, accompanied by the corresponding overtones at 7116 and 7172 cm^{-1} (Δ = 56 cm^{-1}). In the range of the OH-bending fundamentals, new bands appeared at 797, 844, 896, and 927 cm^{-1}. Stretching-bending combinations were dominated by a sharp doublet at 4465 and 4538 cm^{-1} (Δ = 73 cm^{-1}), a higher-energy component below ~4570 cm^{-1}, and a number of low-wavenumber features below 4300 cm^{-1}. These spectral changes were resolved already upon heating at 100ºC and then evolved in parallel suggesting that their

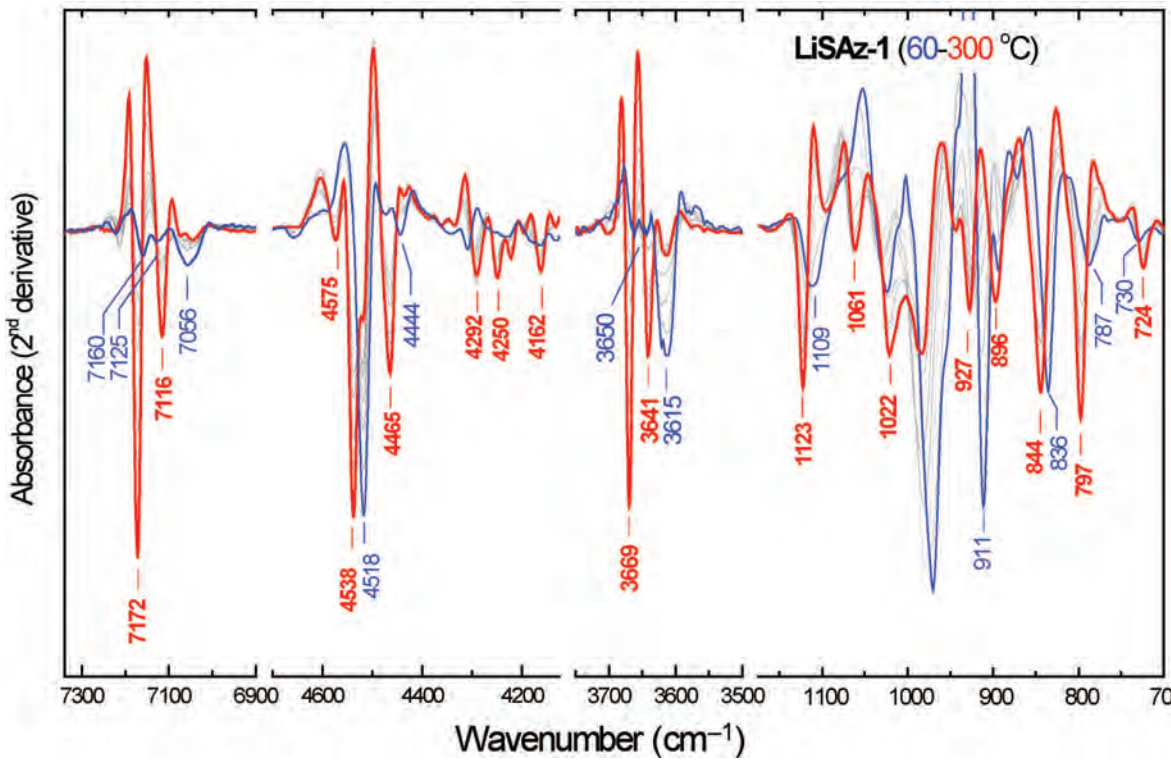

Figure 6. Second derivative absorption spectra of the RCM's based on LiSAz-1 over four ATR and NIR wavenumber ranges. The spectra corresponding to the lowest and highest fixation temperatures (60 and 300ºC) are shown using thick and thin lines (blue and red in the online version), respectively.

ensemble constituted the unique vibrational signature of Li fixation in SAz-1.

This description above of the spectral changes accompanying Li fixation is very similar to that reported by several authors on the basis of absorption spectra (Calvet and Prost, 1971; Madejová *et al.*, 2000a, 2000b; Petit *et al.*, 2004), with one subtle but important difference. These authors described the evolution in the OH-stretching (or overtone) range as the convolution of two processes: the progressive shift of the main ν_{01} (ν_{02}) OH mode of unheated montmorillonite towards 3641 cm^{-1} (7116 cm^{-1}) and the emergence of a new peak at 3669 cm^{-1} (7172 cm^{-1}). On the contrary, the 2nd derivative analysis demonstrates that the 3641 and 3669 cm^{-1} bands and their overtones at 7116 and 7172 cm^{-1} constitute pairs of fixed relative intensity which grow simultaneously at the expense of the broader 3615 (7056) cm^{-1} modes of unheated SAz-1. Moreover, the position and relative intensity of the component bands of the pair in the LiFEO-G system were identical to that of LiSAz-1, despite the large difference in octahedral layer charge of the two clay minerals (Figure 7). Stretching fundamental and overtone-OH modes at nearly identical positions were reported by Petit *et al*. (2002) for charge-reduced Fe-rich montmorillonite from Ölberg, Germany. Furthermore, the published IR absorption spectra of several reduced-charge montmorillonites with different octahedral charges suggest a very similar phenomenology. Prior to any heat treatment, the positions of their OH-stretching and overtone bands were quite variable, but when Li fixation was complete these converged to ~3640, 3670 cm^{-1} or 7110, 7170 cm^{-1}, respectively (Hrobáriková *et al.* 2001; Madejová *et al.*, 2000a, 2000b; Madejová, 2005).

Clearly, a unique self-consistent set of assignments is needed to describe the common vibrational signature of the Li-induced octahedral charge-reduction mechanism in montmorillonite.

Local structure of RCMs

A good starting point in deciphering the structure of RCMs is the assignment of the two ν_{01} bands at ~3640 and 3670 cm^{-1} and their ν_{02} counterparts at ~7115, 7170 cm^{-1}. These bands are attributed to structural OH species of the reduced-charge clay. However, their characteristic wavenumbers are intermediate to those typically encountered in dioctahedral and trioctahedral smectites (Farmer, 1974; Clark *et al.* 1990; Russell and Fraser, 1994) and could be assigned to either type of octahedral sheet. Even in the simplest case of neutral aluminous dioctahedral 2:1 clay minerals, the position of the AlAlOH stretching fundamental mode is highly variable. For example, in hydrated palygorskite, this

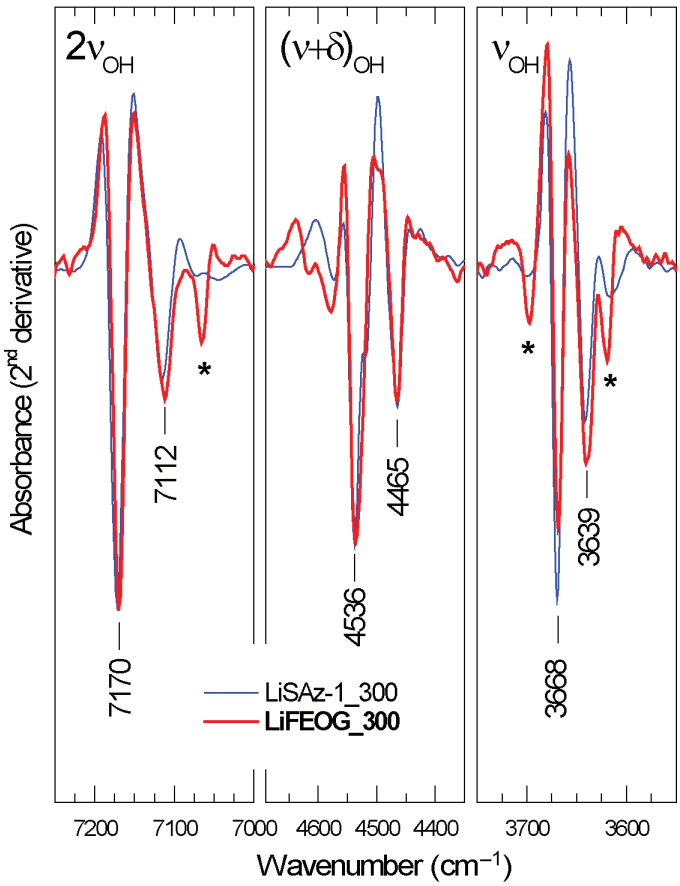

Figure 7. Comparison of the OH-stretching combination and overtone 2nd derivative spectra of LiFEO-G (thick line, red in online version) and LiSAz-1 (thin line, blue in online version) subjected to Li fixation at 300ºC. The spectrum of LiFEO-G is shown multiplied by a factor of 5. Peak positions correspond to LiFEO-G. Bands marked with asterisks are from a kaolinite ancillary phase.

mode is observed at 3615 cm^{-1}, shifting to 3624 cm^{-1} upon drying and to ~3645 cm^{-1} upon folding (VanScoyoc *et al.*, 1979; Gionis *et al.*, 2006). In pyrophyllite, it is observed at ~3675 cm^{-1}, *i.e.* in a position nearly identical to the Mg_3OH mode of talc (Russell and Fraser, 1994).

Insight into the nature of the new OH species can also be based on the anharmonicity values, $X = (2\nu_{01}-\nu_{02})/2$, which can be obtained with high precision from the 2nd derivative spectra. Thus, the data in Figure 6 indicate that both fundamental modes at ~3640 and 3670 cm^{-1} exhibit identical anharmonicity, $X = 83-84$ cm^{-1}, which is smaller than the value of $X = 87$ cm^{-1} of untreated montmorillonite SAz-1. The AlAlOH stretching of pyrophyllite with $\nu_{01} = 3675$ cm^{-1} and $\nu_{02} = 7177$ cm^{-1} (Russell and Fraser, 1994; Clark *et al.*, 1990; Kloprogge *et al.* 2000; Wang *et al.*, 2002) also yields $X = 87$ cm^{-1}. Values of anharmonicity in the range 87–88 cm^{-1} have also been reported for the AlAlOH, AlFeOH, and FeFeOH modes of (dioctahedral) palygorskite in both hydrated and dry states (Gionis *et al.*, 2006). These data indicate that the OH-stretching modes of dioctahedral 2:1 clay minerals exhibit rather uniform values of X, despite the aforementioned large energy variation of their fundamentals. In comparison, neutral trioctahedral 2:1 minerals such as talc or sepiolite have Mg_3OH stretching modes with lower anharmonicity values, $X = 84-85$ cm^{-1} (Petit *et al.*, 2004; Gionis *et al.*, 2007), closer to those observed in reduced-charge Li-montmorillonite. Based on the analysis above, the position of the OH-stretching modes alone is not useful in determining the exact nature of the absorbing species in RCMs, whereas the corresponding anharmonicity values point towards trioctahedral arrangements. The latter is in accordance with early reports for the pleochroism of these modes, which suggested that the OH bonds are perpendicular to the *ab* plane, as in trioctahedral minerals (Calvet and Prost, 1971). Then, the main question in interpreting the spectra is about a mechanism of charge reduction which could create simultaneously two OH-stretching modes (and their corresponding overtones) with fixed position and relative intensities.

That each type of OH species present yields a single OH-stretching (bending, *etc.*) vibrational mode is commonly accepted. Conversely, the number and

relative intensity of OH bands are used to identify the various types of OH present in smectites and estimate their relative abundance (Farmer 1974; Madejová *et al.*, 1994; Besson and Drits, 1997a, 1997b; Gates *et al.*, 2002; Zviagina *et al.*, 2004; Petit, 2005; Gates, 2005; Gionis *et al.*, 2007; Chryssikos *et al.*, 2009). Assuming that this rule of thumb applies also in the case of RCMs, two possible explanations for the emergence of two ν_{01} OH-stretching modes (and their ν_{02} counterparts) can be proposed. Either fixed Li^+ modifies two pre-existing (but poorly distinguishable) populations of OH species and produces an equal number of sharp bands, or Li^+ interacts with a single type of OH group in a manner that removes their degeneracy and produces two new distinct populations.

The first scenario is usually linked to the presence of octahedral substitution by homovalent cations, *e.g.* Fe^{3+} for Al^{3+} in dioctahedral phyllosilicates. For example, the 3641 cm^{-1} peak (Figures 5–6) could represent the AlFeOH counterpart of an AlAlOH pyrophyllite-type mode at 3669 cm^{-1} (*cf.* Russell and Fraser, 1994; Besson and Drits, 1997b; Lantenois *et al.*, 2007). Alternatively, the two bands could correspond to AlMgLiOH and FeMgLiOH species. In either case, the relative intensity of the 3641 *vs*. 3669 cm^{-1} peaks should scale with $x/(1-x)$, where x is the fraction of Fe^{3+} in the octahedral sites. Obviously, this scaling is not supported by the fact that these peaks are identified in both low-Fe (SAz-1, FEO-G, this study) and high-Fe montmorillonites (Petit *et al*., 2002).

The second scenario should involve the perturbation of AlMgOH in montmorillonite by Li^+. Two possibilities should be considered depending on whether the octahedral sheet is *cis*- or *trans*-vacant (*cv*, *tv*). In both cases, each Mg^{2+} cation substituting for Al^{3+} creates two crystallographically identical and energetically degenerate AlMgOH groups. Clearly, mechanisms of fixation capable of removing this degeneracy are required. One possibility would be to fit Li^+ inside a di-trigonal cavity of the tetrahedral sheet as suggested by some (Tettenhorst, 1962; Luca *et al.*, 1989; Alvero *et al.*, 1994; Theng *et al.*, 1997). In this manner, Li^+ would modify only one of the two AlMgOH groups. This type of mechanism would involve the coulombic interaction of Li^+ with the oxygen atom of the AlMgOH group and would lock the O-H dipole to a more tilted position with respect to the principal symmetry axis of the di-trigonal cavity. As such, this scenario is incompatible with the experimental finding that the OH groups of RCMs are perpendicular to the plane of the di-trigonal cavity (Calvet and Prost, 1971).

An alternative mechanism, which has been widely proposed to account for the spectra of RCMs and can remove the degeneracy of the OH groups, is the fixation of Li^+ inside octahedral vacancies (Figure 8). The presence of Li^+ would create local bonding rearrangements which would depend critically on the type of vacancy present. In the case of *cv* montmorillonite, one Li^+ cation occupying the M2a vacancy creates two equivalent AlMgLiOH groups (Figure 8, left), whereas the occupation of the M2b vacancy results in the formation of equivalent AlAlLiOH groups (not shown). In contrast, charge reduction involving the occupation of the M1a *trans*-vacancies by Li^+ is the only mechanism enabling the degeneracy removal of the pre-existing AlMgOH and AlAlOH units by creating AlMgLiOH and AlAlLiOH species in a 1:1 ratio (Figure 8, right). Clearly, this last scenario is compatible with the synchronous appearance of two sharp trioctahedral-like OH stretching (and overtone) modes with fixed position and relative intensity upon charge reduction. If the above argument is correct, the unique vibrational signature of RCMs (Figure 7) would be linked to the presence of *tv* domains in both montmorillonites, and these are more abundant in SAz-1 than in LiFEO-G.

According to Tsipurski and Drits (1984), montmorillonite can range from 100% *cv* (represented by a Wyoming low charge montmorillonite) to 100% *tv*, whereas illite, beidellite, and nontronite are considered to be primarily *trans*-vacant. However, a clear correlation between the composition or the charge of montmorillonite and the type of octahedral vacancy has not been established experimentally (Drits and Zviagina, 2009). The previous published IR studies have not suggested a distinction between the two types of octahedral domains in montmorillonite. As a result, the only practical estimation of the prevailing type of vacancy is based on the proposal by Drits *et al.* (1995), who related the type of vacancy in aluminous dioctahedral smectites indirectly to their temperature of dehydroxylation: *cv* smectites dehydroxylate at temperatures ~150–200ºC higher than their *tv* counterparts (*cf.* Wolters and Emmerich, 2007). A dehydration threshold between the two types (~600ºC) is commonly accepted, according to which SAz-1 and FEO-G (~635ºC) are on the low-end of the *cv* range. Theoretical modeling of *cv* and *tv* illites and smectites (Sainz-Diaz *at al.*, 2001) have suggested that *tv* configurations are slightly favored over their *cv* analogs upon increasing octahedral Mg content and layer charge. These studies would classify SAz-1 and FEO-G as *tv* smectites.

Clearly, the systematics of the octahedral vacancies in montmorillonite remain poorly understood. The present analysis suggests that Li^+ fixation followed by 2^{nd} derivative mid- or near-IR spectroscopy may enhance the 'structural contrast' between *cis*- and *trans*-vacancies, and therefore become a convenient tool for estimating their relative abundance.

CONCLUSIONS

The gradual reduction of the layer charge of two montmorillonites with different layer charge, due to the Hoffmann-Klemen effect, was studied by Li saturation

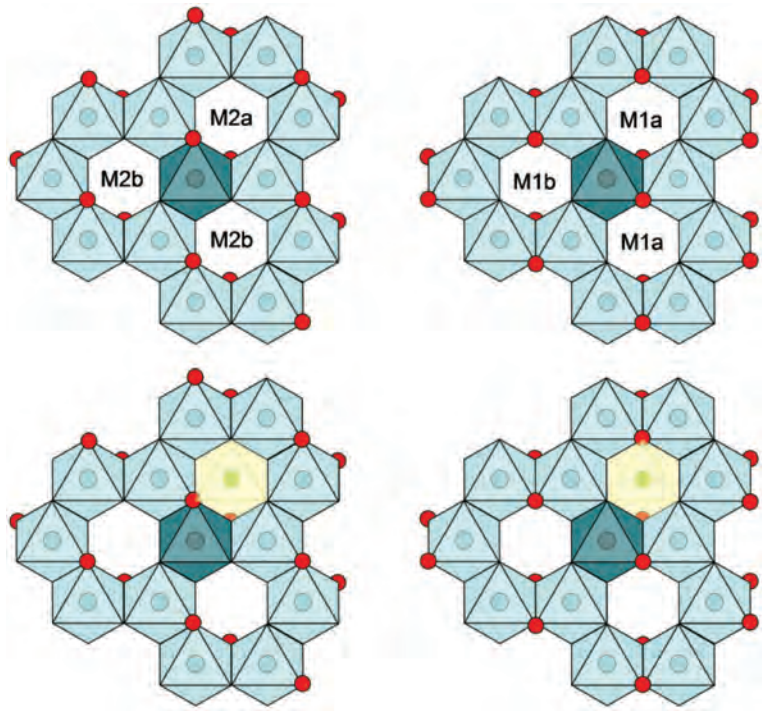

Figure 8. Schematic structure of the octahedral sheet in *cv* (upper left) and *tv* (upper right) montmorillonite with the structural OH groups shown as small spheres. Both arrangements result in two degenerate AlMgOH groups per octahedral Mg^{2+}. The AlAlOH groups are also degenerate in both cases. The degeneracy is preserved by Li^{+} fixation in either the M2a (lower left) or the M2b *cis* vacancy. The degeneracy of the two types of OH groups is removed only if Li^{+} occupies an M1a *trans*-octahedral vacancy (lower right), creating AlMgLiOH, AlAlLiOH units in addition to unperturbed AlMgOH and AlAlOH.

and heating at 80−300ºC. The migration of Li in vacant octahedral sites was accompanied by a decrease in layer charge, CEC, and the amount of adsorbed water, whereas the dehydroxylation temperature remained unaffected. In both smectites, a residual CEC was observed at the end of the experiments, which is attributed to residual vacant octahedral sites due to kinetic constraints. Upon Li migration to vacant octahedral sites, two new sharp OH-stretching fundamentals at ~3640 and 3670 cm^{-1} and their overtones at ~7115, 7170 cm^{-1} were observed in the FTIR spectra of both smectites. Various models of Li fixation capable of removing the degeneracy of the original AlMgOH species were examined. On this basis, the changes observed in the FTIR spectra after Li fixation were compatible with Li^{+} occupying *trans* octahedral vacancies in both smectites. The results of the present study will shed light on the *cis/trans* configuration of smectites and on their behavior at the low charge limit (0.2 e/huc).

ACKNOWLEDGMENTS

This work was funded by a Basic Research Grant to GEC by the Technical University of Crete, as well as by the Applied Spectroscopy Laboratory of TPCI/NHRF. The constructive comments of the Associate Editor and two anonymous reviewers improved the text.

REFERENCES

Alba, M.D., Alvero, R., Becerro, A.I., Castro, M.A., and Trillo, J.M. (1998) Chemical behaviour of lithium ions in reexpanded Li-montmorillonites. *Journal of Physical Chemistry B*, **102**, 2207−2213.

Alvero, R., Alba, M.D., Castro, M.A., and Trillo, J.M. (1994) Reversible migration of lithium in montmorillonite. *Journal of Physical Chemistry*, **98**, 7848−7853.

Bain, D.C. and Smith, B.F.L. (1987) Chemical analysis. Pp. 248−274 in: *A Handbook of Determinative Methods in Clay Mineralogy* (M.J. Wilson, editor). Blackie, Glasgow and London.

Besson, G. and Drits, V.A. (1997a) Refined relationships between chemical composition of dioctahedral fine-dispersed mica minerals and their infrared spectra in the OH stretching region. Part I: Identification of the stretching bands. *Clays and Clay Minerals*, **45**, 158−169.

Besson, G. and Drits, V.A. (1997b) Refined relationships between chemical composition of dioctahedral fine-dispersed mica minerals and their infrared spectra in the OH stretching region. Part II: The main factors affecting OH vibration and quantitative analysis. *Clays and Clay Minerals*, **45**, 170−183.

Bishop, J., Pieters, C.M., and Edwards, J.O. (1994) Infrared spectroscopic analyses on the nature of water in montmorillonite. *Clays and Clay Minerals*, **42**, 702−716.

Bishop, J., Madejová, J., Komadel, P., and Fröschl, H. (2002) The influence of structural Fe, Al and Mg on the infrared OH bands in spectra of dioctahedral smectites. *Clay Minerals*, **37**, 607−616.

Brigatti, M.F., Galán, E., and Theng, B.K.G. (2006) Structures and mineralogy of clay minerals. Pp. 19−86 in: *Handbook of Clay*

Science (F. Bergaya, G. Lagaly and B.K.G. Theng, editors). Developments in Clay Science, **1**, Elsevier, Amsterdam.

Brindley, G.W. and Ertem, G. (1971) Preparation and solvation properties of some variable charge montmorillonites. *Clays and Clay Minerals*, **19**, 399–404.

Bujdák, J., Janek, M., Madejová, J., and Komadel, P. (2001) Methylene blue interactions with reduced charge smectites. *Clays and Clay Minerals*, **49**, 244–254.

Calvet, R. and Prost, R. (1971) Cation migration into empty octahedral sites and surface properties of clays. *Clays and Clay Minerals*, **19**, 175–186.

Christidis, G.E. (2006) Genesis and compositional heterogeneity of smectites. Part III: Alteration of basic pyroclastic rocks – A case study from the Troodos Ophiolite Complex, Cyprus. *American Mineralogist*, **91**, 685–701.

Christidis, G.E. and Eberl, D.D. (2003) Determination of layer charge characteristics of smectites. *Clays and Clay Minerals*, **51**, 644–655.

Christidis, G.E., Blum, A.E., and Eberl, D.D. (2006) Influence of layer charge and charge distribution of smectites on the flow behaviour and swelling of bentonites. *Applied Clay Science*, **34**, 125–138.

Chryssikos, G.D., Gionis, V., Kacandes, G.H., Stathopoulou, E.T., Suárez, M., García-Romero, E., and Sánchez del Río, M. (2009) Octahedral cation distribution in palygorskite. *American Mineralogist*, **94**, 200–203.

Clark, R.N., King, T.V.V., Klejwa, M., Swayze, G.A., and Vergo, N. (1990) High spectral resolution reflectance spectroscopy of minerals. *Journal of Geophysical Research*, **95**, 12653–12680.

Drits, V.A. and Zviagina, B.B. (2009) *Trans*-vacant and *cis*-vacant 2:1 layer silicates: Structural features, identification, and occurrence. *Clays and Clay Minerals*, **57**, 405–415.

Drits, V.A., Besson, G., and Muller, F. (1995) An improved model for structural transformations of heat-treated aluminous dioctahedral 2:1 layer silicates. *Clays and Clay Minerals*, **43**, 718–731.

Farmer, V.C. (1974) The layer silicates. Pp. 331–363 in: *The Infrared Spectra of Minerals* (V.C. Farmer, editor). Monograph **4**, Mineralogical Society, London.

Gates, W.P. (2005) Infrared spectroscopy and the chemistry of dioctahedral smectites. Pp. 125–168 in: *The Application of Vibrational Spectroscopy to Clay Minerals and Layered Double Hydroxides* (J.T. Kloprogge, editor). CMS Workshop Lectures **13**, The Clay Minerals Society, Aurora, Colorado, USA.

Gates, W.P., Komadel, P., Madejová, J., Bujdák, J., Stucki, J.W., and Kirkpatrick, R.J. (2000) Electronic and structural properties of reduced-charge montmorillonites. *Applied Clay Science*, **16**, 257–271.

Gates, W.P., Slade, P.G., Manceau, A., and Lanson, B. (2002) Site occupancies by iron in nontronites, *Clays and Clay Minerals*, **50**, 223–239.

Gionis, V., Kacandes, G.H., Kastritis, I.D., and Chryssikos, G.D. (2006) On the structure of palygorskite by mid- and near-infrared spectroscopy. *American Mineralogist*, **91**, 1125–1133.

Gionis, V., Kacandes, G.H., Kastritis, I.D., and Chryssikos, G.D. (2007) Combined near-infrared and X-ray diffraction investigation of the octahedral sheet composition of palygorskite. *Clays and Clay Minerals*, **55**, 543–553.

Guggenheim, S. and Koster van Groos, A.F. (2001) Baseline studies of the Clay Minerals Society Source clays: Thermal Analysis. *Clays and Clay Minerals* **49**, 433–443.

Guisseau, D., Patrier Mas, P., Beaufort, D., Girard, J.-P., Inoue, A., Sanjuan, B., Petit, S., Arnaud Lens, A., and Genter, A. (2007) Significance of the depth-related transition montmorillonite-beidellite in the Bouillante geothermal field (Guadeloupe, Lesser Antilles). *American Mineralogist*, **92**, 1800–1813

Greene-Kelly, R. (1953) The identification of montmorillonoids in clays. *Journal of Soil Science*, **4**, 233–237.

Güven, N. (1992) Rheological aspects of aqueous smectite suspensions. Pp. 81–125 in: *Clay–Water Interface and its Rheological Implications* (N. Güven and R.M. Pollastro, editors). CMS Workshop Lectures **4**, The Clay Minerals Society, Bloomington, Indiana, USA.

Hofmann, U. and Klemen, R. (1950) Verlust der Austauschfahigkeit von Lithiumionen an Bentonit durch Erhitzung. *Zeitschrift für Anorganische und Allgemeine Chemie*, **262**, 95–99.

Hrobáriková, J., Madejová, J., and Komadel, P. (2001) Effect of heating temperature on Li fixation, layer charge and properties of fine fractions of bentonites. *Journal of Materials Chemistry*, **11**, 1452–1457.

Jaynes, W.F. and Bigham, J.M. (1987) Charge reduction, octahedral charge, and lithium retention in heated, Li-saturated smectites. *Clays and Clay Minerals*, **35**, 440–448.

Johnston, C.T. and Premachandra, G.S. (2001) Polarized ATR-FTIR study of smectite in aqueous suspension. *Langmuir*, **17**, 3712–3718.

Karakassides, M.A., Petridis D., and Gournis, D. (1997) Infrared Reflectance Study of Thermally Treated Li- and Cs-Montmorillonites. *Clays and Clay Minerals*, **45**, 649–658.

Karakassides, M.A., Madejová, J., Arvaiová, B., Bourlinos, A., Petridis, D., and Komadel, P. (1999) Location of Li(I), Cu(II), and Cd(II) in heated montmorillonite: Evidence from specular reflectance infrared and electron spin resonance spectroscopies. *Journal of Materials Chemistry*, **9**, 1553–1558.

Kloprogge, J.T., Ruan, H., and Frost, R.L. (2000) Near-infrared spectroscopic study of synthetic and natural pyrophyllite. *Neues Jahrbuch für Mineralogie, Monatshefte*, **2000**, 337–347.

Komadel, P. (2003) Chemically modified smectites. *Clay Minerals*, **38**, 127–138.

Komadel, P., Bujdák, J., Madejová, J., Šucha, V., and Elsass, F. (1996) Effect of non-swelling layers on the dissolution of reduced-charge montmorillonite in hydrochloric acid. *Clay Minerals*, **31**, 333–345.

Koster van Groos, A.F. and Guggenheim, S. (1987) Dehydration of a Ca-and a Mg-exchanged montmorillonite (SWy-1) at elevated pressures. *American Mineralogist*, **72**, 292–298.

Laird, D.A. (1999) Layer charge influences on the hydration of expandable 2:1 phyllosilicates. *Clays and Clay Minerals*, **47**, 630–636.

Laird, D.A. (2006) Influence of layer charge on swelling of smectites. *Applied Clay Science*, **34**, 74–87.

Laird, D.A. and Fleming, P. (2008) Analysis of layer charge, cation and anion exchange capacities, and synthesis of reduced charge clays. In: *Methods of Soil Analysis. Part 5. Mineralogical Methods* (A. Ulery and R. Drees, editors). SSSA Book Series No 5. Madison, Wisconsin.

Laird, D.A., Barriuso, E., Dowdy, R.H., and Koskinen, W.C. (1992) Adsorption of atrazine on smectites. *Soil Science Society of America Journal*, **56**, 62–67.

Lantenois, S., Beny, J.-M., Muller, F., and Champallier, R. (2007) Integration of Fe in natural and synthetic Al-pyrophyllites: an infrared spectroscopic study. *Clay Minerals*, **42**, 129–141.

Lim, C.H. and Jackson, M.L. (1986) Expandable phyllosilicate reactions with lithium on heating. *Clays and Clay Minerals*, **34**, 346–352.

Luca, V., Cardile, C.M., and Meinhold, R.H. (1989) High resolution multinuclear NMR study of cation migration in montmorillonite. *Clay Minerals*, **24**, 115–119.

Madejová, J. (2005) Studies of reduced-charge smectites by near infrared spectroscopy. Pp. 169–202 in: *The Application*

of Vibrational Spectroscopy to Clay Minerals and Layered Double Hydroxides (J.T. Kloprogge, editor). CMS Workshop Lectures **13**, The Clay Minerals Society, Aurora, Colorado, USA.

Madejová, J. and Komadel, P. (2005) Information available from infrared spectra of the fine fractions of bentonites. Pp. 65–98 in: *The Application of Vibrational Spectroscopy to Clay Minerals and Layered Double Hydroxides* (J.T. Kloprogge, editor). CMS Workshop Lectures **13**, The Clay Minerals Society, Aurora, Colorado, USA.

Madejová, J., Komadel, P., and Čičel, B. (1994) Infrared study of octahedral site populations in smectites. *Clay Minerals*, **29**, 319–326.

Madejová, J., Bujdák, J., Gates, W.P., and Komadel, P. (1996) Preparation and infrared spectroscopic characterization of reduced-charge montmorillonite with various Li contents. *Clay Minerals*, **31**, 233–241.

Madejová, J., Bujdák, J., Petit, S., and Komadel, P. (2000a) Effects of chemical composition and temperature of heating on the infrared spectra of Li-saturated dioctahedral smectites (I) Mid-infrared region. *Clay Minerals*, **35**, 739–751.

Madejová, J., Bujdák, J., Petit, S., and Komadel, P. (2000b) Effects of chemical composition and temperature of heating on the infrared spectra of Li-saturated dioctahedral smectites (II) Near-infrared region. *Clay Minerals*, **35**, 753–761.

Madejová, J., Pálková, H., and Komadel, P. (2006) Behaviour of Li^+ and Cu^{2+} in heated montmorillonite: Evidence from far-, mid-, and near-IR regions. *Vibrational Spectroscopy*, **40**, 80–88.

Maes, A. and Cremers, A. (1977) Charge density effects in ion exchange. Part 1. Heterovalent exchange equilibria. *Journal of the Chemical Society Faraday Transactions*, **73**, 1807–1814.

Maes, A. and Cremers, A. (1978) Charge density effects in ion exchange. Part 2. Homovalent exchange equilibria. *Journal of the Chemical Society Faraday Transactions*, **74**, 1234–1241.

Maes, A., Stul, M.S., and Cremers, A. (1979) Layer charge-cation-exchange capacity relationships in montmorillonite. *Clay and Clay Minerals*, **27**, 387–392.

Muller, F., Besson, G., Manceau, A., and Drits, V.A. (1997) Distribution of isomorphous cations within octahedral sheets in montmorillonite from Camp-Berteau. *Physics and Chemistry of Minerals*, **24**, 159–166.

Odom, I.E. (1984) Smectite clay minerals: properties and uses. *Philosophical Transactions of the Royal Society of London*, **A311**, 391–409.

Petit, S. (2005) Crystal-chemistry of talcs: A NIR and MIR spectroscopic approach. Pp. 41–64 in: *The Application of Vibrational Spectroscopy to Clay Minerals and Layered Double Hydroxides* (J.T. Kloprogge, editor). CMS Workshop Lectures **13**, The Clay Minerals Society, Aurora, Colorado, USA.

Petit, S., Caillaud, J., Righi, D., Madejová, J., Elsass, F., and Köster, H.M. (2002) Characterization and crystal chemistry of an Fe-rich montmorillonite from Ölberg, Germany. *Clay Minerals*, **37**, 283–297.

Petit, S., Decarreau, A., Martin, F., and Buchet, R. (2004) Refined relationship between the position of the fundamental OH stretching and the first overtones for clays. *Physics and Chemistry of minerals*, **31**, 585–592.

Post J.L. and Noble, P.N. (1993) The near-infrared combination band frequencies of dioctahedral smectites, micas and illites. *Clays and Clay Minerals*, **41**, 639–644.

Russell, J.D. (1979) An infrared spectroscopic study of the interaction of nontronite and ferruginous montmorillonites with alkali metal hydroxides. *Clay Minerals*, **14**, 127–137.

Russell, J.D. and Fraser, A.R. (1994) Infrared methods. Pp. 11–67 in: *Clay Mineralogy: Spectroscopic and Chemical Determinative Methods* (M.J. Wilson, editor). Chapman & Hall, London.

Sainz-Diaz, C.I., Hernández-Laguna, A., and Dove, M.T. (2001) Theoretical modelling of *cis*-vacant and *trans*-vacant configurations in the octahedral sheet of illites and smectites. *Physics and Chemistry of Minerals*, **28**, 322–331.

Sato, T., Watanabe, T., and Otsuka, R. (1992) Effects of layer charge, charge location and energy change on expansion properties of dioctahedral smectites. *Clays and Clay Minerals*, **40**, 103–113.

Shainberg, I., Alperovitch, N.I., and Keren, R. (1987) Charge density and Na–K–Ca exchange on smectites. *Clays and Clay Minerals*, **35**, 68–73.

Slade, P.G., Quirk, J.R., and Norrish, K. (1991) Crystalline swelling of smectite samples in concentrated NaCl solutions in relation to layer charge. *Clays and Clay Minerals*, **39**, 234–238.

Sposito, G., Prost, R., and Gaultier, J.P. (1983) Infrared spectroscopic study of adsorbed water on reduced-charge Na/Li-montmorillonites. *Clays and Clay Minerals*, **31**, 9–16.

Srasra, E., Bergaya, F., and Fripiat, J.J. (1994) Infrared spectroscopy study of tetrahedral and octahedral substitutions in an interstratified illite-smectite clay. *Clays and Clay Minerals*, **42**, 237–241.

Stackhouse, S. and Coveney, P.V. (2002) Study of thermally treated lithium montmorillonite by *ab initio* methods. *Journal of Physical Chemistry*, **106**, 12470–12477.

Tettenhorst, R. (1962) Cation migration in montmorillonites. *American Mineralogist*, **47**, 769–773.

Theng, B.K.G., Hayashi, S., Soma, M., and Seyama, H. (1997) Nuclear magnetic resonance and X-ray photoelectron spectroscopic investigation of lithium migration in montmorillonite. *Clays and Clay Minerals*, **45**, 718–723.

Tombacz, E. and Szekeres, M. (2004) Colloidal behaviour of aqueous montmorillonite suspensions: the specific role of pH in the presence of indifferent electrolytes. *Applied Clay Science*, **27**, 75–94.

Tsipurski, S.I. and Drits, V.A. (1984) The distribution of octahedral cations in the 2:1 layers of dioctahedral smectites studied by oblique-texture electron diffraction. *Clay Minerals*, **19**, 177–193.

VanScoyoc, G.E., Serna, C.J., and Ahlrichs, J.L. (1979) Structural changes in palygorskite during dehydration and dehydroxylation. *American Mineralogist*, **64**, 215–223.

Wolters, F. and Emmerich, K. (2007) Thermal reactions of smectites – Relation of dehydroxylation temperature to octahedral structure. *Thermochimica Acta*, **462**, 80–88.

Wang, L., Zhang, M., Redfern, S.A.T., and Zhang, Z. (2002) Dehydroxylation and transformations of the 2:1 phyllosilicate pyrophyllite at elevated temperatures: An infrared spectroscopic study. *Clays and Clay Minerals*, **50**, 272–283.

Zviagina, B.B., McCarty, D.K., Środoń, J., and Drits, V.A. (2004) Interpretation of infrared spectra of dioctahedral smectites in the region of OH-stretching vibrations. *Clays and Clay Minerals*, **52**, 399–410.

(*Received 13 August 2012; revised 23 February 2013; Ms. 700, AE: S. Petit*)

Clays and Clay Minerals, Vol. 61, No. 2, 98–106, 2013.

IDENTIFICATION AND QUANTIFICATION OF THE INTERACTION MECHANISMS BETWEEN THE CATIONIC SURFACTANT HDTMA-Br AND MONTMORILLONITE

PABLO M. NARANJO[1,*], EDGARDO L. SHAM[1,2], ENRIQUE RODRÍGUEZ CASTELLÓN[3], ROSA M. TORRES SÁNCHEZ[4], AND ELSA M. FARFÁN TORRES[1,5]

[1] INIQUI (Instituto de Investigaciones para la Industria Química) – Av. Bolivia 5150 (A4408FVY) Salta, Argentina
[2] Fac. Ingeniería, Universidad Nacional de Salta, Av. Bolivia 5150 (A4408FVY) Salta, Argentina
[3] Fac. Ciencias, Campus de Teatinos, Universidad de Málaga, Boulevar Louis Pasteur 29010, Málaga, Spain
[4] CETMIC (Centro de Tecnología en Minerales y Cerámica) – Camino Centenario y 506 CC (49) (B1897ZCA) M. B. Gonnet, Argentina
[5] Fac. Cs. Exactas, Universidad Nacional de Salta, Av. Bolivia 5150 (A4408FVY) Salta, Argentina

Abstract—Several detailed studies have been done on the characterization of organoclays and the type of structures developed when they interact with alkylammonium molecules. Few published contributions exist, however, on the distribution of surfactant within the organoclays and the mechanism by which they are intercalated. Also, although X-ray photoelectron spectroscopy (XPS) is a suitable technique for the study of the surface characteristics of organoclays, very few such XPS studies have been carried out. With the aim of contributing to a better understanding of the intercalation process, a series of organoclays was synthesized using a montmorillonite and the cationic surfactant hexadecyltrimethylammonium bromide (HDTMABr), with an increasing surfactant load of between 0.2 and 4.0 times the cation exchange capacity of the starting clay. By means of XPS, zeta potential, and thermal analysis techniques, distinguishing the strongly interacting fraction from the weakly interacting fraction of the adsorbed surfactant molecules was possible. Adsorption isotherms of each of these processes were constructed and then adjusted using the Langmuir and Dubinin-Radusquevich adsorption models. Three types of interaction between the surfactant and the clay were identified and described qualitatively and quantitatively. Two of these interactions, strong and weak, involved the hexadecyltrimethylammonium cation ($HDTMA^+$). The third was a weak interaction involving the ion pair $HDTMA^+Br^-$. The results of this study may be useful for the comprehensive design of organoclays with specific physicochemical properties according to the application for which they are destined.

Key Words—Alkylammonium molecules, Cationic Surfactant HDTMA-Br, Montmorillonite.

INTRODUCTION

Smectites are layered aluminosilicates generally arranged in groups of different numbers of layers. The layers have an excess negative charge in their structure. Cations which compensate these charges are located in the interlayer space, are referred to as 'interlaminar cations', and can be exchanged either for organic or inorganic cations.

Organically modified clays, also known as organoclays or nanoclays, can be used in a number of ways, *e.g.* in catalytic processes, as rheological control agents in paintings and lubricants, to reinforce the matrix of polymers and plastics, as adsorbents for effluent treatments, in oil spills, and as a slow-release active matrix, *etc*. (Azejjel *et al*., 2009; Carrado, 2000; de Paiva *et al*., 2008).

The use of thermal analysis techniques for the study of montmorillonitic clays is well established. Thermoanalytical studies of organo-modified clays have demonstrated the applicability of differential thermal analysis-thermogravimetry (DTA-TG) and differential scanning calorimetry (DSC) for differentiating between adsorbed and free organic matter, and also between ionic and molecular adsorption (Xi *et al.*, 2005; He *et al*., 2005, 2006; Yariv *et al*., 2012).

X-ray photoelectron spectroscopy is a powerful technique for studying the surface characteristics of various materials, including clay minerals and related products. Unfortunately, to date, very few XPS studies of organoclays have been published, even though XPS provides valuable information about the distribution of surfactants within organoclays (He *et al*., 2007).

Some of the studies published have described more than one type of interaction between the surfactants and the surface. When dealing with cationic surfactants, cationic exchange is reported as the most important mechanism of adsorption (Bilgiç, 2005). This type of adsorption is related to an average energy of adsorption of between 9 and 16 kJ/mol (Donat *et al.*, 2005). Another reported mechanism of adsorption is interaction through Van der Waals forces. This interaction is weaker than cation exchange adsorption, presenting average adsorption energies in the range 1–8 kJ/mol. Surfactant molecules can be adsorbed by the latter mechanism

* E-mail address of corresponding author:
pnaranjo@unsa.edu.ar
DOI: 10.1346/CCMN.2013.0610208

either as cations or as ion pairs with the respective counterion (Tahani *et al.*, 1999).

To the authors' knowledge no work has been reported that quantifies the fractions of surfactant adsorbed by the different types of interaction.

The aim of the present study was to assess, qualitatively and quantitatively, different mechanisms of interaction between a HDTMA-Br type cationic surfactant and the surface of a montmorillonite-type clay mineral, and to propose the mechanisms involved in these processes.

MATERIALS AND METHODS

Materials

Natural Castiglione clay, which consists mainly of montmorillonite and has a cation exchange capacity (CEC) of 83.7 mmol/100 g, together with hexadecyltrimethylammonium bromide (HDTMA-Br), provided by Merck, were used as starting materials. All solutions were prepared using deionized water (DI-H_2O)

Preparation of organoclays

Organoclays with surfactant loading (SL) of between 0.2 and 4.0 times the CEC were synthesized. The synthesis was carried out in batch, putting 50 mL of a suspension of ~5% w/v of the starting clay in contact with different volumes of 5×10^{-3} M solution of HDTMA-Br, in a final volume of 500 mL. This suspension was kept under shaking for 2 h at room temperature. The solid fraction (organoclay) was separated by centrifugation and washed with DI-H_2O until the total elimination of Br^-. Organoclays were dried at 60ºC, milled in an agate mortar and stored in a desiccator for further characterization, designating each of them as Bent followed by the SL (Bent-0.4, Bent-0.8, *etc*.).

Characterization of the samples

The intercalation process was analyzed by measuring the concentration of the Br^- remaining in the solution after the intercalation, which was achieved by precipitation titration with a standard solution of 0.01 M $AgNO_3$ and 5% w/v K_2CrO_4 solution as indicator. At the same time, the amount of Na^+ exchanged in the solution was quantified by atomic absorption spectrometry (AAS) with flame ionization.

Thermogravimetric analyses were performed using a Rigaku TAS 1100 instrument at temperatures ranging from room temperature to 1200ºC, at a heating rate of 20ºC/min using 20 mg of sample, in a static air atmosphere.

The starting clay mineral, solid surfactant, and organoclays with SL of 0.4, 0.8, 2.0, and 4.0 were analyzed by XPS, using an ESCA 5700 instrument from 'Physical Electronic' (University of Málaga, Spain), with MgKα and AlKα radiation (hν = 1253.6 and 1486.6 eV, respectively), using a hemispheric electron analyzer. Binding energies (BE) were determined with an accuracy of ±0.1 eV. Charge referencing was measured against adventitious carbon (C1s = 284.8 eV). The residual pressure in the analysis chamber was maintained below 10^{-7} Pa during all measurements.

Zeta potential (ζ) measurements of the starting clay and the organoclay Bent-0.8 were performed in a Z-Meter 3.0 instrument from ZETA-METER, Inc. (National University of Salta, Argentina), using suspensions of samples of 0.005% w/v in 0.01 M $NaNO_3$.

Adsorption isotherms were adjusted using the Langmuir equation.

$$q_e = q_{max} K_L C_e / (1 + K_L C_e) \quad (1)$$

where q_e is the amount of solute adsorbed per unit of solid mass (mol/g) for an equilibrium concentration C_e (mol/L); q_{max} is the maximum amount adsorbed in the surface (mol/g), and K_L is the Langmuir constant (L/mol). From the Langmuir constant, a parameter, r, referred to as a "dimensionless equilibrium parameter" can be calculated (Mahramanlioglu *et al.*, 2002). A value of $r < 1$ indicates favorable adsorption, while $r > 1$ indicates an unfavorable adsorption. This parameter was calculated as follows:

$$r = 1/(1 + K_L C_0) \quad (2)$$

where C_0 is the value of the initial concentration of one of the isotherm points.

These data were also adjusted using the Dubinin-Raduskevich equation:

$$q_e = q_{max} \exp(-\beta \varepsilon^2) \quad (3)$$

where ε is the Polanyi potential:

$$\varepsilon = RT \ln(1 - 1/C_e) \quad (4)$$

q_e, q_{max}, and C_e have the same meanings as in the previous equation and β (mol^2/J^2) is a constant related to the average adsorption free energy (E, J/mol):

$$E = -(2\beta)^{(-1/2)} \quad (5)$$

This last isotherm is more general than the Langmuir isotherm because it assumes neither homogeneity of surface adsorption sites nor constancy of adsorption potential (Ackay *et al.*, 2006). The magnitude of adsorption energy can give an indication of the type of adsorption which occurred.

RESULTS AND DISCUSSION

Previous results showed that surfactant is adsorbed by the Bent clay in at least two kinds of different sites indicated by the different thermal stabilities of surfactant molecules.

From characterization results and molecular modeling calculations, a mechanism of adsorption was proposed. Surfactant molecules were initially adsorbed in sites located in the interlayer space of the clay through

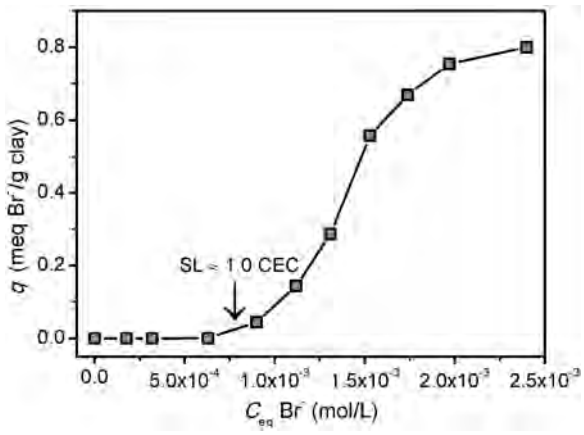

Figure 1. Sorption isotherms of bromide in montmorillonite.

cation exchange. In these kinds of sites, the adsorption was carried out until the interlayer space was saturated. Depending on the surfactant loading anchored in the intercalation process, different kinds of organization of the interlayer were obtained, varying from monolayer in Bent-0.4 to bilayer/pseudo-trilayer in Bent-3.0.

Further adsorption of surfactant occurred in the mesopores generated by tactoids ordered in a 'house-of-cards' type structure. This process left surfactant molecules relatively free, outside the interlayer space.

Quantification of Br^- and Na^+ in supernatant solution of adsorption isotherms

The Br^- anion is present during the adsorption process as a counterion of the cationic surfactant. Chemical analysis, performed after alkylammonium adsorption, showed that in the case of organoclays with SL up to ~1.0 CEC, all the initial Br^- stayed in the solution. For SL values >1.0 CEC, a fraction of Br^- was adsorbed in the solid.

The sorption isotherm of Br^- (Figure 1) coincided with the S-type isotherm described by Giles *et al.* (1974), indicating that it is a system with low affinity of adsorbate for adsorbent. This is concurrent with the existing electrostatic repulsion between the structural negative charges of the layer and the bromide anion. When the SL is >1.0 CEC (Figure 1), the negative charge is compensated by an excess of cationic surfactant, and the process of Br^- sorption begins. A similar phenomenon was observed by Su *et al.* (2012) for NO_3^- adsorption in reversed-charge smectites.

The amount of Na^+ released from the clay, as a result of cationic exchange with the surfactant, was also determined. Results show that the amount of Na^+ released increased with SL up to 1.0 CEC, and remained constant for higher SL values.

Thermogravimetric analysis

Up to ~120ºC, the starting clay experienced a mass loss corresponding to the elimination of physisorbed water, and then a second mass loss corresponding to the dehydroxylation of layers between 500 and 700ºC (Figure 2a). Both thermal events are associated with several endothermic peaks detected in the DTA thermogram (Figure 2b). In organoclay thermograms, a mass loss related to the elimination of physisorbed water was observed between room temperature and ~120ºC (Figure 2a). Another mass loss, associated with a series of exothermic events, was observed between 180 and 700ºC, corresponding both to surfactant combustion phenomena and to the dehydroxylation of layers.

The total percentage of organic compound adsorbed by the clay as function of the SL was determined from thermograms. According to previous results, distinguishing the amount of surfactant adsorbed through each of the two mechanisms, based on the adsorption energies, is possible. The fraction with lower sorption energy

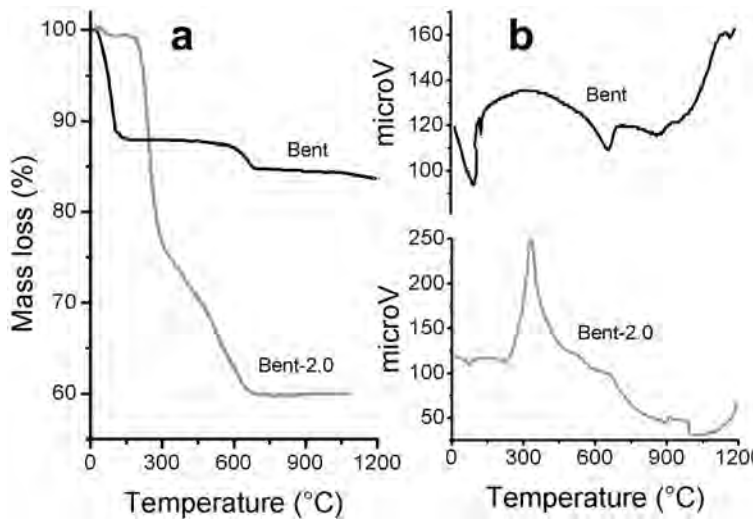

Figure 2. TG (a) and ATD (b) thermograms of Bent (black) and Bent-2.0 (gray).

(mechanism 1) is removed between 180 and 350ºC, and the fraction with greater sorption energy (mechanism 2), between 350 and 800ºC (Figure 3).

For mechanism 1, the adsorption isotherm slope decreased as the equilibrium concentration of the surfactant increased. It was a C-type isotherm in the Giles classification, indicating that the affinity between the solute and the solid was weak, consistent with the low temperatures at which this fraction of surfactant was eliminated (between 180 and 350ºC). For mechanism 2, the isotherm slope increased vertically up to ~0.7 mmol surfactant/g clay and then remained almost constant. This was an H-type isotherm in the Giles classification, with high affinity between the solute and the adsorbent and with high adsorption energy, consistent with the higher temperature of elimination of this fraction of surfactant (between 350 and 800ºC). The total adsorption isotherm is produced from the addition of these two isotherms.

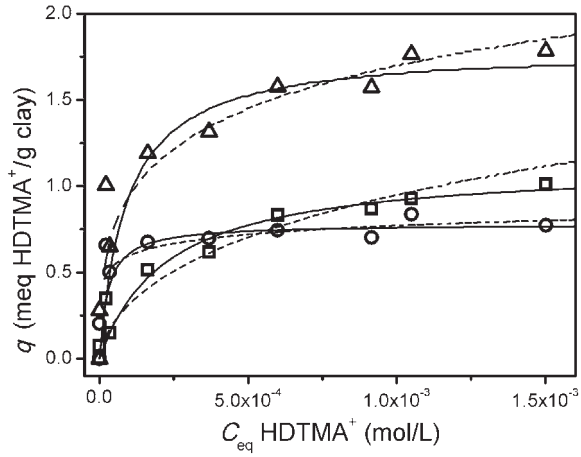

Figure 3. Adsorption isotherms of surfactant in clay by mechanism 1 (○), mechanism 2 (□), and total adsorption (△). Experimental data were adjusted by Langmuir (solid line) and Dubinin-Raduskevich (dash line) models.

Adjustment of adsorption isotherms

Data from adsorption isotherms of the surfactant adsorbed by each mechanism type and the total adsorbed were adjusted using the Langmuir and Dubinin-Raduskevich equations (Figure 3). The results obtained are summarized in Table 1.

Langmuir adsorption model. From the Langmuir adsorption model, values of q_{max} for the total adsorbed amount ($q_{max,\ Total}$) and for the amount adsorbed in weak sites through mechanism 1 ($q_{max,\ 1}$) were calculated. For strong sites, a poor adjustment of the Langmuir equation was obtained ($R^2 = 0.4930$). This is related to the kind of adsorption process developed for the interactions with strong sites. Therefore, the value of q_{max} for mechanism 2 ($q_{max,2}$) was obtained from the difference: $q_{max,2} = q_{max,Total} - q_{max,1}$. A dimensionless equilibrium parameter was calculated using the concentration value of the first point of the adsorption isotherm (1.6×10^{-4} M). A value of $r < 1$ was found in each case, indicating that both adsorption mechanisms were favored.

Dubinin-Raduskevich adsorption model. From the Dubinin-Raduskevich adsorption model, the values of average adsorption energy for the total adsorption of surfactant (E_{Total} = 12.8 kJ/mol), the surfactant adsorbed through mechanism 1 (weak adsorption, E_1 = 9.3 kJ/mol), and the surfactant adsorbed through mechanism 2 (strong adsorption, E_2 = 19.3 kJ/mol) were obtained.

An average adsorption energy of between 1 and 8 kJ/mol indicated physisorption, and between 9 and 16 kJ/mol, chemical adsorption (Donat *et al*., 2005). In the present study, the adsorption on strong sites was a process involving a slightly higher adsorption energy than is generally the case in processes of cationic exchange, so it may be a specific adsorption type, probably resulting in the formation of an inner sphere complex between the surfactant molecule and the clay mineral layer. Besides, the adsorption on weak sites practically coincided with the physisorption energy, meaning that mechanism 1 is the result of the adsorption, through Van der Waals forces (VdW), of surfactant molecules previously adsorbed in the clay by the strong mechanism.

XPS

Sodium and bromine. The results obtained showed the presence of Na in the starting clay, as characterized by the band at 1072.9 eV. In organoclays, the intensity of

Table 1. Langmuir and Dubinin-Raduskevich parameters for mechanism 1, mechanism 2, and the total adsorption.

Mechanism	Dubinin-Raduskevich isotherm			Langmuir isotherm				
	E_{ads} (kJ/mol)	R^2	N	q_m (mmol/g)	K_L (l/mol)	R^2	r	N
2 (strong)	19.3	0.8765	7	0.67*	–	–	–	–
1 (weak)	9.3	0.9642	7	1.13	4.39E+03	0.9970	0.59	7
Total	12.8	0.9744	7	1.80	1.10E+04	0.8695	0.36	7

* Value obtained by difference between $q_{max,\ Total}$ and $q_{max,\ 1}$.

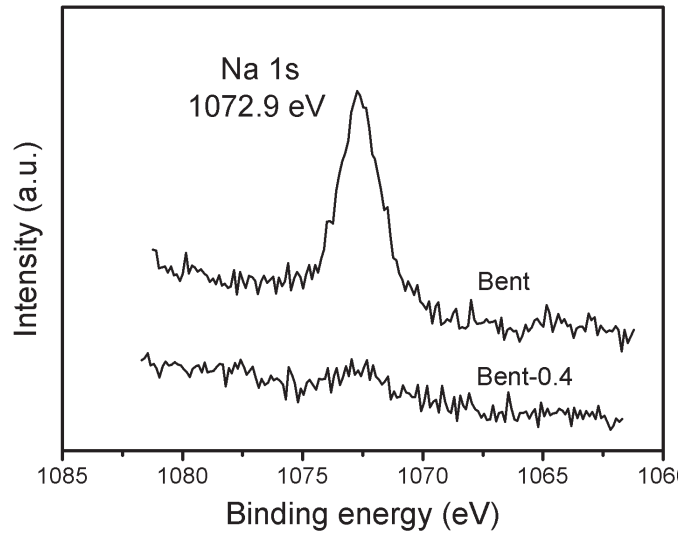

Figure 4. XPS spectra for the samples Bent and Bent-0.4 in the range 1060−1085 eV.

the band corresponding to Na decreased as SL increased. For a SL of 0.8 CEC, only traces of Na were detected, and Na was absent from organoclays with greater SL values as well as for pure surfactant (Figure 4).

The band corresponding to bromine in the XPS spectrum of HDTMA-Br was found at 67.0 eV. Its presence was detected in organoclays with SL values of 2.0 and 4.0 CEC, at 67.7 eV and 67.5 eV, respectively, but was absent from organoclays with lower SL values (Figure 5).

For a given element, binding energy (BE) increases when oxidation occurs, and decreases with reduction. The bromide anion adsorption starts when $HDTMA^+$ adsorption exceeds the CEC. In this situation, Br^- anions were surrounded by an excess of cations, which removed electron density. This decrease of electron density in the anion bromide is equivalent to 'oxidation,' coinciding with the observed increase in BE.

Nitrogen. Most nitrogen functions in which nitrogen is bound to carbon, like amine, amide, nitrile, urea, and nitrogen in aromatic rings, show N1s binding energies in the range 399−400 eV. Quaternary nitrogen shows greater binding energies in the range 401.5−402.5 eV, as expected from the localized positive charge (Briggs, 1998; Liu *et al.*, 2010).

HDTMA-Br presented a band corresponding to N1s at 402.1 eV, referred to as B1 in the present study. In organoclays, B1 shifted to values between 402.2 and

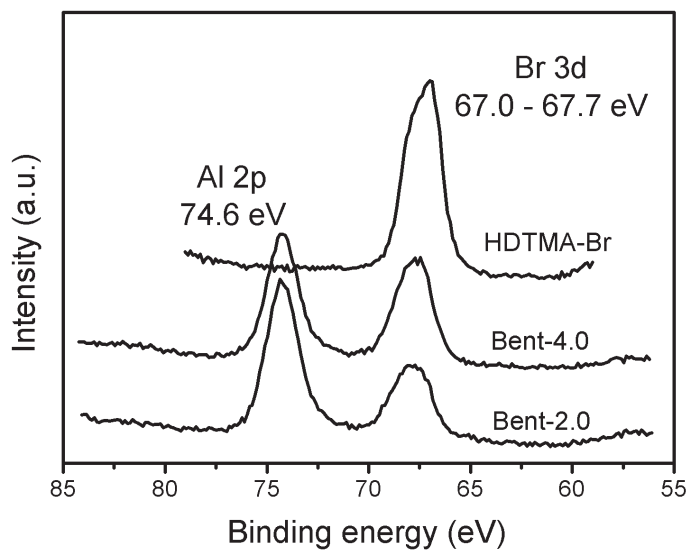

Figure 5. XPS spectra for the samples Bent-2.0, Bent-4.0, and for the pure surfactant in the range 55−85 eV.

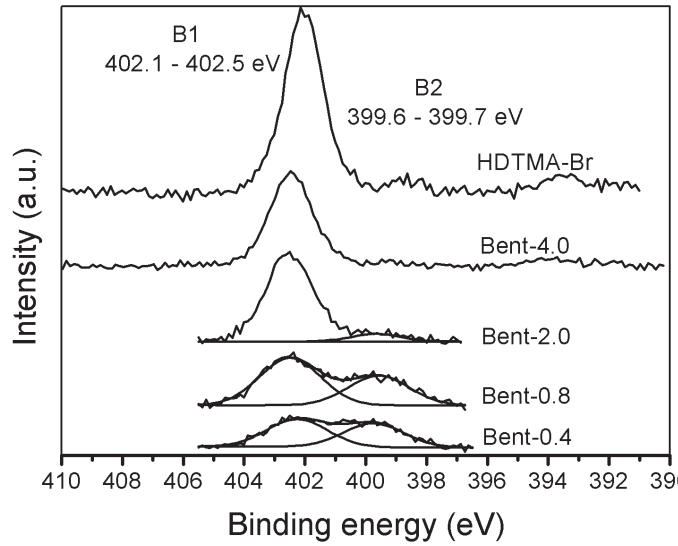

Figure 6. XPS spectra for the samples indicated in the range 390−410 eV.

402.5 eV. The XPS spectra of organoclays showed another band, referred to as 'B2' here, at values of between 399.6 and 399.7 eV (Figure 6).

The position of the B1 band coincides with the BE range of the quaternary nitrogen N1s band, so it was assigned to nitrogen atoms of the surfactant molecules adsorbed in the surface with low energy through Van der Waals forces, as was described for mechanism 1. On other hand, the position of the B2 band was assigned to nitrogen atoms adsorbed with high energy, and corresponds to surfactant molecules adsorbed through mechanism 2 (strong adsorption). The B2 band was not detected in the organoclay with the greatest SL value.

The decrease in binding energy of the B2 band indicated an increase of electron density in the nitrogen. This phenomenon occurs due to a charge transfer from the clay layers to the surfactant molecule (Seki and Yurdakoç, 2005).

In order to facilitate the study of these results and to analyze them together with data provided by thermogavimetric analysis, the following ratios were defined:

$$R_{i,\,(B1/(B1+B2))} = a_{i,\,B1}/(a_{i,\,B1} + a_{i,\,B2})$$
$$R_{i,\,(CE/(CE+VdW))} = q_{i,\,VdW}/(q_{i,\,(CE/(CE+VdW))} + q_{i,\,VdW})$$

where a_i is the area of the nitrogen XPS band (B1 or B2, as indicated) of the organoclay with SL = i and q_i is the amount of surfactant adsorbed per mass unit, as determined by TG, corresponding to adsorption by cationic exchange (CE) or by Van der Waals (VdW) interactions of the organoclay with SL = i.

Both ratios increased with SL (Figure 7). This indicates that the relative amount of molecules adsorbed through Van der Waals forces increased with SL. For small SL values, the TG results indicated that 20% of the molecules were adsorbed by Van der Waals interactions, whereas XPS results indicated that this percentage is 50%. For large SL values, the percentage of molecules adsorbed by weak forces increased to 60%, according to TG, whereas, according to XPS, 100% of the molecules were observed to be adsorbed by Van der Waals interactions, *i.e.* molecules adsorbed through CE were not detected. The TG provided data about all of the sample, whereas XPS analyzes the surface only up to a determined depth (~4 nm in this case). So, the fact that molecules adsorbed through CE were not detected by XPS analyses in organoclays with SL = 4.0 CEC confirms that weak adsorption is produced at the external surface of the layers. The presence of molecules fixed in the interlayer space through strong adsorption could not be detected from XPS spectra because of the

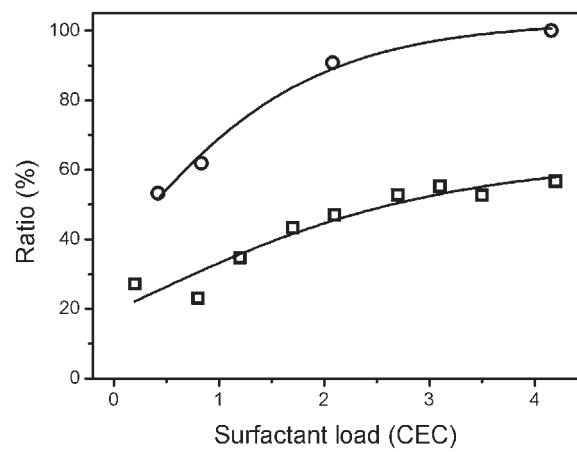

Figure 7. Percentage of surfactant adsorption by a weak mechanism with respect to total adsorption: data obtained from TG (□) and XPS (○) are compared.

limited depth of analysis in the conditions in which these studies were carried out.

Zeta potential

The zeta potential (ζ) of organoclay Bent-0.8 was less negative than the ζ of the starting clay throughout the pH range studied (Figure 8). In order to produce a variation in this potential, the adsorption of an ion with a charge opposite to that of the layer (in this case, a cation) must occur at a distance smaller than the thickness of the Stern layer (Jouniaux and Ishido, 2012). Inorganic cations are hydrophilic, adsorbed with their hydration spheres forming outer-sphere complexes outside of the Stern layer. Moreover, surfactant molecules are hydrophobic and are adsorbed in a specific way, forming inner sphere complexes with the negative charges of the layers, which produce an increase in the ζ.

Adsorption model

The processes that are possible as the SL value increases were deduced by analysing the data shown in Figure 9 and the scheme illustrated in Figure 10. Note that Figure 9 is not an adsorption isotherm, as the horizontal axis does not represent surfactant concentration at equilibrium. Figure 9 shows the variations of the quantity of surfactant and bromide adsorbed by the different mechanisms with respect to the amount of surfactant added initially.

When the SL value was small (Figure 10b), surfactant adsorption occurred with the release of Na^+ to supernatant solution, as was verified by chemical analysis and XPS results. The large adsorption energies determined from the adjustment of adsorption isotherms and the variations in bending energy indicate that the process carried out in this stage was not simply an exchange of cations. The zeta potential results suggest that it was a specific adsorption, involving the formation of an inner-sphere complex and the transfer of charge between the surfactant and the clay mineral. This process (strong adsorption) continued until it reached a value of SL = 1. Surfactant molecules adsorbed through this mechanism are referred to as '$HDTMA^+$(CE).'

Another adsorption mechanism may be proposed based on TG results, the adjustment of data given by the Dubinin-Raduskevich adsorption model, and the binding energy bands corresponding to nitrogen atoms in XPS studies, in which the surfactant in the solution interacts, through Van der Waals forces, with alkyl tails of previously adsorbed surfactant cations. This process (weak adsorption) was observed throughout the SL range studied. Surfactant molecules adsorbed through this mechanism were referred to as '$HDTMA^{total}$(VdW)'.

From the total amount of surfactant molecules adsorbed through Van der Waals forces, a fraction was present as cations, and another fraction formed ion pairs with bromide anions. For an SL value < the CEC (Figure 10a), the organoclay carried a net negative charge, keeping Br^- anions from getting close to it. Weak adsorption of ionic pairs, quantified by the decrease of bromide in supernatant solutions and corroborated by the presence of the peak corresponding to bromine in XPS spectra, started when SL > 1 and increased with SL in the studied range (Figure 10d). Surfactant molecules adsorbed through this mechanism were referred to as '$HDTMA^+Br^-$(VdW)'.

The interaction mechanisms between the surfactant and the clay are summarized in Table 2. The difference between $HDTMA^{total}$(VdW) and $HDTMA^+Br^-$(VdW) was the amount of surfactant adsorbed by VdW forces that did not form ion pairs. This type of adsorption was observed throughout the SL range studied, with a maximum at an intermediate value (SL ≈ 1.7 CEC) (Figure 9). Surfactant molecules adsorbed through this mechanism were referred to as '$HDTMA^+$(VdW)'.

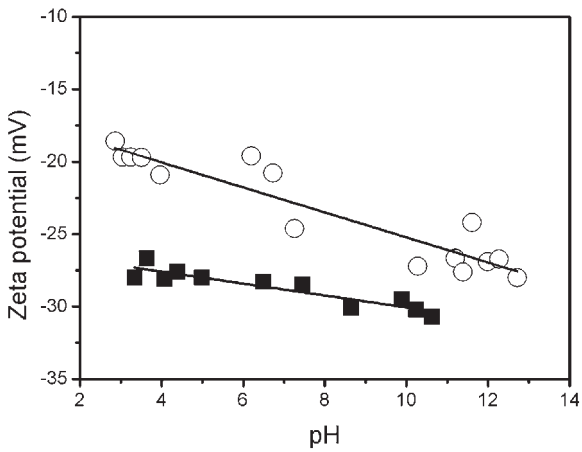

Figure 8. Zeta potential *vs*. pH. Comparison of the starting clay (■) with the organoclay Bent-0.4 (○).

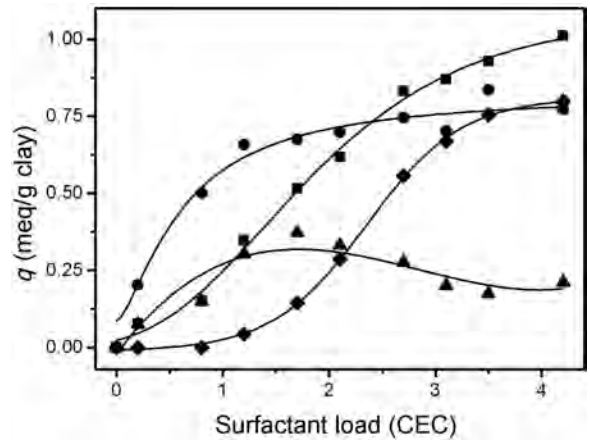

Figure 9. Different forms of surfactant adsorption: $HDTMA^+$(CE) (●), $HDTMA^{Total}$(VdW) (■), $HDTMA^+Br^-$(VdW) (▲), and $HDTMA^+$(VdW) (◆): Amounts adsorbed per mass of clay in relation to the amount of surfactant added initially.

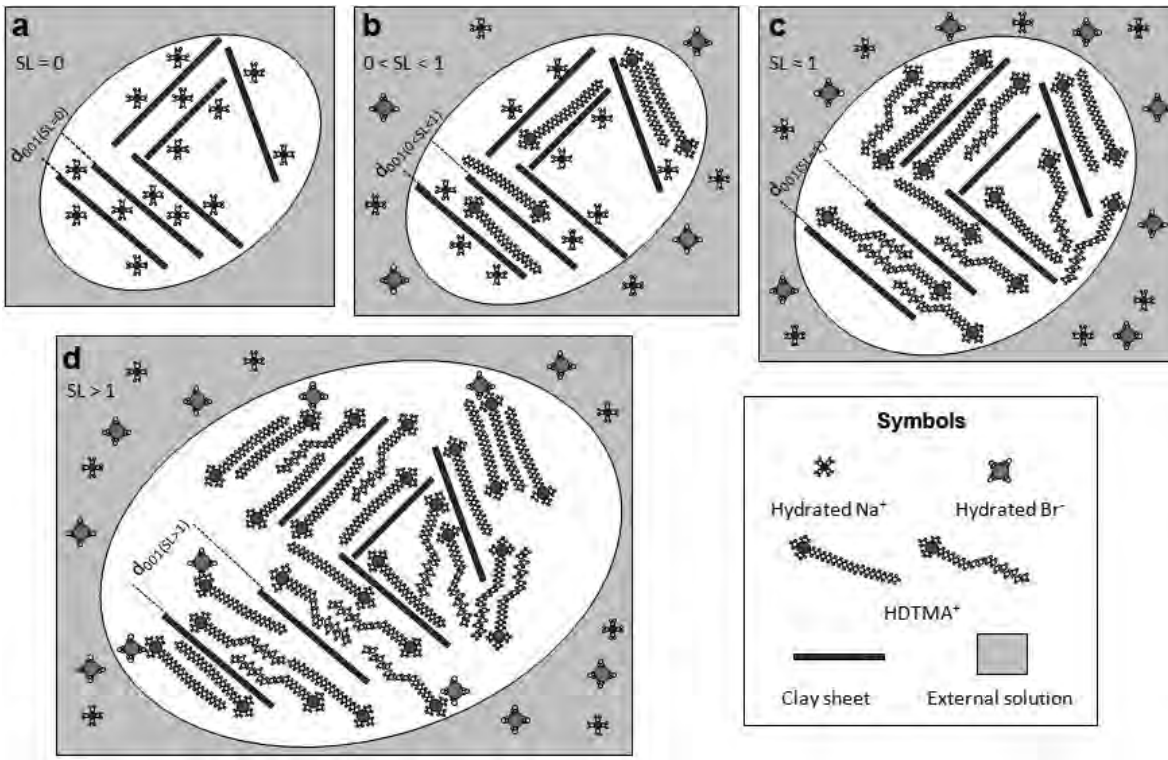

Figure 10. Schematic representation of the process of adsorption of surfactant on the surface of montmorillonite.

CONCLUSIONS

Organoclays containing different amounts of organic compounds were synthesized using $HDTMA^+Br^-$ as the surfactant. Two different mechanisms of surfactant adsorption were observed and the fractions adsorbed by each mechanism were quantified, using different characterization techniques.

Maximum adsorbed amounts and the adsorption energies involved in each mechanism were determined applying Langmuir and Dubinin-Raduskevich adsorption models to the data.

The present study verified that surfactant adsorption in the interlayer space of the clay mineral is produced by a 'strong' adsorption mechanism, in which the surfactant forms an inner-sphere and/or charge-transfer complex with clay layers, as corroborated by ζ potential and XPS measurements. The study also confirmed the existence of a 'weak' adsorption mechanism, by Van der Waals-type interactions between carbon tails of the surfactant molecules in solution and the molecules previously adsorbed by the 'strong' mechanism.

Based on these results, the proposed interaction mechanism between the organic surfactant and the clay mineral is characterized qualitatively and, for the first time, quantitatively.

REFERENCES

Akçay, G., Akçay, M., and Yurdakoç, K. (2006) The characterization of prepared organomontmorillonite (DEDMAM) and sorption of phenoxyalkanoic acid herbicides from aqueous solution. *Journal of Colloid and Interface Science*, **296**, 428–433.

Azejjel, H., del Hoyo, C., Draoui, K., Rodríguez-Cruz, M.S., and Sánchez-Martín, M.J. (2009) Natural and modified clays from Morocco as sorbents of ionizable herbicides in aqueous medium. *Desalination*, **249**, 1151–1158.

Bilgiç, C. (2005) Investigation of the factors affecting organic cation adsorption on some silicate minerals. *Journal of Colloid and Interface Science*, **281**, 33–38.

Briggs, D. (1998) *Surface Analysis of Polymers by XPS and Static SIMS*. Cambridge University Press, New York.

Carrado, K.A. (2000) Synthetic organo- and polymer-clays: preparation, characterization, and materials applications. *Applied Clay Science*, **17**, 1–23.

de Paiva, L.B., Morales, A.R., and Valenzuela Díaz, F.R. (2008) Organoclays: Properties, preparation and application. *Applied Clay Science*, **42**, 8–24.

Donat, R., Akdogan, A., Erdem, E., and Cetisli, H. (2005) Thermodynamics of Pb^{2+} and Ni^{2+} adsorption onto natural bentonite from aqueous solutions. *Journal of Colloid and Interface Science*, **286**, 43–52.

Giles, C., Smith, D., and Huitson, A. (1974) A general treatment and classification of the solute adsorption isotherm. I. Theoretical. *Journal of Colloid and Interface Science*, **47**, 755–765.

He, H., Ding, Z., Zhu, J., Yuan, P., Xi, Y., Yang, D., and Frost, R.L. (2005) Thermal characterization of surfactant-modified montmorillonites. *Clays and Clay Minerals*, **53**, 287–293.

He, H., Frost, R.L., Bostrom, T., Yuan, P., Duong, L., Yang D., Xi, Y., and Kloprogge, J.T. (2006) Changes in the morphology of organoclays with HDTMA+ surfactant loading. *Applied Clay Science*, **31**, 262–271.

He, H., Zhou, Q., Frost, R.L., Wood, B.J., Duong, L.V., and Kloprogge, J. T. (2007) A X-ray photoelectron spectroscopy study of HDTMAB distribution within organoclays. *Spectrochimica Acta Part A: Molecular and Biomolecular Spectroscopy*, **66**, 1180–1188.

Jouniaux, L. and Ishido, T. (2010) Electrokinetics in earth sciences: A tutorial. *International Journal of Geophysics*, Volume 2012, 16 pages, doi: 10.1155/2012/286107.

Liu, G., Wu, S., van de Ven, M., Molenaar, A., and Besamusca, J. (2010) Characterization of surfactant on montmorillonite nanoclay to be used in bitumen. *Journal of Materials in Civil Engineering*, **22**, 794–799.

Mahramanlioglu, M., Kizilcikli, I., and Bicer, I. (2002) Adsorption of fluoride from aqueous solution by acid treated spent bleaching earth. *Journal of Fluorine Chemistry*, **115**, 41–47.

Seki, Y. and Yurdakoç, K. (2005) Paraquat adsorption onto clays and organoclays from aqueous solution. *Journal of Colloid and Interface Science*, **287**, 1–5.

Su, K., Radian, A., Mishael, Y., Yang, L., and Stucki, J.W. (2012) Nitrate reduction by redox-activated, polydiallyldimethylammonium-exchanged ferruginous smectite. *Clays and Clay Minerals*, **60**, 464–472.

Tahani, A., Karroua, M., Van Damme, H., Levitz, P., and Bergaya, F. (1999) Adsorption of a cationic surfactant on Na-montmorillonite: Inspection of adsorption layer by X-ray fluorescence spectroscopies. *Journal of Colloid and Interface Science*, **216**, 242–249.

Xi, Y., Martens, W., He, H., and Frost, R.L. (2005) Thermogravimetric analysis of organoclays intercalated with the surfactant octadecyltrimethylammonium bromide. *Journal of Thermal Analysis and Calorimetry*, **81**, 91–97.

Yariv, S., Lapides, Y., and Borisover, M. (2012) Thermal analysis of tetraethylammonium and benzyltrimethylammonium montmorillonites. *Journal of Thermal Analysis and Calorimetry*, **110**, 385–394.

(*Received 4 July 2012; revised 24 January 2013; Ms. 687; AE: H. He*)

Clays and Clay Minerals, Vol. 61, No. 2, 133–140, 2013.

QUANTITATIVE *IN SITU* STUDY OF THE DEHYDRATION OF BENTONITE-BONDED MOLDING SANDS

GUNTRAM JORDAN[1], CONSTANZE EULENKAMP[1], ELBIO CALZADA[2], BURKHARD SCHILLINGER[2], MARKUS HOELZEL[2], ALEXANDER GIGLER[1], HELGE STANJEK[3], AND WOLFGANG W. SCHMAHL[1]

[1] Ludwig-Maximilians-Universität München, Department für Geo- und Umweltwissenschaften, Theresienstr. 41, 80333 München, Germany

[2] Technische Universität München, FRM II, Lichtenbergstr.1, 85748 Garching, Germany

[3] RWTH Aachen, Ton- und Grenzflächenmineralogie, Wüllnerstr. 2, 52065 Aachen, Germany

Abstract—Bentonite-bonded molding sand is one of the most common mold materials used in metal casting. The high casting temperatures cause dehydration and alteration of the molding sand, thereby degrading its reusability. Neutron radiography and neutron diffraction were applied to study these processes by using pure bentonite-quartz-water mixtures in simulation casting experiments. The aim of the experiments was to compare the dehydration behavior of raw and recycled mold material in order to assess possible causes of the limited reusability of molding sands in industrial application. Neutron radiography provided quantitative data for the local water concentrations within the mold material as a function of time and temperature. Dehydration zones, condensation zones, and areas of pristine hydrated molding sand could be established clearly. The kinematics of the zones was quantified. Within four cycles of de- and rehydration, no significant differences in water kinematics were detected. The data, therefore, suggest that the industrial handling (molding-sand additives and the presence of metal melt) may have greater effects on molding-sand reusability than the intrinsic properties of the pure bentonite–quartz–water system.

Key Words—Bentonite, Dehydration Process, Metal Casting, Molding Sand, Neutron Powder Diffraction, Neutron Radiography, Smectite.

INTRODUCTION

Large quantities of casted metal parts are produced with bentonite-bonded molding sands. Smectite, as the main component of bentonite, provides the required binding properties. Binding is partially related to the negative layer charge of the smectites. In the interlayer space, cations compensate for the layer charge. These interlayer cations can hydrate reversibly, resulting in a swelling of the interlayer space. X-ray powder diffractometry (XRD) revealed the dependence of the d_{001} value on the interlayer hydration states (*e.g.* Bradley *et al*., 1937; Ferrage *et al*., 2005a, 2005b; Moore and Reynolds, 1997; Norrish, 1954). The uptake and release of water is influenced by various factors such as size, valence, hydration energy of the interlayer cation, and the charge, as well as the charge distribution of the layers (Collins *et al*., 1992; Ferrage *et al*., 2005b, 2007c; Jasmund and Lagaly, 1993; Koster van Groos and Guggenheim, 1984). Furthermore, hydration takes place discontinuously and different hydration states can coexist within an interlayer (Aldushin *et al*., 2007; Ben Brahim *et al*., 1984; Bérend *et al*., 1995; Cases *et al*., 1997; Collins *et al*., 1992; Sánchez-Pastor *et al*., 2010; Wilson *et al*., 2004). Analogously, dehydration occurs discontinuously. Investigations by XRD (Ferrage *et al*., 2007a, 2007b) showed that Ca-montmorillonite evolves during drying from one hydration state to another *via* mixed-layer structures. Thermogravimetric analysis (Bray and Redfern, 1999; El-Barawy *et al*., 1986; Guggenheim and Koster van Groos, 2001; Koster van Groos and Guggenheim, 1984; Zabat and Van Damme, 2000) showed that dehydration takes place in the range 50−350ºC depending on the experimental conditions. Bray and Redfern (1999) reported a two-step dehydration where adsorbed water was released before interlayer water. Guggenheim and Koster van Groos (1992, 2001) demonstrated that water fugacity influences the dehydration of smectites to a great extent. According to these authors, water adsorbed at surfaces plays a major role in dehydration below 100ºC. Compaction of the sample, in contrast, gained importance above 100ºC.

Although smectites have been investigated intensively, the dehydration and rehydration kinetics on an industrial scale of both pure smectite and of mold materials are not understood sufficiently. While isothermal uptake and release of interlayer water is generally considered to be a reversible process, the occurrence of sorption-desorption-hysteresis clearly indicates complex kinetics (*e.g.* Cases *et al*., 1992; Komadel *et al*., 2002). Furthermore, any alterations of the chemical state of the layers (*e.g.* Wu *et al*., 1989) or elevated temperatures (*e.g.* Ferrage *et al*., 2007a) can cause irreversible modifications of de- and rehydration behavior.

* E-mail address of corresponding author:
guntram.jordan@lrz.uni-muenchen.de
DOI: 10.1346/CCMN.2013.0610210

Industrially processed mold material loses its capability to reabsorb water (Grefhorst *et al*., 2005; Tilch, 2004). This limits considerably the reusability of the material. As a consequence, only 93−98 wt.% of the mold material is recycled after casting. Environmental aspects as well as the demands of increasing production efficiency, however, require an increased reusability rate for molding sand. A detailed understanding of the uptake and release of water in mold material is, therefore, essential.

The aim of the present study was to better understand the limitations of the reusability of molding sands in industrial applications. In order to accomplish this goal, multi-cycle experiments were performed which simulated the recurring thermal impact of industrial-scale casting on a pure quartz-bentonite-water system. The application of the pure system enabled discrimination between potential effects originating from intrinsic mineral properties (*e.g*. reversible *vs*. irreversible dehydration of smectites) and actual industrial handling (*e.g*. alterations of the mold material by the metal melt or additives such as reducing agents). Information on the spatial and temporal distribution of water within the mold material during thermal impacts was obtained by applying neutron radiography (*cf.* Fijal-Kirejczyk *et al*., 2011; Luo, 2007) and neutron powder diffractometry.

SAMPLES AND METHODS

Samples

Additive-free molding sand with a compactibility of 45−50% was obtained from S&B Industrial Minerals GmbH (Marl, Germany). The composition of the molding sand was 84 wt.% quartz sand (average grain size 0.24 mm; Frechen, Germany), 12 wt.% sodium bentonite (Wyoming, USA), and 3−4 wt.% water. The composition of the bentonite was calculated from XRD data using the software package *BGMN* (Ufer *et al*., 2008): 87 wt.% montmorillonite, 4 wt.% quartz, 4 wt.% albite, 2 wt.% muscovite, 2 wt.% calcite, 1 wt.% brookite.

Casting simulation experiment

A container (approx. size 140 mm × 67 mm × 60 mm) was filled with molding sand and equipped with thermocouples located at heights of ~0, 10, 20, 30, 40, and 50 mm (Figure 1a). The container was mounted in an experimental stand at the neutron imaging facility ANTARES (FRM II, Germany; Schillinger *et al*., 2006) and dropped onto a preheated hotplate (~650ºC; Figure 1b) while taking neutron radiographs (2048 × 2048 pixel CCD camera, 2 × 2 binning mode, spatial sample resolution ~0.15 mm). The temperature of the hotplate was chosen in order to avoid massive dehydroxylation of smectites progressing far into the bulk molding sand. In order to facilitate constant thermal conditions in the beam direction, low heat flow from the copper-baseplate to the front and rear aluminum walls of the container was desirable. The front and rear walls, therefore, were mounted at a distance of 3 mm from the baseplate of the container. Thus, the container had a 3 mm wide slit at the bottom edges between the baseplate and the front and rear walls. The radiograph acquisition frequency was ~0.21 Hz which determined the temporal resolution of the experiments. The neutron radiography observations lasted for ~24 min. A detailed description of the experimental set-up can be found in Schillinger *et al*. (2011).

The water lost by the dehydration experiments was determined gravimetrically. De-ionized water was then added to the dehydrated sand. Due to the limited accuracy of the gravimetric determination (~0.1% of the total mass of sand and container), the mass of added water varied in multi-cyclic experiments by up to ~10%. The re-moistened molding sand was homogenized with a blender for ~5 min. The sand was then left undisturbed in a plastic bag for 3 days (the possibility of water loss during this period cannot be excluded completely). In all experiments, loading of the container and compaction of the sand were conducted in a standardized way to ensure maximum homogeneity and the best possible reproducibility.

Neutron radiography contrast

Attenuation of the neutron beam by transmission through the mold container from its initial intensity, I_0, to intensity I can be described by:

$$I/I_0 = \exp\left(-\sum_i \delta_i x_i\right) \quad (1)$$

where δ_i is the attenuation coefficient of the phase i, and x_i is the partial path length of the neutron beam passing through phase i with $x_i = a_i\, x$ (where a_i is the partial length coefficient and x is the beam-path length of the entire mold container).

Because neutron attenuation depends on the amount of hydrogen in the beam path, the hydration state of the molding sand can be correlated directly to the neutron intensity detected by the CCD camera. The sum in equation 1, therefore, can be split into one term for the mold container filled with dehydrated molding sand (s) and a second term accounting for water (w). The logarithm of equation 1 then yields:

$$\ln(I/I_0) = -\delta_s x_s - \delta_w x_w \quad (2)$$

Converting the radiography detector signal into linearly normalized grayscales (GS_n) between unity for the open beam without any sample ($I = I_0$; $GS_{n\ \text{open beam}} = 1 = I/I_0$) and zero for the beam shut off ($I = I/I_0 = 0$; $GS_{n\ \text{dark image}} = 0$), equation 2 yields:

$$\ln(GS_n) = -\delta_s x_s - \delta_w x_w \quad (3)$$

For the normalized grayscales in a dehydrated reference radiograph ($GS_{n\ \text{dehydr}}$), the last term vanishes:

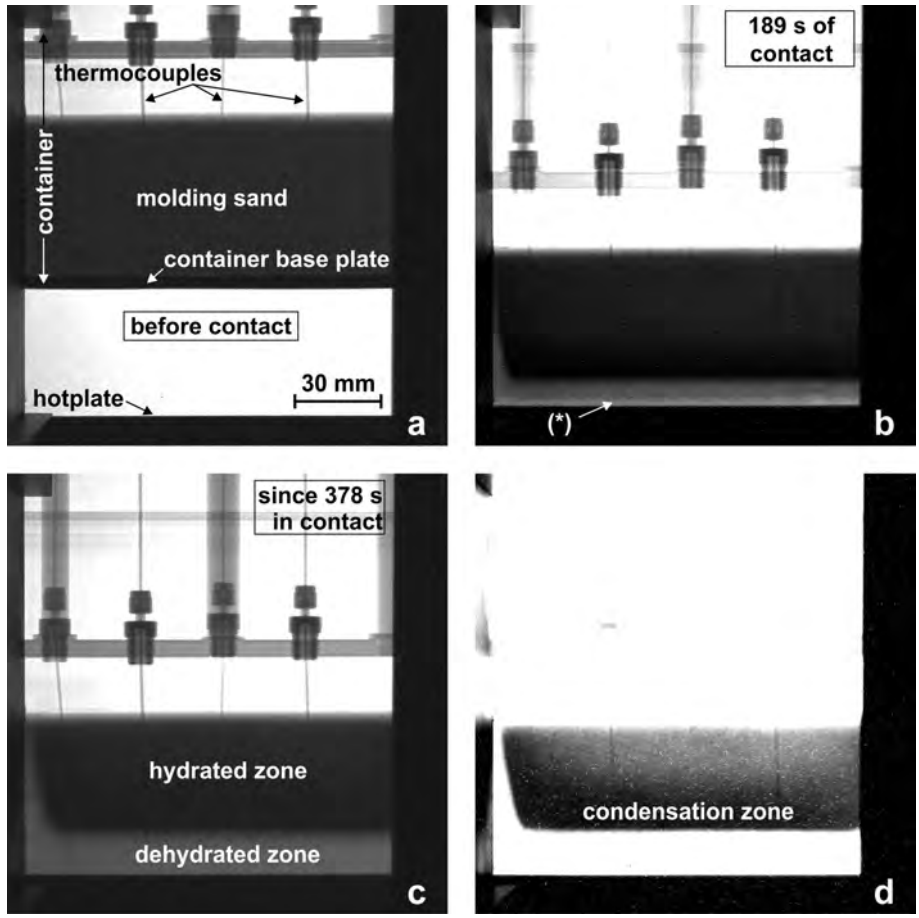

Figure 1. Neutron radiographs of a casting simulation experiment. Image grayscales are a measure of the neutron scattering intensity. Changes in the intensity essentially correlate with changes in the local concentration of water. (a) Radiograph shows the molding-sand container (equipped with thermocouples) ~45 mm above the hotplate. (b) The container has been in contact with the hotplate for 189 s. The molding sand in the lowest region of the container is dehydrated. (c) A further 189 s later the vertical extent of the dehydrated zone has grown significantly. (d) Same radiograph as in part c with adjusted brightness and contrast settings. The modified settings allow the identification of a condensation zone located in the lower range of the hydrated zone.

$$\ln(GS_{n\ \mathrm{dehydr}}) = -\delta_s x_s \tag{4}$$

Combining equations 3 and 4 yields:

$$x_w = \frac{\ln(GS_{n\ \mathrm{dehydr}}) - \ln(GS_n)}{\delta_w} \tag{5}$$

Taking into account a neutron attenuation coefficient for water $\delta_w = 5.415\ \mathrm{cm}^{-1}$ (www.ncnr.nist.gov with λ = 4 Å) and the bulk density of the molding material (obtained from the weight and fill level of the container), equation 5 permits determination of the wt.% of water of the molding material displayed in the radiographs within the above-mentioned limits of spatial and temporal resolution.

Note, however, that the incident neutron beam is not mono-energetic but has a spectrum mostly ranging from 1.8 to 6 Å, centered around 3.5–4 Å. In addition, the tabulated attenuation coefficient treats scattering like absorption (*i.e.* scattered neutrons do not reach the detector) and does not account for forward-scattered neutrons that hit the large detector area under small angles, leading to a diffuse background. The additional absolute error may well be up to ~15%, but cannot be quantified without extensive numerical simulations. However, comparing the conditions of this study (x_w < 3 mm for the fully hydrated molding sand; sample–detector distance >5 cm) with the scattering profiles obtained by Hassanein (2006), no significant contribution of scattered neutrons in the radiographs was expected. Furthermore, at a neutron transmission below ~15%, multiple scattering may affect the accuracy of the quantification of absolute water contents to some extent. The accuracy of equation 5, therefore, decreases with increasing mold-container thickness and increasing water content. The molding sand used in the experiments yielded transmissions ranging from ~8% (fully hydrated) to ~30% (dehydrated). The experiments below, however,

compare relative measurements under very similar conditions.

Neutron powder diffraction

In order to identify different hydration states of smectite by an evaluation of the position and intensity of the 001 peak, neutron powder diffraction was conducted using the thermal high-resolution neutron powder diffractometer SPODI (FRM II, Germany; Hoelzel *et al*., 2012). The molding sand (mass ~5 g) was analyzed in its original state, after dehydration in the casting simulation experiment, and after rehydration. All neutron diffraction measurements were performed at room temperature and wavelengths λ = 2.396 Å or 2.536 Å using a germanium (331) monochromator at take-off angles of 135º or 155º, respectively. A possible λ/3 contribution was avoided by a graphite filter. The positions of the 001 peaks in the diffraction patterns have been verified by applying the Rietveld refinement program *BGMN* which uses a fundamental parameter approach to model the peak profiles (Ufer *et al*., 2004). For the instrumental resolution function of SPODI, a width formula for a single squared Lorentzian was used.

RESULTS

Casting simulations

Neutron radiography recorded the temporal and spatial intensity variations of the neutron beam passing through the mold-sand container during the experimental casting simulation. Because hydrogen fluxes are controlling these intensity variations almost exclusively, dehydration processes and water fluxes could be accessed directly and quantitatively.

Neutron radiographs were taken from the mold-sand container in contact with a hotplate underneath (Figure 1b). A 3 mm zone of significant dehydration (recognizable by lighter grayscales) initiated at the bottom of the container (asterisk in Figure 1b). This zone was caused by rapid venting of water vapor through the 3 mm slits between the front and rear walls and the baseplate of the container (see above). With increasing residence time of the container on the hotplate (Figure 1c), dehydration of the molding sand continued upwards. Dehydrated molding sand in the lower region and hydrated sand on top were easily distinguished visually. Modified brightness and contrast settings of the detector data (*cf.* Figure 1c,d) also revealed an increased amount of water in the lower range of the hydrated sand region.

The normalized detector data (GS_n) were taken along vertical profiles of the mold container (profile data point = mean value from a horizontal 1×330 pixel strip). The profile data were converted into water-concentration profiles by applying equation 5 and using the density of the mold material in the container. The mean grayscale of the most dehydrated parts of the sand in the last three images of the radiograph sequence was used as a reference value for $GS_{n\ \mathrm{dehydr}}$. Thermocouples placed in this area indicated a temperature range of 200−250ºC. The radiographs did not give any indication of a dehydroxylation reaction in these areas. Water concentration profiles (Figure 2a) were obtained from radiographs of dehydrating raw molding sand (first dehydration) and of molding sand that has been de- and rehydrated four times before (Figure 2b).

The hydration states at the locations of two different thermocouples (2 and 3 cm above the container baseplate) were plotted *vs*. the corresponding temperature readings of the thermocouples for the two different molding sands (Figure 3). Assuming that water was the only mobile component in the system, the plots can be perceived as local thermo-gravimetric measurements within larger sample systems. Note that these local measurements also revealed reallocations of water within a sample, whereas standard thermo-gravimetric analyses integrated over the entire sample volume and measured only the net escape of water from a system. Furthermore, due to the non-linearity of the local heating rate, the temperature scales of such plots (Figure 3) did not correspond to a linear time scale. The water contents *vs*. temperature plots (Figure 3) revealed the general behavior of an initial increase in water concentration, followed by a decrease above ~100ºC. Time-synchronization errors of radiography and temperature data logging limited the precision of the determination of the transition point between hydration and dehydration.

Neutron diffractometry

Neutron powder diffractometry of raw molding sand revealed smectite d_{001} values of ~19 Å (Figure 4). After dehydration in the experimental casting simulation stand, the molding sand was measured again. A smectite d_{001} value of 9.7 Å was observed. Subsequently, the molding sand was rehydrated by adding the gravimetrically determined amount of lost water and a resting period of 3 days. The sand revealed smectite d_{001} values of ~19 Å again.

A second set of diffractometry experiments focused on rehydration kinetics. After dehydration of the molding sand, the lost water was determined gravimetrically and re-added. The sand was then homogenized and left undisturbed for ~30 min. Subsequently, diffraction patterns were taken every 90 min over a period of 8.5 h. The water uptake of smectite interlayers was monitored by the position of the 001 reflection of smectite. The d_{001} value expanded to ~19 Å within 2.5 h and remained constant thereafter (Figure 5).

DISCUSSION

Different hydration states of smectite interlayers result in different d_{001} values (*e.g.* Couture, 1985; Ferrage *et al*., 2005a, 2005b; Jasmund and Lagaly,

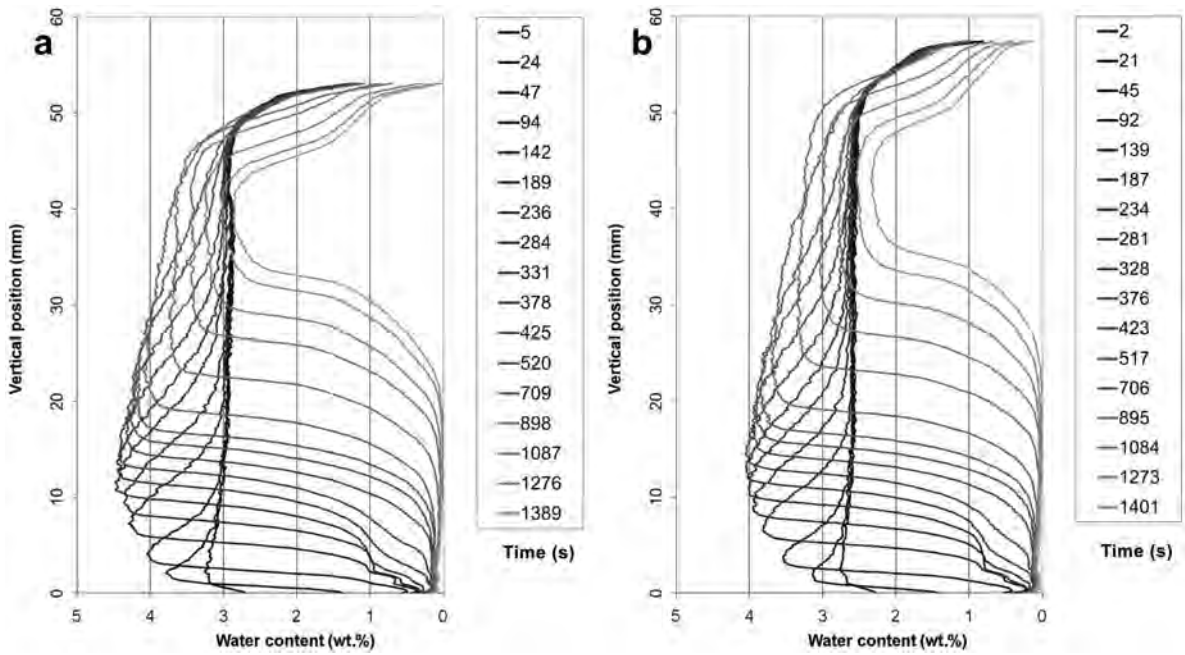

Figure 2. Evolution of the water concentration profiles in a raw molding sand (a) and a recycled molding sand (b) during the casting simulation experiment. The water concentrations were converted from the grayscales taken over the entire vertical extent of the molding-sand container obtained at given times in the respective radiograph.

1993; Wilson *et al*., 2004). Non-hydrated Na- and Ca-smectites have d_{001} values of 9.6−10.1 Å. Mono- and bi-hydrated smectites show 12.3−12.7 Å and 15.1−15.8 Å, respectively. The uptake of three water layers leads to d_{001} values of 19−20 Å. Identification of the hydration states of smectite in molding sand was made possible by neutron powder diffraction in spite of the small amount, 12 wt.%. Smectites in raw molding sand showed d_{001} values of ~19 Å (Figures 4 and 5) which correspond to smectite interlayers with three water layers (Wilson *et al*., 2004). This indicates that the smectite interlayers in the raw molding sand used for casting simulation were fully hydrated.

After the heat treatment, the molding sand was extracted from the casting simulation apparatus and analyzed by neutron diffractometry. The d_{001} values decreased to ~9.7 Å, which indicates complete dehydration. This result was confirmed by Ferrage *et al*. (2007a) who observed a transition from mono- to dehydrated Ca-montmorillonite at temperatures >90ºC. The authors further report that the relative abundance of dehydrated interlayers was ~70% after 950 s at 125ºC. Complete dehydration was predicted to occur at ~170ºC.

After the dehydration experiments, the amount of water lost was determined gravimetrically and was re-added to the dehydrated molding sand. Neutron diffractometry (Figures 4 and 5) showed that the smectite d_{001} values increased to ~19 Å (corresponding to three water layers) within 2.5 h. Therefore, the smectites of recycled molding sand used in subsequent dehydration experiments (Figure 2b) had had the same hydration state as pristine molding sand. Note, however, that due to small differences in the shape of the d_{001} peak, hydration heterogeneities within the smectites cannot be discounted completely.

The formation of three water layers within 2.5 h contradicts the statement of Dieng (2005) who reported rehydration of pores within ~1 h and of interlayers within a day or more. Although the compositions of the samples used by Dieng (2005) were not fully defined, the smectite contents (25−97%) were substantially greater than the 12 wt.% used here. A possible dependence of the hydration state of the smectites on the porosity (and, therefore, of the water transport capacity of the samples) cannot be excluded.

Comparing the neutron radiographs of raw and recycled molding sand (*cf*. Figure 2), the general process of dehydration was identical. Within the limits of temporal resolution of radiography, the release of water started instantaneously upon contact of container and hotplate. Initially, water vapor migrated in two directions: it rose and re-condensed in the still colder zone above and it vented through the slits between baseplate and container walls. The larger the dehydrated zone grew, the less water vented through the base slits. After ~300 s, the amount of water venting through the slits was negligible and upward transport to the condensation zone took place exclusively. After ~700 s, water concentration profiles were considerably influenced by the fill level of molding sand in the container.

The maximum local water concentration correlated with a temperature of ~100ºC (Figure 3). With increas-

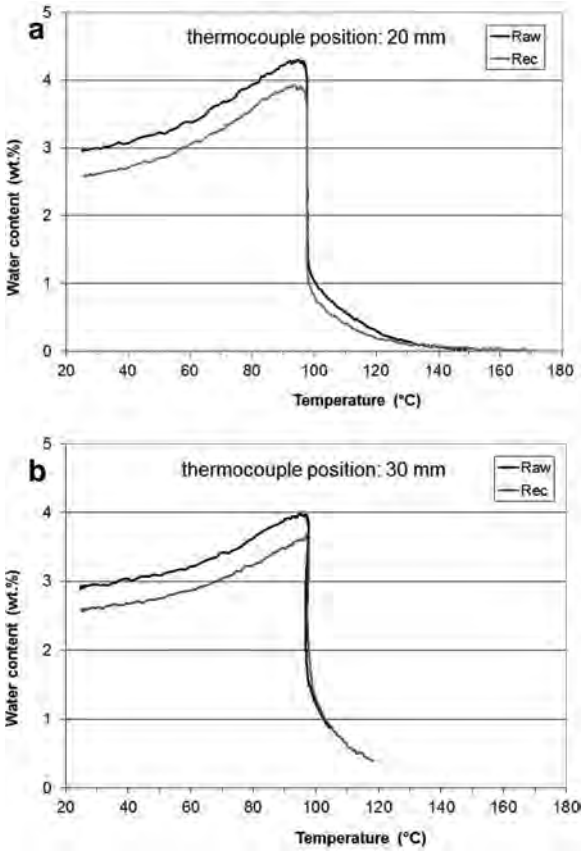

Figure 3. Plots of water concentrations obtained from the radiographs during an entire casting simulation experiment at the position of a thermocouple *vs*. the related temperature reading. For better comparison, the plots of raw (Raw) and recycled (Rec) molding sands were grouped for the thermocouples located 20 mm (a) and 30 mm (b) above the base plate.

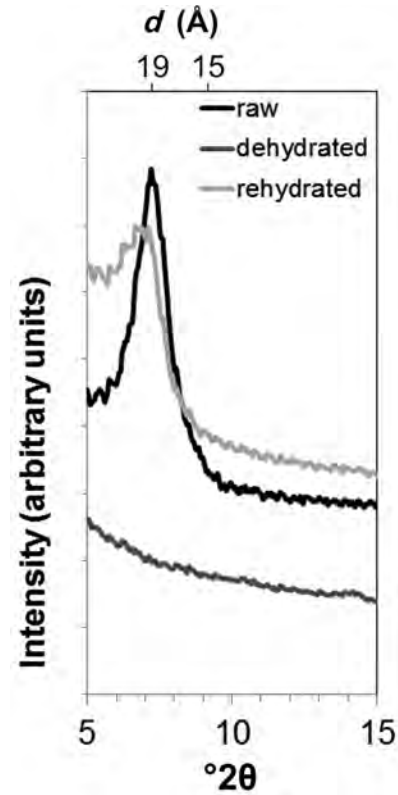

Figure 4. 001 reflection of smectites in neutron powder diffraction patterns (λ = 2.396 Å) of molding sands. The raw and rehydrated molding sands have similar d_{001} values of ~19 Å. The diffractogram of dehydrated molding sand shows a peak with very weak intensity at ~14.2º2θ yielding a *d* value of ~9.7 Å. The intensities were normalized to the incident neutron counts.

ing temperature, the water concentration reduced rapidly. Subsequently, the dehydration rate decreased continuously until dehydration ceased in the temperature range 170–220ºC. Above 100ºC, neither the vertical profiles (Figure 2) nor the plots of local water concentrations *vs*. temperature (Figure 3) revealed any sign of an onset of a new process associated with a noticeable release of hydrogen. Within the period of radiographic observation, no indication of a dehydroxylation of the octahedral sheets of smectite was, therefore, observed. However, the possibility that thermal treatment caused a chemical alteration of some smectites which may have led to a modified re-hydration behavior of these minerals cannot be ruled out. Irreversible dehydration taking place at temperatures above 90ºC was reported by Ferrage *et al*. (2007a).

Irrespective of any possible alteration of the smectites, all water lost from the molding sand by the casting simulation was re-added within the accuracy of the gravimetric measurement. A potential deficit of water within the interlayers would result in a surplus of pore water. Therefore, the observed differences in the initial water concentrations of the raw and recycled molding sand (Figure 3) cannot be associated with a reduced capacity of smectites to reabsorb water but rather with the limited accuracy of the water-loss measurement.

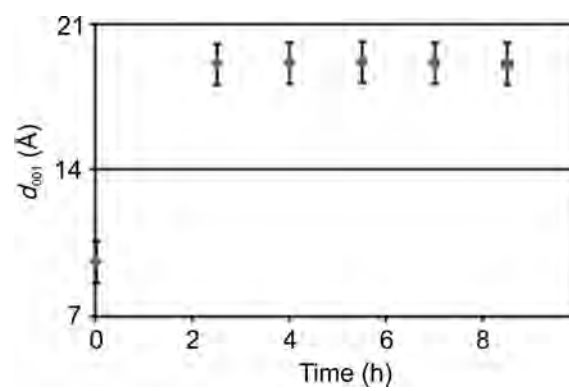

Figure 5. Neutron powder diffraction data of rehydrating molding sand. The d_{001} values of smectite were plotted *vs*. the rehydration time. The *d* values were verified using the Rietveld program code *BGMN*.

An important point of the casting simulation experiment is that, prior to any dehydration, molding sand first and foremost is subject to a hydration process within the condensation zone at temperatures up to 100ºC. Whether these hot-hydrous conditions lead to a rapid hydration of a few still dehydrated interlayers (which may be present in some smectites) or whether the hot-hydrous conditions (rather than the subsequent hot-dry conditions) are more likely to alter the chemical state of smectites and to reduce their de- and rehydration capacity is unknown. In bentonite samples at least, steam has been identified to efficiently reduce the swelling capacity (Couture, 1985).

Irrespective of the effects of the condensation zone, neutron diffractometry showed that the smectite interlayers in all casting simulation experiments were hydrated and that the concentration of chemically modified smectites, if present at all, was below the detection limit. The only obvious difference between the raw and recycled molding sand directly prior to the onset of dehydration at ~100ºC, therefore, is pore-water concentration. For temperatures above 100ºC, Guggenheim and Koster van Groos (2001) suggested that dehydration kinetics of surface-adsorbed water may be controlled by sand compaction rather than binding affinity. This may also hold for pore water. A correlation between molding-sand compaction and dehydration kinetics can be expected and may explain the observed similar dehydration behavior of raw and recycled molding sand.

CONCLUSIONS

The kinetics of dehydration of the pure quartz-bentonite-water system in the casting simulation experiments performed here was probably controlled by the compaction of the material. Due to similar compaction of the molding sand used here, the dehydration kinetics of both raw and recycled molding sand revealed no significant difference. Further experiments should, therefore, focus on small-scale variations of water contents and its distribution kinetics within a porous system, where diffusional transport might be much more important relative to mechanical mixing.

If the casting simulation experiments caused irreversible alterations of smectites, the effects of these alterations on the dehydration kinetics were insignificant within the number of cycles performed. The occurrence of fast and significant reduction of molding-sand binding properties by industrial handling, therefore, seems more likely to be a consequence of the industrial handling (*e.g.* alterations by the metal melt or additives) rather than originating from naturally intrinsic mineral properties (*e.g.* irreversibility of smectite dehydration). The application of neutron radiography, *e.g.* to additive-containing moldings sands, could help to identify the main cause of the loss of quality of the molding sand.

ACKNOWLEDGMENTS

Help with the Rietveld refinement program *BGMN* provided by the late Jörg Bergmann is gratefully acknowledged. Molding-sand samples were kindly provided by S&B Industrial Minerals GmbH. The work was supported financially by the BMBF/DFG Sonderprogramm Geotechnologien (Forschungsvorhaben 03G0707). The comments provided by the Editor in Chief, the Associate Editor, and two anonymous reviewers improved the manuscript considerably and are gratefully acknowledged.

REFERENCES

Aldushin, K., Jordan, G., Aldushina, E., and Schmahl, W.W. (2007) On the kinetics of ion-exchange in phlogopite – an *in situ* AFM study. *Clays and Clay Minerals*, **55**, 339–347.

Ben Brahim, J., Besson, G., and Tchoubar, C. (1984) Etude des profils des bandes de diffraction X d'une beidellite-Na hydratée à deux couches d'eau. Détermination du mode d'empilement des feuillets et des sites occupés par l'eau. *Journal of Applied Crystallography*, **17**, 179–188.

Bérend, I., Cases, J.M., Francois, M., Uriot, J.P., Michot, L., Masion, A., and Thomas, F. (1995) Mechanism of adsorption and desorption of water vapor by homoionic montmorillonite: 2. The Li^+, Na^+, K^+, Rb^+ and Cs^+ exchanged forms. *Clays and Clay Minerals*, **43**, 324–336.

Bradley, W.F., Grim, R.E., and Clark, G.F. (1937) A study of the behavior of montmorillonite upon wetting. *Zeitschrift für Kristallographie*, **97**, 260–270.

Bray, H.J. and Redfern, S.A.T. (1999) Kinetics of dehydration of Ca-montmorillonite. *Physics and Chemistry of Minerals*, **26**, 591–600.

Cases, J.M., Bérend, I., Besson, G., Francois, M., Uriot, J.-P., Thomas, F., and Poirier, J. (1992) Mechanism of adsorption and desorption of water vapor by homoinonic montmorillonite. 1. The sodium-exchanged form. *Langmuir*, **8**, 2730–2739.

Cases, J.M., Bérend, I., Francois, M., Uriot, J.P., Michot, L.J., and Thomas, F. (1997) Mechanism of adsorption and desorption of water vapor by homoionic montmorillonite: 3. The Mg^{2+}, Ca^{2+}, Sr^{2+} and Ba^{2+} exchanged forms. *Clays and Clay Minerals*, **45**, 8–22.

Collins, D.R., Fitch, A.N., and Catlow, C.R. (1992) Dehydration of vermiculite and montmorillonite: A time resolved powder neutron diffraction study. *Journal of Materials Chemistry*, **2**, 865–873.

Couture, R. (1985) Steam rapidly reduces the swelling capacity of bentonite. *Nature*, **318**, 50–52.

Dieng, M.A. (2005) Der Wasseraufnahmeversuch nach DIN 18132 in einem neu entwickelten Gerät. *Bautechnik*, **82**, 28–32.

El-Barawy, K.A., Girgis, B.S., and Felix, N.S. (1986) Thermals treatment of some pure smectites. *Thermochimica Acta*, **98**, 181–189.

Ferrage, E., Lanson, B., Malikova, N., Plançon, A., Sakharov., B.A., and Drits, V.A. (2005a) New insights on the distribution of interlayer water in Bi-hydrated smectite from X-ray profile modeling of 00l reflections. *Chemistry of Materials*, **17**, 3499–3512.

Ferrage, E., Lanson, B., Sakharov. B.A., and Drits, V.A. (2005b) Investigation of smectite hydration properties by modeling of X-ray diffraction patterns: Part I. Montmorillonite hydration properties. *American Mineralogist*, **90**, 1358–1374.

Ferrage, E., Kirk, C., Cressey, G., and Cuadros, J. (2007a) Dehydration of Ca-montmorillonite at the crystal scale. Part 1. Structure evolution. *American Mineralogist*, **92**, 994–1006.

Ferrage, E., Kirk, C., Cressey, G., and Cuadros, J. (2007b) Dehydration of Ca-montmorillonite at the crystal scale. Part 2. Mechanisms and kinetics. *American Mineralogist*, **92**, 1007–1017.

Ferrage, E., Lanson, B., Sakharov, B.A., Geoffroy, N., Jacquot, E., and Drits, V.A. (2007c) Investigation of dioctahedral smectite hydration properties by modeling of X-ray diffraction profiles: Influence of layer charge and charge location. *American Mineralogist*, **92**, 1731–1743.

Fijal-Kirejczyk, I.M., Milczarek, J.J., and Zoladek-Nowak, J. (2011) Neutron radiography observations of inner wet region in drying of quartz sand cylinder. *Nuclear Instruments and Methods in Physics Research A*, **651**, 205–210.

Grefhorst, C., Podobed, O., and Böhnke, S. (2005) Bentonitgebundene Formstoffe: Umlaufverhalten von Bentoniten unter besonderer Betrachtung des Kreislaufsystems und der Nasszugfestigkeit. *Gießerei*, **92**, 63–67.

Guggenheim, S. and Koster van Groos, A.F. (1992) High-pressure differential thermal analysis (HP-DTA). I. Dehydration reactions at elevated pressures in phyllosilicates. *Journal of Thermal Analysis*, **38**, 1701–1728.

Guggenheim, S. and Koster van Groos, A.F. (2001) Baseline studies of the Clay Minerals Society Source Clays: thermal analysis. *Clays and Clay Minerals*, **49**, 433–443.

Hassanein, R.K. (2006) Correction methods for the quantitative evaluation of thermal neutron tomography. PhD dissertation No 16809, ETH Zürich, Switzerland, 102 pp.

Hoelzel, M., Senyshyn, A., Juenke, N., Boysen, H., Schmahl, W., and Fuess, H. (2012) High-resolution neutron powder diffractometer SPODI at research reactor FRM II. *Nuclear Instruments and Methods in Physics Research A*, **667**, 32–37.

Jasmund, K. and Lagaly, G. (editors) (1993) *Tonminerale und Tone*. Steinkopff Verlag, Darmstadt, Germany.

Komadel, P., Hrobáriková, J., Smrčok, L., and Koppelhuber-Bitschnau, B. (2002) Hydration of reduced-charge montmorillonite. *Clay Minerals*, **37**, 543–550.

Koster van Groos, A.F. and Guggenheim, S. (1984) The effect of pressure on the dehydration reaction of interlayer water in Na-montmorillonite (SWy-1). *American Mineralogist*, **69**, 872–876.

Luo, X. (2007) Study of infrastructure materials using neutron radiography and diffraction. PhD dissertation, University of Tennessee, Knoxville, USA, 192 pp.

Moore, D.M. and Reynolds, R.C. Jr. (1997) *X-ray Diffraction and Identification and Analysis of Clay Minerals*. Oxford University Press, Oxford, UK and New York.

Norrish, N. (1954) The swelling of montmorillonite. *Discussions of the Faraday Society*, **18**, 120–133.

Sánchez-Pastor, N., Aldushin, K., Jordan, G., and Schmahl, W.W. (2010) K^+-Na^+ exchange in phlogopite on the scale of a single layer. *Geochimica et Cosmochimica Acta*, **74**, 1954–1962.

Schillinger, B., Calzada, E., and Lorenz, K. (2006) Modern neutron imaging: Radiography, tomography, dynamic and phase contrast imaging with neutrons. *Solid State Phenomena*, **112**, 61–72.

Schillinger, B., Calzada, E., Eulenkamp, C., Jordan, G., and Schmahl, W.W. (2011) Dehydration of moulding sand in simulated casting process examined with neutron radiography. *Nuclear Instruments and Methods in Physics Research A*, **651**, 312–314.

Tilch, W. (2004) Ermittlung des Aufbereitungsverhaltens bentonitgebundener Formstoffe (Betriebssande). *Gießerei-Praxis*, **1/2004**, 12–18.

Ufer, K., Roth, G., Kleeberg, R., Stanjek, H., Dohrmann, R., and Bergmann, J. (2004) Description of X-ray powder pattern of turbostratically disordered layer structures with a Rietveld compatible approach. *Zeitschrift für Kristallographie*, **219**, 519–527.

Ufer, K., Stanjek, H., Roth, G., Dohrmann, R., Kleeberg, R., and Kaufholf, S. (2008) Quantitative phase analysis of bentonites by the Rietveld method. *Clays and Clay Minerals*, **56**, 272–282.

Wilson, J., Cuardros, J., and Cressey, G. (2004) An *in situ* time-resolved XRD-PSD investigation into Na-montmorillonite interlayer and particle rearrangement during dehydration. *Clays and Clay Minerals*, **52**, 180–191.

Wu, J., Low, P.F., and Roth, C.B. (1989) Effects of octahedral-iron reduction and swelling pressure on interlayer distances in Na-nontronite. *Clays and Clay Minerals*, **37**, 211–218.

Zabat, M. and Van Damme, H. (2000) Evaluation of the energy barrier for dehydration of homoionic (Li, Na, Cs, Mg, Ca, Ba, $Al_x(OH)_y^{z+}$ and La)-montmorillonite by a differentiation method. *Clay Minerals*, **35**, 357–363.

(*Received 22 November 2012; revised 7 March 2013; Ms. 728; AE: S. Kadir*)

Clays and Clay Minerals, Vol. 61, No. 2, 141–151, 2013.

MAPPING KAOLINITE AND DICKITE IN SANDSTONE THIN SECTIONS USING INFRARED MICROSPECTROSCOPY

VALENTIN ROBIN*, SABINE PETIT, DANIEL BEAUFORT, AND DIMITRI PRÊT

Université de Poitiers, CNRS UMR 7285 IC2MP, HydrASA Bât. B35, rue Michel Brunet, F-86022 Poitiers Cedex, France

Abstract—A method to characterize and map both kaolinite and dickite polytypes in sandstone thin sections using infrared microspectroscopy (IRMS) was developed. Minerals identification using IRMS can be performed using the hydroxyl-stretching band of most clay minerals (3500−4000 cm^{-1}) in spite of infrared (IR) interferences caused by the embedding resin and glass substratum. Emphasis was placed on determining the optimum analytical conditions for IR data acquisition. The best data-acquisition parameters for Fourier-transform infrared (FTIR) measurements (*i.e.* spectra quality as a function of beam size and the number of scans) were obtained from a series of single spectra. Then, spatial resolution was explored as a function of the IR beam size (from 50 μm × 50 μm to 15 μm × 15 μm) and the step-scan interval (*i.e.* the distance between two successive analysis points). The IRMS measurements were performed on thin sections of materials characterized previously using scanning electron microscopy (SEM) and chemical analysis. Using IRMS, locations on the thin sections containing nearly pure dickite or kaolinite polytypes were identified and mapped. Most spectra collected using IRMS represented kaolin mineral aggregates rather than individual crystals, however, and mixing of kaolin polytypes was common at the spatial resolution of the IR beam size used. The spatial resolution of the IRMS was comparable to optical petrography and made possible the identification of areas on the thin section for further '*in situ*' investigation using other methods (*e.g.* microprobe, Laser Ablation Inductively Coupled Plasma Mass Spectrometry – LA-ICP-MS, *etc*.). Also, the use of blocky crystal morphology to identify dickite was questioned, as kaolinite with blocky habit was identified. Mineral mapping using IRMS seems particularly suited for investigating petrographic relationships between kaolinite and dickite in sandstone diagenesis, but could also be used for clay minerals in other rock types or soils.

Key Words—Dickite, IR Microspectroscopy, Kaolinite, Mineral Mapping, Sandstone.

INTRODUCTION

Over the last decade, most of the advances in quantitative petrology involved the extensive use of modern image-processing techniques providing quantitative measurements of the spatial heterogeneities of rocks (mineralogy, texture, porosity...). Such mapping methods are the primary means for determining the exact relationships between mineral species and pores for researchers attempting to model the dissolution-crystallization processes experienced by rocks over geological time periods and their resulting petrophysical properties. Several methods based on chemical element mapping (acquired using various techniques) have been proposed to build mineral mapping in clay-rich natural rocks or engineered materials (De Andrade *et al.*, 2006; Munoz *et al.*, 2006; Prêt *et al.*, 2010a, 2010b). These methods are limited by the fact that they do not identify and are not able to visualize the polytypes of clay minerals. Furthermore, any methods which allow the visualization of the petrographic relationships between dickite and kaolinite in thin sections of sedimentary rocks would be of major interest to those investigating the kaolinite-to-dickite transition, which is a marker of the thermal history of sandstones during silicoclastic diagenesis (Beaufort *et al.*, 1998; Ehrenberg *et al.*, 1993; Lanson *et al.*, 1996, 2002). Classical methods for identification of clay minerals from powders (X-ray diffraction, XRD, or FTIR spectroscopy on KBr pellets) do not allow for localization of kaolin polytypes within the rocks being examined. Using the morphology of the crystals observed using a scanning electron microscope, *i.e.* vermiform habit for kaolinite *vs.* blocky habit for dickite (McAulay *et al.*, 1994; Osborne *et al.*, 1994), remains a rather subjective approach which can be contradicted by transmission electron microscopy (TEM) investigations (Kameda *et al.*, 2008). Moreover, building maps from localized characterizations of kaolin polytypes obtained by the use of electron back-scattering diffraction (EBSD) on individual crystals (Kogure *et al.*, 2005) or TEM through a focused ion beam (Kogure *et al.*, 2005) is difficult.

IRMS of thin sections is classically used for the petrographic study of rocks. However, few works dealing with IRMS for *in situ* characterization of clays are available in the literature. A polarizing infrared microspectrometer was used for the study of OH configuration on single crystals of kaolinite and dickite (Johnston *et al.*, 1990) and of muscovite (Tokiwai and Nakashima, 2010). Kaolinite was characterized by

* E-mail address of corresponding author:
valentin.robin@univ-poitiers.fr
DOI: 10.1346/CCMN.2013.0610211

reflection-mode IRMS (Rintoul and Fredericks, 1995) but only one study has dealt with the use of IRMS to characterize kaolinite in petrographic thin sections (Beauvais and Bertaux, 2002).

In the present study, the mapping of clay minerals by IRMS from thin sections of rocks was accomplished for the first time. Kaolin polytypes in thin sections of sandstones were identified and mapped using IRMS. Efforts to determine the best analytical conditions (single spectrum and mapping parameters) to optimize data acquisition were emphasized. The effects of acquisition parameters on spectrum statistics (beam size and number of scans) were evaluated from a single-point analysis prior to optimization of map parameters (step scan as a function of beam size).

EXPERIMENTAL

Materials

The specimen analyzed in the present study was a thin section obtained from a core sample collected within the oil-bearing Middle Jurassic Brent Group sediments of the Froy hydrocarbon reservoir (Norwegian continental shelf, North Sea). The specimen consists of a fine- to medium-grained arkosic sandstone lithified during burial to a depth of 3200 m. This specimen (referred to as 25/2-13 3417.85m) belongs to the series of samples investigated to refine the kaolinite–dickite transformation mechanism in sandstone reservoirs (Cassagnabère, 1998; Kameda *et al.*, 2008; Lanson *et al.*, 2002). According to mineralogical analyses based on XRD, differential thermal analyses, and IR spectroscopy, Cassagnabère (1998) determined that the kaolin material extracted from this specimen consists of a mixture of dickite (85%) and kaolinite (15%). More information about the mineral sequence and the diagenetic processes experienced by this sandstone can also be found in Cassagnabère (1998).

Associated FTIR features of kaolinite/dickite specimens

The 3500–3750 cm^{-1} IR range is usually used to distinguish the kaolin minerals. The FTIR spectra of the three kaolin polymorphs are significantly different. At ambient temperature, kaolinite exhibits four bands in the OH-stretching region at ~3695, 3668, 3652, and 3620 cm^{-1}, noted as ν_1, ν_2, ν_3, and ν_4, respectively, while only three bands at 3710, 3655, and 3622 cm^{-1} are observed for dickite (Farmer and Russell, 1964; Farmer, 1998; Frost *et al.*, 1997; Frost and Van Der Gaast, 1997; Ledoux and White, 1964; Madejová *et al.*, 2010; Prost *et al.*, 1987). Only four OH groups are present in the kaolinite unit cell (Bish, 1993), but the one-to-one assignment of the ν_1, ν_2, ν_3, and ν_4 to these single OH groups is incorrect based on their dichroic behavior (Farmer, 1974; Johnston *et al.*, 1990). Accordingly, first-principles modeling (Balan *et al.*, 2001, 2005, 2010) attributed the ν_1, ν_2, and ν_3 bands to vibrations of the three inner-surface OH groups, with ν_1 corresponding to the in-phase stretching mode and ν_2 and ν_3 to the anti-phase stretching modes, the ν_4 band being due to vibrations of the inner hydroxyl. The origin of the OH-stretching bands of dickite is still debated (Balan *et al.*, 2010).

Empirically, the wavenumber and the relative absorbance of the structural OH-stretching bands are commonly used as indicators of order/disorder in kaolin minerals. Some crystalline defaults in kaolinite, mostly related to stacking faults, may lead to local dickite-like features and the ratio of the ν_2 and ν_3 relative integrated intensities are commonly used as an order or disorder index reflecting the 'dickitic' or monoclinic character of kaolinite (Brindley *et al.*, 1986; Farmer and Russell, 1964; Farmer, 1974; Farmer, 1998; Frost *et al.*, 1997; Frost and Van Der Gaast, 1997; Prost *et al.*, 1989). By increasing the resolution of the IR spectra of the OH groups, low-temperature spectra allow clearer identification of dickite- and nacrite-like local configurations in disordered kaolinite (Balan *et al.*, 2010; Johnston *et al.*, 1990, 2008; Prost *et al.*, 1987, 1989).

Increasing amounts of dickite in a kaolinite-dickite mixture can be proven by the following characteristics of the OH-stretching IR bands (Beaufort *et al.*, 1998): (1) the progressive shift of ν_1 from 3695 cm^{-1} to 3710 cm^{-1} accompanied decreasing intensity and band broadening; (2) the progressive disappearance of ν_2 at 3668 cm^{-1}, a slight shift to 3655 cm^{-1} of the band at 3652 cm^{-1}, and a slight shift to 3622 cm^{-1} of the band at 3620 cm^{-1} .

Instrumentation

Infrared radiation from a FTIR spectrometer was transmitted to a microscope with IR detectors, allowing FTIR analysis in parallel with observations in microscopy. This offers the unique advantage over classical FTIR techniques of allowing *in situ* measurements.

The IR spectra were recorded in petrographic thin sections using an IR source and a Cesium Iodide (CsI) beamsplitter from a Nicolet™ 6700 FTIR spectrometer (Waltham, Massachusetts, USA). The spectrometer was coupled with a Thermo Scientific Nicolet™ Continuum FTIR microscope equipped with a Mercury Cadmium Telluride (MCT) detector cooled with liquid nitrogen. Analyses were collected in transmission mode in the middle infrared (MIR) domain between 4000 and 400 cm^{-1}. The IR beam from the spectrometer was transmitted to the microscope and was shaped by passing through a mask made of adjustable slits. The shaped IR beam was then passed through samples and the transmitted radiation was collected and concentrated with a semi-spherical condenser before passing to the detector. The IR beam was shaped by the mask slits into a square with side lengths of 15–50 μm. Depending on the IR beam size, each spectrum consisted of 32 to 800 scans with a resolution of 4 cm^{-1}. A scan consisted of one back and forth motion of the mobile mirror in the

interferometer, which reflects the IR beam to the beamsplitter. The time needed for one scan depends on mirror velocity and the resolution required.

The optical microscope was equipped with an Olympus system. The magnification factor selected for spectra acquisitions was $\times 320$.

Data were sent to the computer and treated using *OMNIC*™ software with *Atlμs* add-on for mapping provided by Thermo Scientific.

The microscope was equipped with a motorized stage which permitted control of both the position and the movement of the thin section in a digitalized X-Y plane with an accuracy of 1 μm. For mapping applications, the motorized stage was used to perform step-by-step acquisition of IR spectra over a selected area. The motorized stage was also programmed for a regular translation to a point set as the background to regularly refresh the background conditions.

Reference transmission FTIR spectra were recorded with 4 cm^{-1} resolution and 100 scan accumulation using KBr sample pellets on a Nicolet 760 FTIR spectrometer equipped with a KBr beamsplitter and DTGS-KBr IR detector.

RESULTS AND DISCUSSION

Effect of sample preparation

The use of IRMS to identify minerals in thin sections is limited in the following ways: (1) the epoxy resin (araldite 2020) which sticks the sample to the glass slide and the resin which impregnates the porous network induces strong absorption bands between 2800 and 3000 cm^{-1} and a broad band at 3400 cm^{-1} (Figure 1a,b). (2) The glass substratum of the thin sections induces strong Si−O absorption which saturates the signal below 2200 cm^{-1} (Figure 1c). As a consequence, IR measurements are available in limited spectral windows, especially in the 3500−4000 cm^{-1} range. This limited range remains of particular interest because it corresponds to the hydroxyl-stretching band region of most clay minerals. (3) Effect of beam size and acquisition parameters on spectrum statistics.

Because IRMS maps of large areas or the use of a small beam size requires the accumulation of numerous scans, the best instrument parameters must be determined for each beam size to optimize spectral quality and minimize data-acquisition time.

To optimize the acquisition conditions for mapping, the effect of the number of scans stacked for a single-point analysis was first studied. An area on the thin section where dickite occurred was selected to better assess the influence of the parameters. The area was selected because no mixing with other minerals was detected in the SEM or FTIR studies.

Spectra recorded after the collection of 100 scans were selected for mapping with a 50 μm × 50 μm window. One hundred scans was a good compromise between spectrum quality and acquisition time as OH-stretching bands of dickite were identified unambiguously and well resolved. For a 25 μm × 25 μm IR beam, the definition of the bands decreased noticeably compared with 50 μm × 50 μm under the same conditions. At least 200 scans were necessary to obtain a well resolved 3710 cm^{-1} band, with a loss of resolution for the bands at 3650 and 3620 cm^{-1}. For a 15 μm × 15 μm window, the smallest window used in this study, the resultant spectra presented incoherent points in absorbance, *i.e.* an oversaturation of the 3620 cm^{-1} band, and

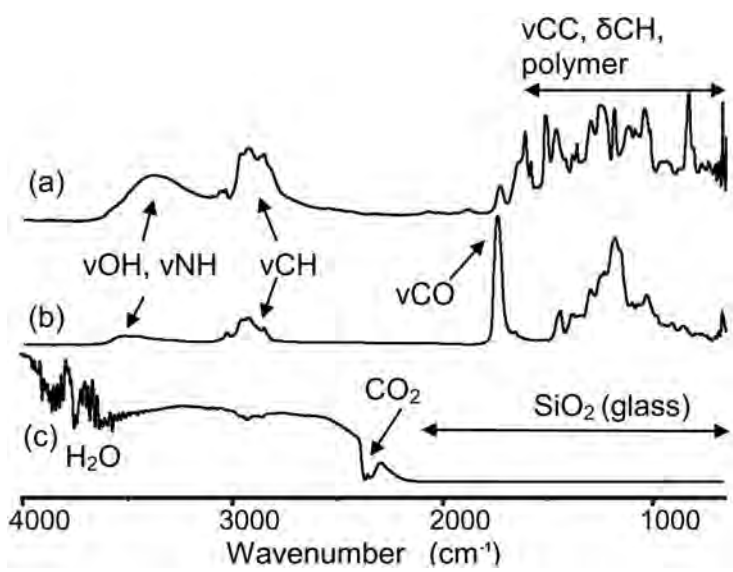

Figure 1. Single-point IR spectra (50 μm × 50 μm beam): (a) epoxy resin used to stick the rock sample on glass slides; (b) epoxy resin used to perform impregnation of porous rock samples; (c) single-channel measurement through air (a glass slide was used as the substratum for thin sections and resin).

noise-damaged band shapes. At least 800 scans were necessary to get definition good enough for the high wavenumber band near 3710 cm^{-1} for mapping with a 15 μm × 15 μm window. Decreasing the beam size produced a non-linear relationship between spectrum quality and number of scans. The 15 μm × 15 μm beam covered 9% of the surface analyzed with the 50 μm × 50 μm beam (225 and 2500 μm^2, respectively), and 800 scans for the small beam was not enough to reach the same quality as 32 scans for the larger beam (spectra from the 50 μm × 50 μm beam and 32 scans displayed no abnormal points). In order to preserve the same signal to noise ratio, the number of scans for each spectrum needed to be increased exponentially when decreasing the beam size.

Mapping parameters and conditions

The parameters used for mapping acquisition depended on the distance between two successive acquisitions in both the X and Y directions. When an overlap of the analysis windows was selected, the step size used did not exceed 50% of the window size, in order to guarantee an homogeneous covering of the area. The spectra were then processed in order to localize the kaolin polytypes on the map on the basis of the study of the integrated area of specific OH-stretching bands and use of Principal Component Analysis (PCA) as detailed below.

The OH-stretching bands of kaolinite and dickite (3695 and 3710 cm^{-1}, respectively) were used for probing kaolin polytypes in the scanned areas (Figure 3b) because the OH-stretching bands of kaolin minerals occurring at lower wavenumbers were usually overlapped by those of other clay minerals such as micas and chlorite (Figure 2). From an SEM image (Figure 3a), the overlap can be explained by the close contact between the hydroxylated minerals. In such a mapping method, the grayscale level of each pixel of the digital images represented the integrated intensity (*i.e.* area) of bands between 3680 and 3720 cm^{-1} and was proportional to the amount of kaolin minerals contained in the material analyzed (Figure 3c). Smoothing of the raw map was achieved using linear interpolation (Figure 3d). The color scale represented the variation of the integrated intensities from the maximum value (red) and minimum value (blue) calculated. Because parameters were changing from one map to another (beam size, overlap...), integrated intensities also varied. Then a different scale was attributed to each map.

However, in these conditions, direct intensity measurements of absorbance were difficult because of overlapping bands associated with each kaolin polytype (Figure 2) and to unusual intensities of the kaolinite ν_1 bands (Figure 4). Spectra measured from aggregates of small particles were as expected. Spectra with unusual relative intensities of the OH-stretching bands compared to reference kaolinite were specifically recorded for vermicular kaolinite. Acquisition of such an unusual intensity for the kaolinite (particularly ν_1) OH-stretching band has been noted for large vermicular kaolinite from

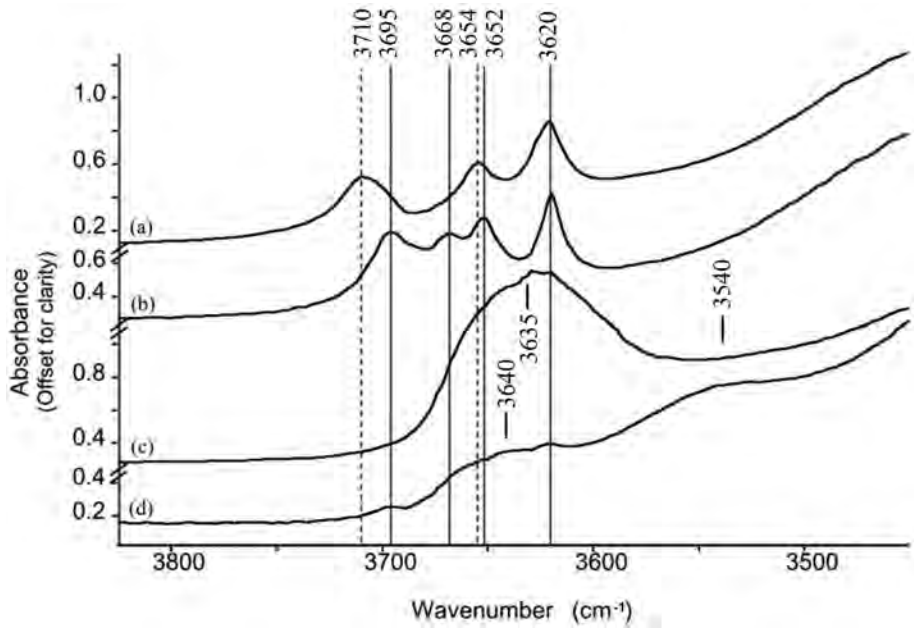

Figure 2. IR spectra in the OH-stretching bands region of phyllosilicates analyzed in the specimen, collected in transmission mode with a 50 μm × 50 μm spot and 100 scans. (a) Dickite, bands at 3710, 3654, and 3621 cm^{-1} (dotted lines); (b) kaolinite, bands at 3695, 3668, 3652, and 3620 cm^{-1} (solid lines); (c) micas, large and intense band centered at 3635 cm^{-1}; (d) chlorite, large bands centered at 3540 and 3640 cm^{-1}, and kaolinite, shoulder at 3695 cm^{-1}. Solid lines represent kaolinite band positions; dotted lines, dickite band positions.

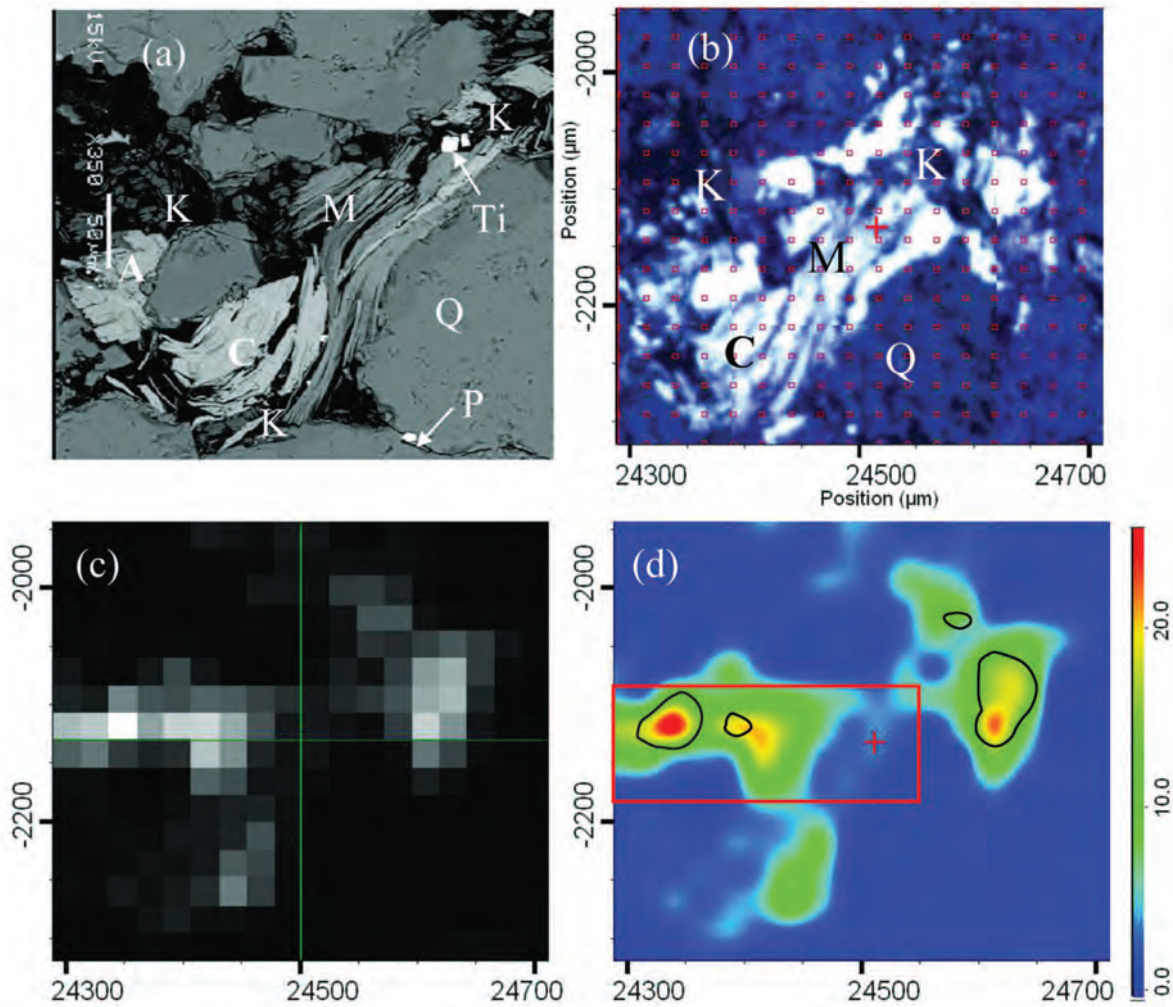

Figure 3. (a) Backscattered electron image. Chemical analysis indicates kaolin minerals (K), mica (M), chlorite (C), ankerite (A), anatase (Ti), pyrite (P), and quartz (Q); (b) optical image of the area of interest from the FTIR microscope digital camera. (c) Map of kaolin minerals, Ib (Table 1) (area shown in parts a and b, 50 µm × 50 µm IR beam and 25 µm step value). Pixels 25 µm × 25 µm, grayscale representing integrated intensity of bands between 3680 and 3720 cm^{-1}. (d) Smoothed map (linear interpolation) of kaolin minerals, with scale of integrated intensities of bands between 3680 and 3720 cm^{-1}. Black contour lines represent dickite-rich areas.

lateritic soils by IRMS (Beauvais and Bertaux, 2002). The unusual relative intensities were interpreted as being due to the large size of vermicular kaolinite giving rise to a very large number of OH vibrators in similar orientations. This constitutes a severe limitation to any quantitative estimation of the respective amounts of kaolinite and dickite from IRMS spectra on textured minerals.

Kaolinite and dickite were distinguished using multispectral Principal Component Analysis (PCA). As described previously, only the bands in the 3690–3720 cm^{-1} range can be used for kaolin minerals characterization (no overlapping with OH-stretching bands of other hydroxylated minerals). As *Atlµs* allows the user to select one or several wavenumber ranges with which the PCA will be done, the multispectral PCA was not applied on the whole MIR range but only on a reduced domain, from 3690 to 3720 cm^{-1}. In this range, *Atlµs* was able to detect the principal components of the spectra, *i.e.* the wavenumber range for which the variance of the absorbance through the whole series of spectra was greatest. Principal components were represented as theoretical bands which were compared to experimental spectra. The degree of correlation between the theoretical bands and the spectra was then used to create a map. The software was used to find the first five principal components. A band close to kaolinite ν_1 was found as the first principal component which was evaluated for correlation with the absorbance of the spectra. The map obtained from the analysis of this first component did not have mineralogical significance; sites with kaolinite or dickite could not be differentiated and almost all sites with OH-stretching absorbance were enhanced. The second principal component found

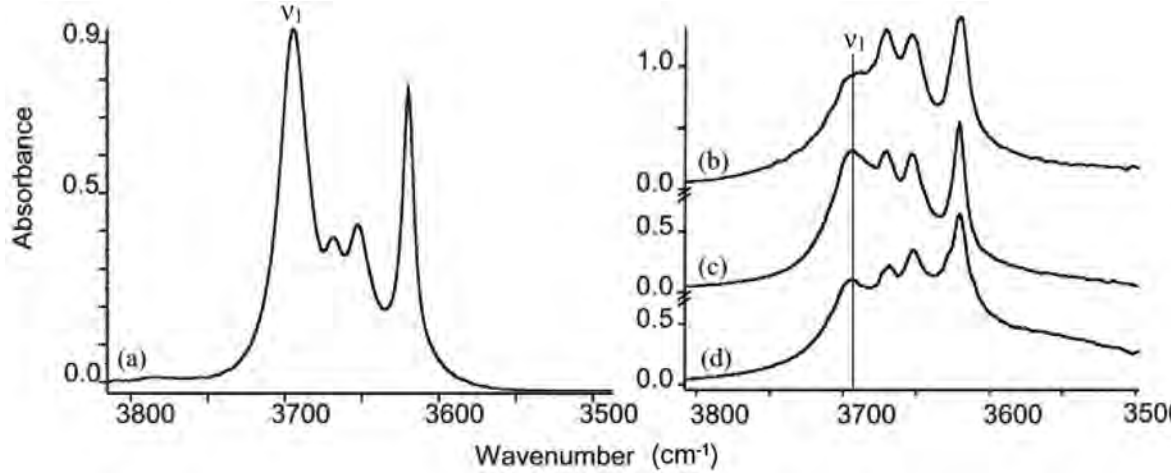

Figure 4. IR spectra of kaolin minerals in the OH-stretching bands region. (a) Kaolinite KGa-1 in KBr pellet; (b, c, d) collected in transmission mode through a 50 µm × 50 µm spot and 100 scans from several locations.

corresponded to the dickite high-wavenumber OH-stretching band. The degree of contribution of the principal component 2 in the recorded spectra was displayed using grayscale on a surface map (Figures 5a, 6c), which gave the locations of the dickite-rich sites. Smoothing of these maps was achieved by using linear interpolation and displayed as color maps (Figures 5b, 6d), using red for spectra with large contributions and blue for spectra with small contributions of the principal component 2. In order to locate the dickite-rich sites on the kaolin minerals maps, a threshold of the dickite maps was created and the contours of the dickite-rich sites displayed as black contour lines on kaolin minerals maps (Figures 3d, 6b). The other principal components after the second were of no mineralogical interest; differentiation between minerals and noise was not achieved.

The IR detector stability had to be monitored over a long period because a mineral map can take several hours to acquire (Table 1). After 16 h of analysis, no drift of the motorized stage and no shift of the condenser alignment were seen. The stability of the detector was monitored, measuring the intensity of the 3710 cm^{-1} IR band of a dickite specimen every 30 min for 11 h. After ~5 h, the intensity of the IR spectrum decreased slightly with increasing time according to a first order equation. However, the loss of intensity measured after 11 h (<5%) was insignificant compared to the intensity values recorded during the acquisition of the maps (Figures 3, 5, 6), and can be ignored for qualitative analysis. If long-time acquisitions are needed, a correction of 0.6%/h can be applied in order to compensate for the intensity loss after 5 h.

Application of FTIR mapping

The results of this methodological work indicate that IRMS can be used to study petrographic thin sections of

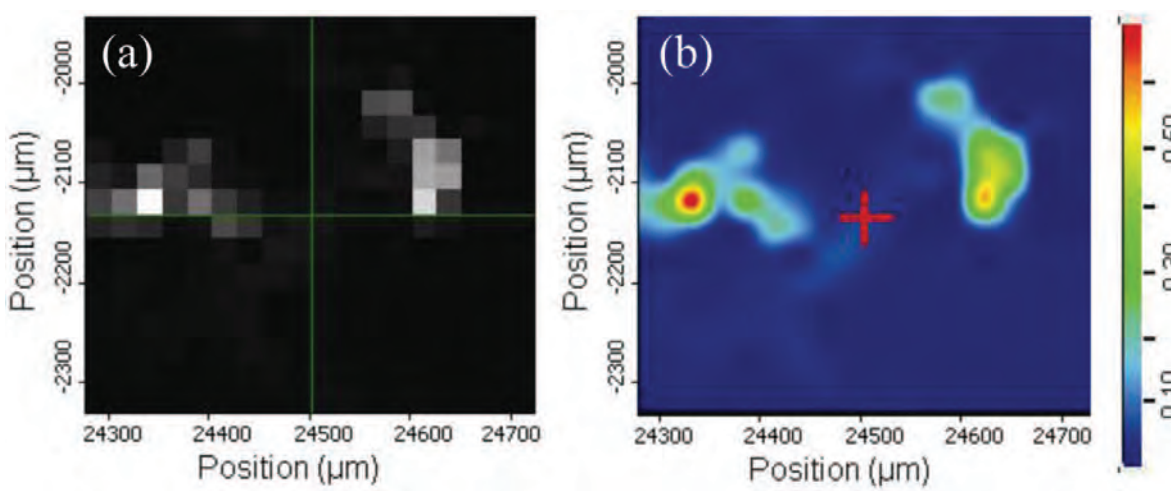

Figure 5. (a, b) Dickite map obtained after PCA applied to map Ib (part c, Figure 6). (a) Dickite map with 25 µm × 25 µm pixels; (b) smoothed map of dickite with color scale.

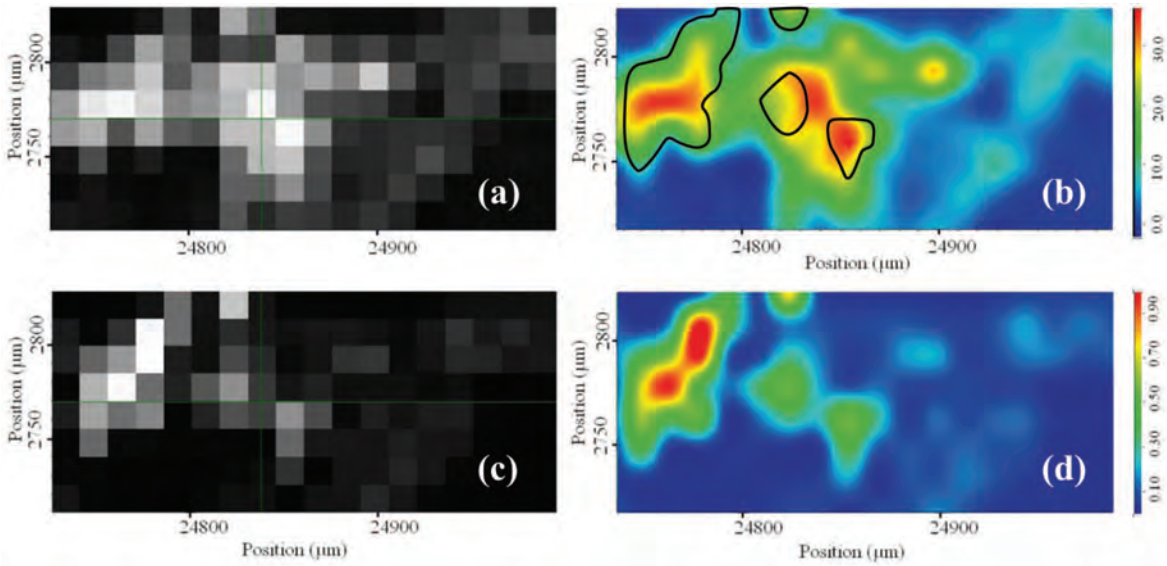

Figure 6. (a, b) Kaolin minerals map III (Table 1). (c, d) Dickite maps. (a) Area X: 24250 to 24550 µm; Y: −2175 to −2275 µm of Figure 3. 15 µm × 15 µm IR beam and 15 µm step value. 15 µm × 15 µm pixels grayscale representing integrated intensities, *i.e.* area, of bands between 3680 and 3720 cm^{-1}. (b) Smoothed map (linear interpolation) of kaolin minerals, with scale of integrated intensities of bands between 3680 and 3720 cm^{-1}. Black contour lines represent dickite-rich areas. (c) Dickite map with 15 µm × 15 µm pixels. (d) Smoothed map of dickite with color scale.

sandstone which suffered kaolinite-to-dickite transition during their burial diagenesis. The IRMS permits (1) the localization of the two kaolin polytypes within the clay cement and (2) the mapping of dickite distribution at the pore scale.

Localizing kaolin minerals in thin section. The main contribution of the IRMS analysis of kaolin minerals in thin section is its ability to characterize each polytype *in situ* in the sandstones (even in the case of small amounts). This is well illustrated in Figure 7. In a previous study, the clay fraction of this sample was extracted and studied by FTIR using KBr pressed pellets. From FTIR spectra of mechanical mixtures of kaolinite and dickite, the dickite/kaolinite ratio was estimated to be 85/15 (Cassagnabère, 1998). Pure kaolinite spectra (Figure 7a) were distinguished from pure dickite (Figure 7d) and mixing of the two kaolin minerals (Figure 7b,c) using IRMS at several locations on the thin section. According to the size of the IR beam used (from 50 µm × 50 µm to 15 µm × 15 µm) and to the SEM observations indicating a <10 µm average size for the crystals of kaolin minerals, most of the single-point analyses collected by IRMS had to be considered as representative of particle aggregates rather than individual particles. The fact that IR spectra of pure kaolinite and/or dickite (Figure 7a,d) had been recorded among spectra corresponding to mixing of the two polytypes of kaolin minerals (Figure 7b,c) indicated that segregations of each polytype exist at a scale which is broadly similar to that of the petrographic observations performed with optical microscopy in thin sections. In other words, the IRMS analysis can be considered as a useful method to complete the petrographic study of thin sections in characterizing the kaolin cement at a relatively local scale (<50 µm × 50 µm). Mapping the kaolin cements with IRMS would allow the easy selection of areas of interest for further *in situ* investigations of each polytype by microprobe analysis or LA-ICP-MS, for instance.

Table 1. Summary of the parameters selected to map kaolin minerals in this study.

Map number	Map dimension (µm)	Beam size (µm)	Scans	Time/step (s)	Step size (µm)	Number of spectra	Total time (h)
Ia	450 × 400	50/50	100	41.83	50/50	90	1.0
Ib	425 × 375	50/50	100	41.83	25/25	288	3.3
Ic	450 × 400	50/50	100	41.83	15/15	868	10.1
II	400 × 350	25/25	200	83.67	25/25	255	5.9
III	260 × 100	15/15	800	334.68	15/15	140	13.5

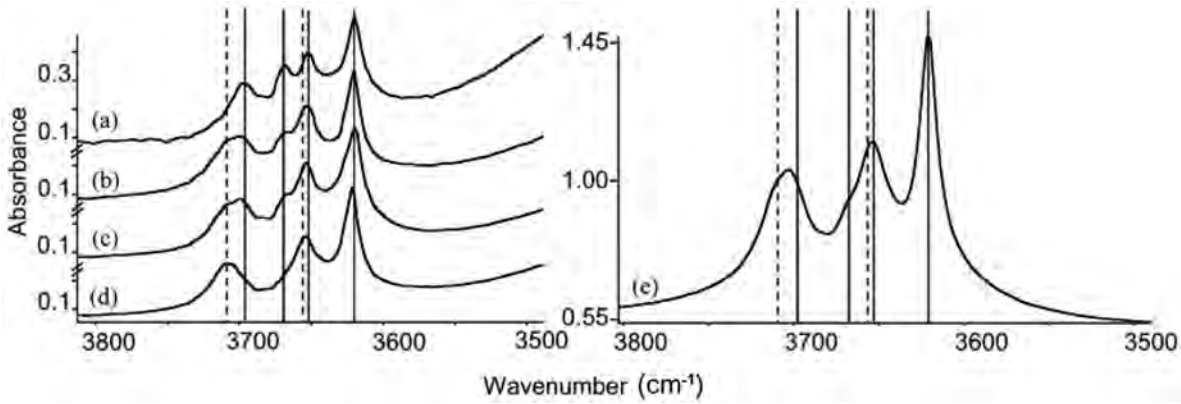

Figure 7. IR spectra of kaolin minerals in the OH-stretching bands region: (a–d) collected in transmission mode through a 50 μm × 50 μm spot and with 100 scans. (e) Extracted clay fraction collected in transmission mode through KBr pellets (Beaufort *et al.*, 1998) (85% dickite and 15% kaolinite, Cassagnabère (1998)). Solid lines represent kaolinite band positions; dotted lines, dickite band positions.

Mapping kaolin minerals. With acquisition time varying with both the window size and the step size value, optimizing the setting parameters in order to minimize acquisition time was crucial. Several maps were created in order to measure the effect of the window size and the step size on the quality of the map (Table 1).

A first map of kaolin minerals (Ib Table 1, Figure 3) was obtained from a thin section in which previous SEM analyses indicated that kaolin minerals, phengitic micas, and Fe-rich chlorite coexist with quartz, ankerite, titanium oxide, and pyrite. This map, in which the size of each pixel was 25 μm × 25 μm (50 μm × 50 μm IR beam with a step size value of 25 μm), confirmed that IRMS allows the identification of kaolin minerals, even in a complex mineral matrix which includes several types of phyllosilicates, with IR absorption in the OH-stretching region (as shown in Figure 2).

Decreasing the step size led to improved detection accuracy of mineralogical variations and a better resolution of the spatial distribution of the minerals investigated (Ia to Ic, Table 1, Figure 8). Map Ia (Figure 8a) was composed of pixels 50 μm × 50 μm in size for a step size value of 50 μm in both the X and Y directions. By decreasing the step value by half in each direction (25 μm) an overlap was created between the areas analyzed and the number of pixels was increased by four (Ib Table 1). The information gain from maps Ia to Ib was significant (Figure 8a,b). In map Ib, strong contrasts were observed within the area represented by one pixel in Ia, showing that the differentiation of dickite within the kaolin minerals was more accurate in Ib than in Ia. The maps III and Ic (Figures 6, 8c), both with the same pixel size 15 μm × 15 μm, displayed a better spatial resolution than the maps Ia and Ib (Figure 8a,b).

If a comparison is made between maps III and Ic (Figures 6, 8c), in which the pixel size was the same but the beam size was different, the quality of the information obtained is notably better in map III (Figure 6). In map Ic (Figure 8c) each pixel represented an average value obtained from several spectra (window size of 50 μm × 50 μm but a step size of 15 μm). In map III (Figure 6) each pixel represented only one spectrum recorded with a 15 μm × 15 μm window size (no overlap of the acquisition windows). The same comparison can be made between the maps Ib (50 μm × 50 μm beam, 25 μm step size) and II (25 μm × 25 μm window size, 25 μm step size) (Figure 8b,c). The spatial resolution and the level of detail were the same, with 25 μm × 25 μm pixels, but the nature of the information was different with an average of several measurements by pixel for map Ib and one spectrum for one pixel for map II.

SUMMARY AND CONCLUSIONS

Infrared microspectroscopy is a convenient method for the characterization of kaolin minerals in sandstone and can be used to study kaolin minerals in their petrographic environment. The method is particularly useful for investigating the petrographic relationships between kaolinite and dickite. Such relationships cannot be examined directly in thin section by other classical methods, such as XRD, microprobe analysis, or SEM observation.

(1) Several authors have proposed that dickite can be distinguished from kaolinite based on crystal morphology (blocky dickite *vs.* vermicular kaolinite). However, IRMS analysis of kaolin minerals with blocky habit indicates that this interpretation is questionable. Indeed, blocky kaolin minerals in a sandstone were characterized as kaolinite using IRMS (Figure 9). Blocky kaolinite in sandstone had previously been identified using EBSD (Kogure *et al.*, 2005), which requires separation and extraction of single crystals before identification. Such methods are not adapted to petrographic examination of thin sections of rocks.

(2) IRMS can be used to map kaolinite and dickite distribution in thin sections at the petrographic scale.

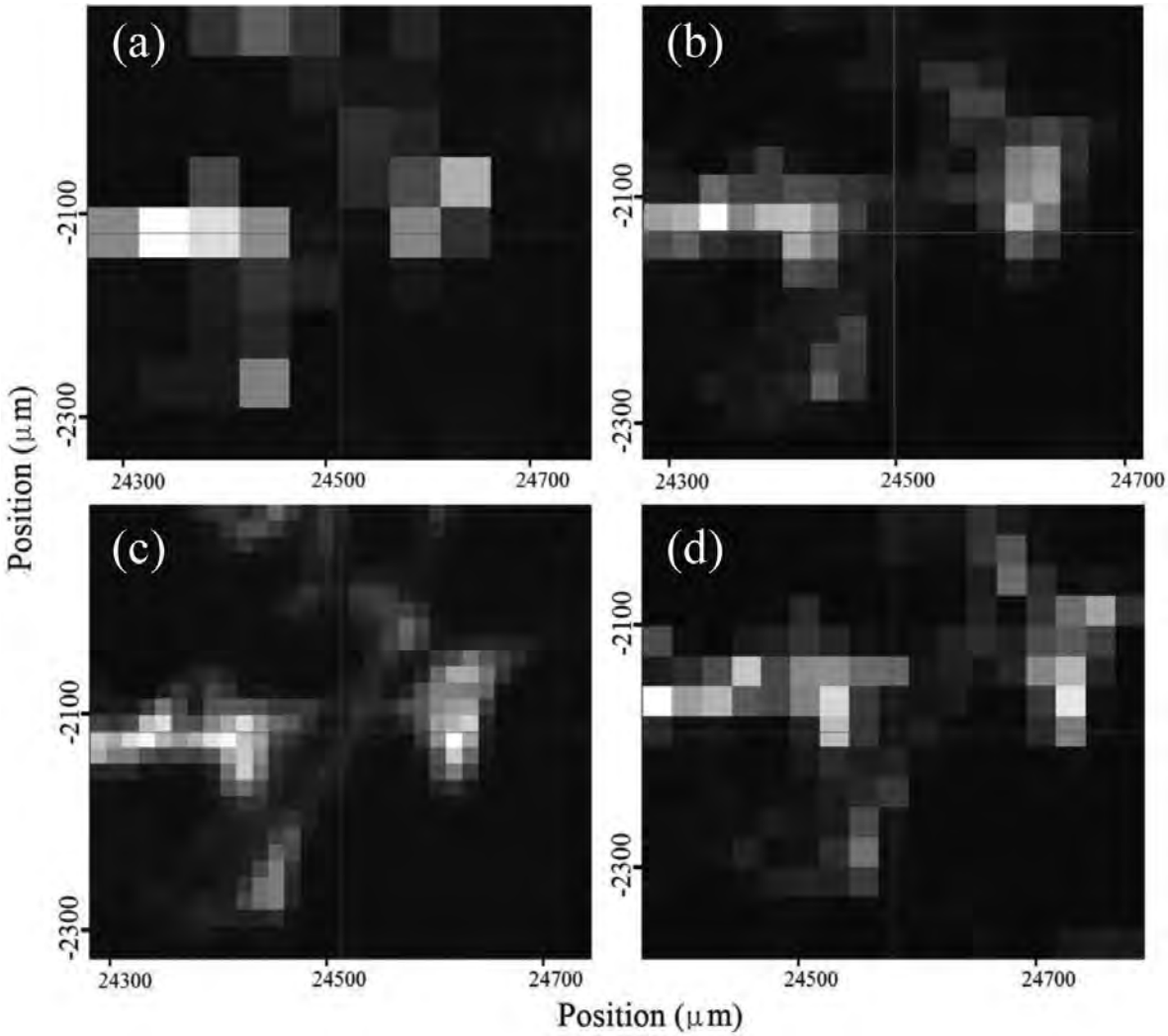

Figure 8. Kaolin map: (a) Map Ia (Table 1), 50 μm × 50 μm IR beam and 50 μm step value in X and Y directions; (b) Map Ib (Table 1), 50 μm × 50 μm IR beam and 25 μm value in X and Y directions; (c) Map Ic (Table 1), 50 μm × 50 μm IR beam and 15 μm step value in X and Y directions; and (d) Map II (Table 1), 25 μm × 25 μm IR beam and 25 μm step value in X and Y directions.

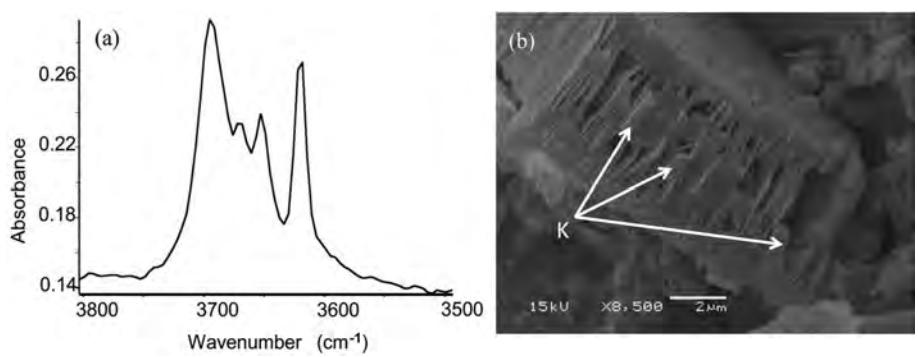

Figure 9. (a) Scale expansion of the OH-stretching region from sample (25_15-1 3006m) collected in transmission mode through a 50 μm × 50 μm spot and with 100 scans. (b) SEM image of intergrowth of kaolin minerals with a blocky habit (k).

Spatial resolution is limited by the IR window size (15 μm × 15 μm). However, IRMS is particularly well adapted to mapping the distribution of the relatively coarse-grained (up to 30 or 40 μm) kaolinite and dickite formed during sandstone digenesis. Characterization and mapping of other hydroxylated minerals, such as chlorite and micas, can also be carried out using IRMS. However, the spatial resolution of IRMS is minor compared to that of SEM.

(3) Integration of IRMS into a series of petrographic analyses (optical microscope, SEM...) requires the use of thin sections, which have drawbacks, such as glass slide and embedding resin IR interferences, but these interferences can be addressed using self-supporting thin sections (thin sections separated from the glass slide after polishing) and by the use of specific embedding resins.

(4) IRMS can also be used for thin sections of finer-grained kaolin polytypes in other natural environments, such as pedogenic or hydrothermal systems. For example, IRMS has been used to characterize disordered kaolinite in thin sections of soils and to identify structural Fe in the 3598 cm^{-1} absorption band of kaolinite (Beauvais and Bertaux, 2002).

ACKNOWLEDGMENTS

The authors are grateful to the Editor in Chief, Associate Editor, and two anonymous reviewers for their constructive contributions, helping to improve the quality of this paper.

REFERENCES

Balan, E., Saitta, A.M., Mauri, F., and Calas, G. (2001) First-principles modeling of the infrared spectrum of kaolinite. *American Mineralogist*, **86**, 1321–1330.

Balan, E., Lazzeri, M., Saitta, A.M., Allard, T., Fuchs, Y., and Mauri, F. (2005) First-principles study of OH-stretching modes in kaolinite, dickite, and nacrite. *American Mineralogist*, **90**, 50–60.

Balan, E., Delattre, S., Guillaumet, M., and Salje, E.K.H. (2010) Low-temperature infrared spectroscopic study of OH-stretching modes in kaolinite and dickite. *American Mineralogist*, **95**, 1257–1266.

Beaufort, D., Cassagnabere, A., Petit, S., Lanson, B., Berger, G., Lacharpagne, J.C., and Johansen, H. (1998) Kaolinite-to-dickite reaction in sandstone reservoirs. *Clay Minerals*, **33**, 297–316.

Beauvais, A. and Bertaux, J. (2002) In situ characterization and differenciation of kaolinites in lateritic weathering profiles using infrared microspectroscopy. *Clays and Clay Minerals*, **50**, 314–330.

Bish, D.L. (1993) Rietveld refinement of the kaolinite structure at 1.5 K. *Clays and Clay Minerals*, **41**, 738–744.

Brindley, G.W., Kao, C.-C., Harrison, J.L., Lipsicas, M., and Raythatha, R. (1986) Relation between structural disorder and other characteristics of kaolinites and dickites. *Clays and Clay Minerals*, **34**, 239–249.

Cassagnabère, A. (1998) Characterization and interpretation of kaolinite-to-dickite transition in Froy and Rind hydrocarbons reservoirs (North Sea, Norway). PhD thesis, University of Poitiers, France.

De Andrade, V., Vidal, O., Lewin, E., O'Brien, P., and Agard, P. (2006) Quantification of electron microprobe compositional maps of rock thin sections: an optimized method and examples. *Journal of Metamorphic Geology*, **24**, 655–668.

Ehrenberg, S.N., Aagaard, P., Wilson, M.J., Fraser, A.R., and Duthie, D.M.L. (1993) Depth-dependent transformation of kaolinite to dickite in sandstones of the Norwegian continental shelf. *Clay Minerals*, **28**, 325–352.

Farmer, V.C. (1974) *The Infrared Spectra of Minerals*. Monograph **4**, The Mineralogical Society, London.

Farmer, V.C. (1998) Differing effects of particle size and shape in the infrared and Raman spectra of kaolinite. *Clay Minerals*, **33**, 601–604.

Farmer, V.C. and Russell, J.D. (1964) The infra-red spectra of layer silicates. *Spectrochimica Acta*, **20**, 1149–1173.

Frost, R.L. and van der Gaast, S.J. (1997) Kaolinite hydroxyls; a Raman microscopy study. *Clay Minerals*, **32**, 471–484.

Frost, R.L., Tran, T.H., and Kristof, J. (1997) The structure of an intercalated ordered kaolinite; a Raman microscopy study. *Clay Minerals*, **32**, 587–596.

Johnston, C.T., Agnew, S.F., and Bish, D.L. (1990) Polarized single-crystal Fourier-transform infrared microscopy of Ouray dickite and Keokuk kaolinite. *Clays and Clay Minerals*, **38**, 573–583.

Johnston, C.T., Kogel, J.E., Bish, D.L., Kogure, T., and Murray, H.H. (2008) Low-temperature FTIR study of kaolin-group minerals. *Clays and Clay Minerals*, **56**, 470–485.

Kameda, J., Saruwatari, K., Beaufort, D., and Kogure, T. (2008) Textures and polytypes in vermiform kaolins diagenetically formed in a sandstone reservoir: a FIB-TEM investigation. *European Journal of Mineralogy*, **20**, 199–204.

Kogure, T., Inoue, A., and Beaufort, D. (2005) Polytype and morphology analyses of kaolins minerals by electron back-scattered diffraction. *Clays and Clay Minerals*, **53**, 201–210.

Lanson, B., Beaufort, D., Berger, G., Baradat, J., and Lacharpagne, J.-C. (1996) Illitization of diagenetic kaolinite-to-dickite conversion series; late-stage diagenesis of the Lower Permian Rotliegend Sandstone reservoir, offshore of the Netherlands. *Journal of Sedimentary Research*, **66**, 501–518.

Lanson, B., Beaufort, D., Berger, G., Bauer, A., Cassagnabere, A., and Meunier, A. (2002) Authigenic kaolin and illitic minerals during burial diagenesis of sandstones: a review. *Clay Minerals*, **37**, 1–22.

Ledoux, R.L. and White, J.L. (1964) Infrared study of the OH groups in expanded kaolinite. *Science*, **143**, 244–246.

Madejová, J., Balan, E., and Petit, S. (2010) Application of vibrational spectroscopy to the characterization of phyllosilicates and other industrial minerals. *Advances in the Characterization of Industrial Minerals* (G.E. Christidis, editor). EMU Notes in Mineralogy, **9**, European Mineralogical Union and the Mineralogical Society of Great Britain and Ireland, London.

McAulay, G.E., Burley, S.D., Fallick, A.E., and Kusznir, N.J. (1994) Palaeohydrodynamic fluid flow regimes during diagenesis of the Brent group in the Hutton-NW Hutton reservoirs; constraints from oxygen isotope studies of authigenic kaolin and reverse flexural modelling. *Clay Minerals*, **29**, 609–626.

Munoz, M., de Andrade, V., Vidal, O., Lewin, E., Pascarelli, S., and Susini, J. (2006) Redox and speciation micromapping using dispersive X-ray absorption spectroscopy; application to iron in chlorite mineral of a metamorphic rock thin section. *Geochemistry, Geophysics, Geosystems – G^3*.**7**, doi: 10.1029/2006GC001381.

Osborne, M., Haszeldine, R.S., and Fallick, A.E. (1994) Variation in kaolinite morphology with growth temperature

in isotopically mixed pore-fluids, Brent Group, UK North Sea. *Clay Minerals*, **29**, 591–608.

Prêt, D., Sammartino, S., Beaufort, D., Meunier, A., Fialin, M., and Michot, L.J. (2010a) A new method for quantitative petrography based on image processing of chemical element maps: Part I. Mineral mapping applied to compacted bentonites. *American Mineralogist*, **95**, 1379–1388.

Prêt, D., Sammartino, S., Beaufort, D., Fialin, M., Sardini, P., Cosenza, P., and Meunier, A. (2010b) A new method for quantitative petrography based on image processing of chemical element maps: Part II. Semi-quantitative porosity maps superimposed on mineral maps. *American Mineralogist*, **95**, 1389–1398.

Prost, R., Damême, A., Huard, E., and Driard, J. (1987) Infrared study of structural OH in kaolinite, dickite, and nacrite at 300 to 5 K. (L.G. Schultz, H. van Olphen, and F.A. Mumpton, editors). International Clay Conference, Denver, 1985. The Clay Minerals Society, Bloomington, Indiana, USA, pp. 17–23.

Prost, R., Dameme, A., Huard, E., Driard, J., and Leydecker, J.P. (1989) Infrared study of structural OH in kaolinite, dickite, nacrite, and poorly crystalline kaolinite at 5 to 600 K. *Clays and Clay Minerals*, **37**, 464–468.

Rintoul, L. and Fredericks, P.M. (1995) Infrared microspectroscopy of bauxitic pisoliths. *Applied Spectroscopy*, **49**, 1608–1616.

Tokiwai, K. and Nakashima, S. (2010) Integral molar absorptivities of OH in muscovite at 20 to 650ºC by in-situ high-temperature IR microspectroscopy. *American Mineralogist*, **95**, 1052–1059.

(*Received 28 August 2012; revised 12 March 2013; Ms. 707; AE: H. He*)

Clays and Clay Minerals, Vol. 61, No. 2, 152–164, 2013.

ANISOTROPIC SURFACE CHARGING OF CHLORITE SURFACES

XIHUI YIN[1], LUJIE YAN[2], JING LIU[1], ZHENGHE XU[2], AND JAN D. MILLER[1,*]

[1] Department of Metallurgical Engineering, College of Mines and Earth Sciences, University of Utah, 135 South 1460 East, Room 412, Salt Lake City, UT 84112-0114, USA
[2] Department of Chemical and Materials Engineering, University of Alberta, Room 280C, Chemical and Materials Engineering Building, Edmonton, Alberta, AB T6G 2G6, Canada

Abstract—Chlorite is a layered silicate mineral group of importance in geology, agriculture, and in the processing of mineral resources. A more detailed analysis of the surface charge of chlorite minerals is important in order to improve our fundamental understanding of such particle structures and their behavior in suspension. In this study, the anisotropic surface charging of chlorite has been established using Atomic Force Microscopy surface-force measurements with a silicon nitride tip. The surface-charge densities and surface potentials at the chlorite basal-plane surfaces and edge surface were obtained by fitting force curves with the Derjaguin-Landau-Verwey-Overbeek theoretical model. The results show that at pH 5.6, 8.0, and 9.0 the chlorite mica-like face is negatively charged with the isoelectric point (IEP) less than pH 5.6. In contrast, the chlorite brucite-like face is positively charged in this pH range and the IEP is greater than pH 9.0. The surface charging of the chlorite edge surface was found to be pH-dependent with the IEP occurring at pH 8.5, which is slightly greater than the edge surfaces of talc and muscovite due to the larger content of magnesium hydroxide at the chlorite edge surface. Findings from the present research are expected to provide a fundamental foundation for the analysis of industrial requirements, *e.g.* collector adsorption, slime coating, and particle interactions in the area of mineral-processing technology.

Key Words—Anisotropic Surface Characteristics, Atomic Force Microscopy, Basal Plane, Chlorite, DLVO Model, Edge Surface, Electrophoresis, Flotation, Surface Charge, Surface Potential.

INTRODUCTION

The group of phyllosilicates, or layered silicates, including serpentine, mica, chlorite, and the clay minerals, is very important in geology, agriculture, and mineral processing (Murray and Kogel, 2005; Harvey and Murray, 1997; Murray, 1991). Some of the phyllosilicates in a pure state are valuable in a wide range of applications including in ceramics, in the manufacture of paper (as a coating, pigment, and filler), in inks and paints (as an extender), in medicine, and as an additive in the production of rubber and polymers (Harvey and Murray, 1997; Murray, 2000). In other circumstances, however, the phyllosilicates, such as kaolinite, illite, and talc, may cause problems in making efficient particle separations in the recovery/utilization of mineral resources and in achieving satisfactory sedimentation/consolidation for disposal of the waste (tailings) from these operations. Note that almost all the aforementioned processes and/or utilization of the phyllosilicates are affected by their crystal structure and surface properties. In this regard, the study of phyllosilicate surface chemistry is critical to the development of improved technology in many sectors of the economy.

The chlorite minerals are a major magnesia silicate group of gangue minerals found in both sulfide and non-sulfide ores. Chlorite is a 2:1:1 type phyllosilicate, consisting of a brucite-like or gibbsite-like sheet sandwiched between mica-like trilayers. The common minerals in the chlorite class include clinochlore ($(Mg_5Al)(AlSi_3)O_{10}(OH)_8$), chamosite ($(Fe_5Al)(AlSi_3)O_{10}(OH)_8$), nimite ($(Ni_5Al)(AlSi_3)O_{10}(OH)_8$), and pennantite ($(Mn, Al)_6(Al, Si)_4O_{10}(OH)_8$). The spacing, the distance between two repeating chlorite layers, is ~1.4 nm. The lattice structure of the brucite-like and mica-like layers of chlorite have been imaged using atomic force microscopy (AFM) (Vrdoljak *et al.*, 1994). When a chlorite crystal is cleaved, both a mica-like face and a brucite-like or gibbsite-like face should be exposed. The mica-like face is expected to carry a permanent negative charge, as 25% of the Si atoms are substituted by Al atoms in the tetrahedral sheet. This charge deficiency is compensated by the positively charged brucite-like or gibbsite-like sheet. Both the negatively charged mica-like layer and the positively charged brucite-like or gibbsite-like sheet contribute to the overall surface-charge density. In addition to the basal plane surfaces, the edge surface of chlorite particles may also have a different charging behavior. The edge surface of phyllosilicates is composed of broken covalent or ionic bonds which have high polarity and are easily hydrolyzed to exhibit a strong pH-dependent surface-charge density (Nalaskowski *et al.*, 2007; Fuerstenau and Pradip, 2005).

Electrophoresis is a common method for determining the zeta potential which represents the electrostatic

* E-mail address of corresponding author:
Jan.Miller@utah.edu
DOI: 10.1346/CCMN.2013.0610212

potential close to the surface at the slipping plane when the particles are moving in the aqueous solution under the influence of an electric field. The pH at which the slipping plane carries zero net charge is known as the isoelectric point (IEP). The zeta potential of chlorite has been studied by several researchers using the electrophoresis technique (Sondi and Pravdic, 1996; Sondi *et al.*, 1996, 1997; Fornasiero and Ralston, 2005). The measured IEP is in the range of pH 3 to 6, depending on different mineralogy and electrolyte conditions. Note that the zeta potential calculated from electrophoretic measurements assumes that the particles are spherical and does not take into account the platy shape and anisotropic character of phyllosilicate particles.

Mular-Roberts titration is another technique used to characterize the surface charging. In this method, the pH value of a suspension is measured at different ionic strengths. The suspension is first prepared at given pH and ionic strength; then the ionic strength is increased to yield a change in pH (Mular and Roberts, 1966). When no change in pH occurs, the pH value is determined as the point of zero salt effect (PZSE). Using the Mular-Roberts titration technique, Alvarez-Silva *et al.* (2010) determined the PZSE of chlorite as pH 4.7, compared to an electrophoretic IEP at pH < 3. Some researchers consider the titration method to be a better technique as it is not affected by the particle shape. Like the electrophoresis technique, however, the titration technique still only gives an overall surface charge density and the anisotropic surface charging characteristics of phyllosilicate particles are not defined.

Atomic force microscopy has been applied widely in the investigation of the surface properties for different minerals (Veeramasuneni *et al.*, 1996; Nalaskowski *et al.*, 2007; Assemi *et al.*, 2006; Zhao *et al.*, 2008; Yan *et al.*, 2011; Yin and Drelich, 2008; Long *et al.*, 2009; Gupta *et al.*, 2011). According to the geometry of the AFM tips, several theoretical models have been developed based on the Derjaguin-Landau-Verwey-Overbeek (DLVO) theory in which the electrostatic interaction and van der Waals interaction are considered. A common technique used for surface-force measurements is known as the colloidal probe technique in which a small particle with spherical shape is glued at the end of a tipless AFM cantilever (Nalaskowski *et al.*, 2003; Wallqvist *et al.*, 2006; Zhang *et al.*, 2007). The colloidal probe technique can greatly enhance the sensitivity of surface-force measurements. However, the spherical particles used in the measurements are usually 5−20 μm in size. Thus, obtaining a high-resolution image during the surface-force measurements is difficult. The roughness of the particle surfaces may also influence significantly the surface forces.

By using the colloidal probe technique, the surface charging property can be determined. Generally, AFM measures the diffuse-layer potential or diffuse-layer charge. The IEP is often used to describe a surface electrostatic potential of zero from AFM measurements. Although the values of IEP determined by AFM and electrophoretic mobility may not be exactly the same, they are usually very close to each other (Leroy *et al.*, 2011; Drelich and Wang, 2011). The surface-charging behaviors of the talc basal-plane surface and the edge surface were found by Nalaskowski *et al.* (2007) to be different. However, the surface roughness of their samples was still too great to acquire reliable AFM force curves and perform a detailed quantitative analysis. In another study (Zhao *et al.*, 2008), the quality of the edge surfaces was improved using a microtome cutting technique to create a smooth surface. Subsequently, the interaction forces between a silica probe particle and muscovite face and edge surfaces were measured by Zhao *et al.* (2008). Ultra-smooth (roughness <1 nm) mica and talc basal-plane and edge surfaces were prepared successfully by Yan *et al.* (2011). The anisotropic surface-charging characteristics for mica and talc basal-plane surfaces and edge surfaces have been characterized using AFM.

The present study discusses the surface charging of chlorite as a function of pH measured by electrophoresis and AFM. The IEPs for the chlorite mica-like face, brucite-like face, and edge surfaces were determined from surface force measurements using AFM. In this way, the anisotropic charging properties for chlorite were established. The present research is expected to provide a better understanding of the anisotropic surface-chemistry properties of chlorite which is significant for developing suitable flotation reagent schedules (collectors, depressant, modifiers, and pH) and improving flotation separation processes.

MATERIALS AND METHODS

Sample preparation

A high-purity chlorite crystal with natural cleavage on the (001) plane from Chester, Pennsylvania, USA, was used. X-ray diffraction (XRD) results implied that the chlorite sample is highly ordered and the basal reflections (001), (002), (003), (004), (005) of chlorite were observed. No other possible mineral contaminants were detected in the XRD pattern. X-ray photoelectron spectroscopy (XPS) analysis showed that the chlorite sample contains 7.5% Si, 4.9% Al, 9.9% Mg, and trace amounts of Na (0.2%), Fe (0.3%), Cr (0.7%), and chloride (0.2%). The XPS results suggested that the chlorite sample being studied corresponded most closely to clinochlore. A few flakes of chlorite sample were ground to <45 μm in size to measure the zeta potential using the electrophoresis method.

One thin layer of chlorite was peeled from the chlorite crystal using sticky tape. This thin layer of the chlorite crystal as well as the chlorite crystal itself were then glued on two thoroughly cleaned glass substrates. As chlorite is composed of alternating mica-like layers and brucite-like sheet structures, when a chlorite sample

is cleaved, two different faces will be exposed. By using this method, chlorite samples exposing a mica-like surface and a brucite-like surface were prepared (Figure 1). Note that the cleavage of chlorite can be random. Thus, either a mica-like layer or brucite-like sheet can be exposed at the top of the tape. After keeping the sample in a petri-dish for 24 h until the glue was completely dry, the samples were mounted on magnetic disks as the substrate for study of the charging properties of chlorite surfaces using AFM. Before measuring the surface force by AFM, the samples were dried and cleaned with high-purity nitrogen gas to remove any contaminants.

The chlorite edge surface was also prepared. A small flake of the chlorite sample was embedded in epoxy resin (Electron Microscopy Sciences, Hatfield, Pennsylvania, USA) and baked for 24 h at 60ºC. Then the sample was trimmed using a razor blade under an optical microscope to make the sample perpendicular to the cutting edge. When the chlorite edge was exposed, the sample was glued on a magnetic disk and cut using an ultramicrotome (EM UC 7, Leica Microsystems, Inc.) to obtain a smooth surface for subsequent AFM study. Before measuring the surface force by AFM, the samples were rinsed with Milli-Q water and ethanol and cleaned with high-purity nitrogen gas to remove any debris or contaminants.

Zeta-potential measurements

The zeta-potential measurements were done using the electrophoresis technique (ZetaPALS, Brookhaven Instrument Corp., New York). A chlorite suspension with a concentration of 0.05 wt.% was prepared in 1 mM KCl background electrolyte. The mobilities of chlorite particles were measured at varying pH and then converted to zeta potentials (ζ) using Smoluchowski's model as follows:

$$U = \frac{\varepsilon\zeta}{4\pi\eta} E_{\infty} \quad (1)$$

where U is the particle mobility, E_{∞} is the strength of the electric field applied, and ε and η are the dielectric constant and viscosity of the solvent, respectively. The Smoluchowski model assumes that the particles are spherical and that the surface-charge densities are uniformly distributed at the particle surfaces.

Surface-force measurements using AFM

A picoforce AFM with a Nanoscope V controller (Bruker Corporation, Santa Barbara, California, USA) was used with a PF-type scanner designed for picoforce measurements. A contact-mode silicon nitride cantilever was used to study the surface charging of chlorite. The spring constant was determined by the thermal tuning function provided in *Nanoscope V* 7.20 software and this value was used later in data analysis. The AFM images of chlorite basal planes and edge surfaces were collected before the surface force measurements were taken. The images were captured with a scan size of 5 μm and scan rate of 1 Hz. The resolution of the image is 512 points/line.

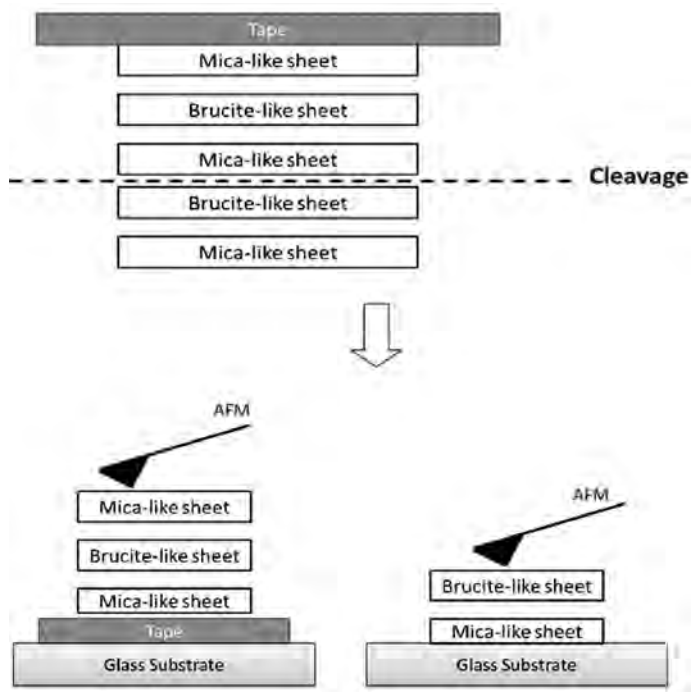

Figure 1. Schematic diagram of the preparation procedure for chlorite basal surfaces.

The surface-force measurements were conducted at the chlorite mica-like surface, the brucite-like surface, and the edge surface at five different locations in 1 mM KCl at pH 5.6, 8, and 9. At each location, five force curves were collected. All the force measurements were performed at a scan rate of 1 Hz and captured at a resolution of 512 points/measurement. *SPIP* software (Image Metrology, Lyngby, Denmark) was used to convert the deflection-distance curves to force-distance curves. Baseline correction and hysteresis correction were involved in preparation of the force curves. The force-distance curves were fitted with the theoretical DLVO model under constant surface-charge density or a constant surface-potential boundary condition. The surface charge density and the surface potential of various types of clay surfaces were obtained from fitting the force profile data to the DLVO theory.

Theoretical model

The geometry of the silicon nitride AFM tip can be approximated as being conical in shape with a spherical cap at its apex. The geometry of the system and the parameters used are shown in Figure 2. The symbols α and β are the geometrical angles for the spherical cap at the tip end and conical tip with α+β = 90º, *D* is the distance from the end of the tip to the substrate, *L* is the distance between a differential surface section of the tip and the substrate, *r* is the radius of the circle of the tip at a given vertical position, and *R* is the radius of the spherical cap at the tip end (Drelich *et al.*, 2007).

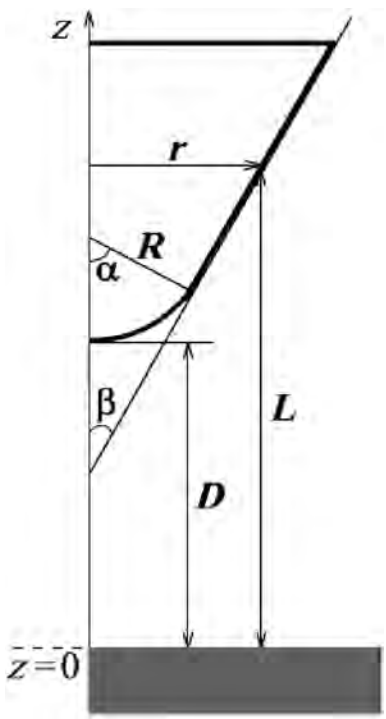

Figure 2. Geometry of the system and parameters used for theoretical DLVO calculations.

The DLVO theoretical model with this geometry was derived and discussed in the literature (Drelich *et al.*, 2007) and only the final equations are given here.

The van der Waals force between the spherical segment of the tip and flat substrate surface is given by:

$$F_{TS}^{vdw\text{-}S} = \frac{A}{6}\left[\frac{(R+D)-2L_1}{L_1^2} - \frac{R-D}{D^2}\right] \quad (2)$$

The formula describing the van der Waals force for the conical segment of the AFM tip is:

$$F_{TS}^{vdw\text{-}C} = \frac{A}{3\tan^2\alpha}\left(\frac{1.0}{L_1} + \frac{R\sin\alpha\tan\alpha - D - R(1-\cos\alpha)}{L_1^2}\right) \quad (3)$$

where $L_1 = D+R(1-\cos\alpha)$, A is the combined Hamaker constant, ε is the dielectric constant of the solution in this system, ε_0 is the permittivity of vacuum, $1/\kappa$ is the Debye length, *D* is the distance between the two surfaces, and subscripts 1 and 2 refer to the two surfaces. ($A_{water} = 3.7\times10^{-20}$ J, $A_{tip} = 1.62\times10^{-19}$ J, $A_{chlorite} = 2.33\times10^{-19}$ J (Isrealachvili, 1985; Vincent and Jean Marc, 2007)).

The electrostatic forces with constant surface potential for the spherical part and the conical part of the tip are given by:

$$F_{TS}^{S} = 4\pi\varepsilon_0\varepsilon\Phi_T\Phi_S(a_0e^{-\kappa D} - a_1^{-\kappa L_1}) - 2\pi\varepsilon_0\varepsilon(\Phi_T^2+\Phi_S^2)(a_1e^{-2\kappa D} - a_3^{-2\kappa L_1}) \quad (4)$$

where Φ_T and Φs are the surface potentials of AFM tip and surface, $a_0 = \kappa R-1$, $a_1 = \kappa R\cos\alpha-1$, $a_2 = a_0+0.5$, and $a_3 = a_1+0.5$.

$$F_{TS}^{C} = \frac{4\pi\varepsilon_0\varepsilon\kappa}{\tan\alpha}\left[b_1\Phi_T\Phi_Se^{\kappa L_1} - b_2\frac{(\Phi_T^2+\Phi_S^2)}{2}e^{2\kappa L_1}\right] \quad (5)$$

The electrostatic force with constant surface charge density for the spherical part and the conical part of the tip is given by:

$$F_{TS}^{S} = \frac{4\pi}{\varepsilon_0\varepsilon\kappa^2}\sigma_T\sigma_S(a_0e^{-\kappa D} - a_1e^{-\kappa L_1}) + \frac{2\pi}{\varepsilon_0\varepsilon\kappa^2}(\sigma_T^2+\sigma_S^2)(a_2e^{-2\kappa D} - a_3e^{-2\kappa L_1}) \quad (6)$$

$$F_{TS}^{C} = \frac{4\pi}{\varepsilon_0\varepsilon\kappa\tan\alpha}\left[b_1\sigma_T\sigma_Se^{-\kappa L_1} + b_2\frac{(\sigma_T^2+\sigma_S^2)}{2}e^{-2\kappa L_1}\right] \quad (7)$$

where σ_T and σ_s are the surface charge densities of AFM tip and surface, respectively,

$$b_1 = \left[R\sin\alpha - \frac{D+R(1-\cos\alpha)}{\tan\alpha}\right] + \frac{1}{\tan\alpha}\left[\left(L_1+\frac{1}{\kappa}\right)\right] \quad (8)$$

$$b_2 = \left[R\sin\alpha - \frac{D + R(1-\cos\alpha)}{\tan\alpha}\right] + \frac{1}{\tan\alpha}\left[\left(L_2 + \frac{1}{2\kappa}\right)\right] \quad (9)$$

The total electrostatic force between the tip and the substrate can then be obtained for either constant surface potential or constant surface charge density by the sum of these two parts:

$$F^{e} = F^{S}_{TS} + F^{C}_{TS} \quad (10)$$

The total DLVO force for the system with geometry shown in Figure 2 is given by adding the electrostatic force and the van der Waals force:

$$F = F^{e} + F^{vdw} \quad (11)$$

The surface potential is calculated from the surface-charge density using the Grahame equation (Isrealachvili, 1985) which is expressed as

$$c_0 = c_\infty \exp\left(-\frac{z_i e\Psi}{kT}\right) \quad (12)$$

$$c_0 - c_\infty = \frac{\sigma^2}{2\varepsilon\varepsilon_0 kT} \quad (13)$$

$$c_\infty = \frac{\kappa\varepsilon\varepsilon_0 kT}{e^2 z^2} \quad (14)$$

where Ψ is the surface potential, k is the Boltzmann constant, T is the absolute temperature, e is the electronic charge, z is the valence of the ions, c_0 is the ionic concentration at the surface, and c_∞ is the ionic concentration in the bulk at $x = \infty$ where $\Psi(\infty) = 0$.

RESULTS AND DISCUSSION

Zeta potential of chlorite measured by electrophoresis

The results of the zeta potentials of chlorite particles determined by electrophoresis (Figure 3) indicate that the IEP of chlorite is ~pH 5.5, a result which is in good agreement with the value given by Fornasiero and Ralston (2005). According to the crystalline structure of chlorite, both a mica-like face and a brucite-like face can be exposed at a particle surface and contribute to the surface-charge density of chlorite. Usually, mica-group minerals have an IEP of <pH 2, whereas brucite has a larger IEP which is ~pH 11 (Pokrovsky and Schott, 2004; Fuerstenau *et al.*, 2007). The IEP measured for chlorite in the present study is close to the average value of the IEP for mica and brucite. Note, however, that the IEP determined from electrophoretic mobility may be misleading due to the basic assumption in the Smoluchowski model that the particles are of spherical shape (Butt *et al.*, 2003) and of homogeneous surface-charge density (Nalaskowski *et al.*, 2007; Wypych and Satyanarayana, 2004). Chlorite is known to be a mineral with platy morphology and anisotropic surface characteristics. The surface charge at the two basal planes (mica-like face and brucite-like face) and at the edge surface can be different. Therefore, the zeta potential obtained from electrophoresis with the Smoluchowski model may not reflect the surface potential at the shear plane. So far, no model is available to describe the

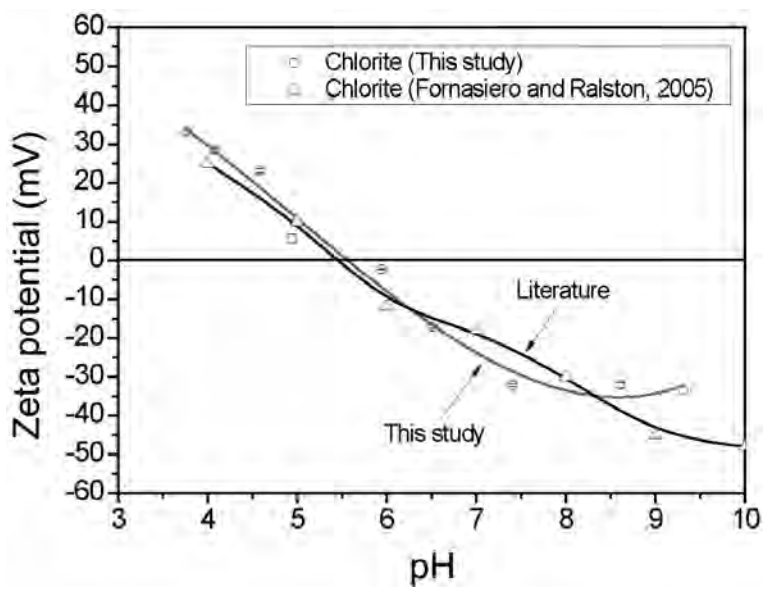

Figure 3. Zeta potential of chlorite as a function of pH measured in 1 mM KCl by the electrophoresis method compared with the results reported in the literature (Fornasiero and Ralston, 2005). The error bars denote the standard deviation of multiple surface force measurements.

movement of platy-shaped particles with anisotropic surface-charging characteristics. Hence, the anisotropic surface charge of chlorite needs to be characterized using other techniques.

Interaction forces at chlorite basal-plane surfaces

Surface forces were measured at both the chlorite mica-like face surface and the brucite-like surface. The chlorite basal plane surface (Figure 4a) was determined to be the mica-like face by subsequent AFM surface-force measurements. The root-mean-square surface roughness for the chlorite basal-plane surface was determined to be from 0.1 to 0.4 nm. This roughness suggests that the chlorite basal-plane surfaces are smooth enough to satisfy the requirements of AFM surface force measurement.

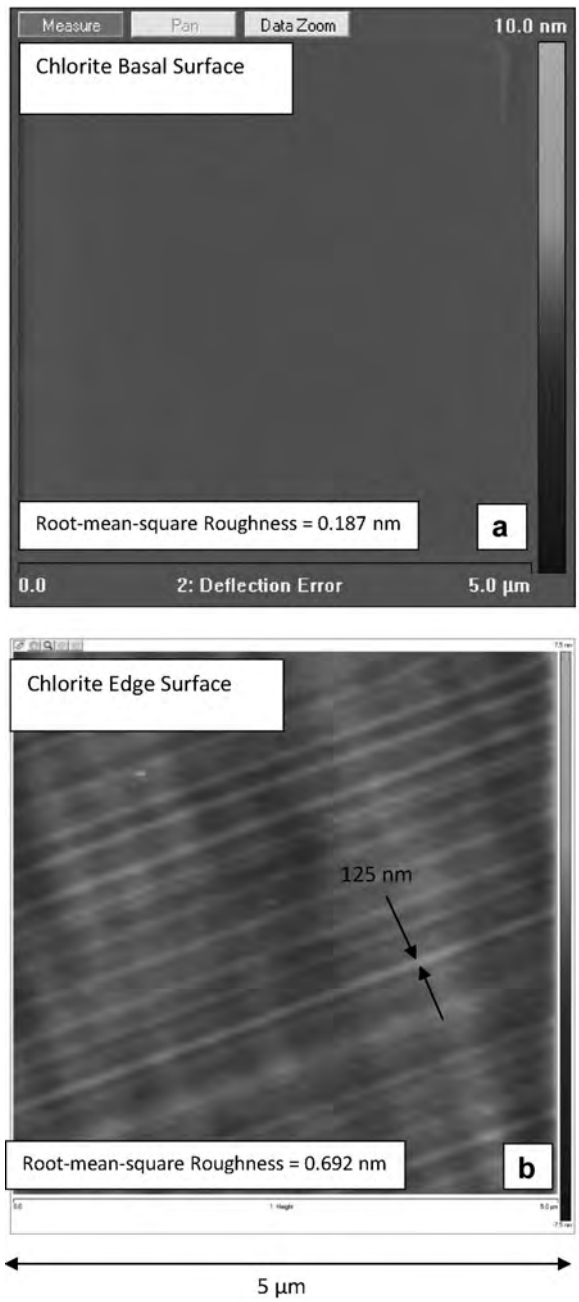

Figure 4. Typical AFM image of chlorite mica-like basal plane surface (a) and edge surface (b).

The approaching surface-force curves were collected at both types of basal planes of chlorite. The typical interaction forces between the silicon nitride AFM tip and the chlorite mica-like surface in 1 mM KCl solutions with varying pH values are shown in Figure 5. A 10−20% variation on the magnitude of the surface forces was observed during the AFM surface-force measurements. The open circles on the graphs represent experimental data, whereas the solid lines represent data calculated using the DLVO theoretical model. For the curve fitting, the surface-charge densities of the silicon nitride AFM tip at different pH values were taken from the literature (Yan *et al.*, 2011). The IEP of the silicon nitride AFM tip is noted to be ~pH 4.0 (Yin and Drelich, 2008). Thus, the tip should be negatively charged at pH 5.6, 8.0, and 9.0. The experimental surface-force curves are in good agreement with the curves calculated from the theoretical model at separation distance >5 nm (Figure 5). However, at shorter separations, the theoretical fitting curves deviated from the experimental curves. The strong repulsive interactions recorded at separations below 1−2 nm might be attributed to a non-DLVO force known as the 'hydration force' which was not taken into account in the theoretical model used in the present study. Electrostatic interaction is usually observed at separation distances of 5 to 30 nm. Long-range repulsive forces were observed at all three pH conditions (Figure 5). The magnitude of the repulsion increased gradually with an increase in pH. The results indicate that chlorite mica-like face is negatively charged in this pH range and the IEP of the chlorite mica-like face is <pH 5.6.

In contrast to the mica-like face of chlorite, attractive interactions dominate the brucite-like face of chlorite at all three pH values (5.6, 8.0, and 9.0), suggesting that it is positively charged in this pH range and its IEP should be >pH 9 (Figure 6).

INTERACTION FORCES AT CHLORITE EDGE SURFACES

A representative AFM image of the chlorite edge surface is shown in Figure 4b. The root-mean-square surface roughness was determined to be 0.692 nm, confirming that the ultramicrotome cutting technique is capable of creating a 'molecularly smooth' flat surface which can be used for AFM surface-force measurements. The pattern of lines arises from the chlorite sheets (Figure 4b). The distances between the lines were measured as 80−130 nm. Compared to the distances

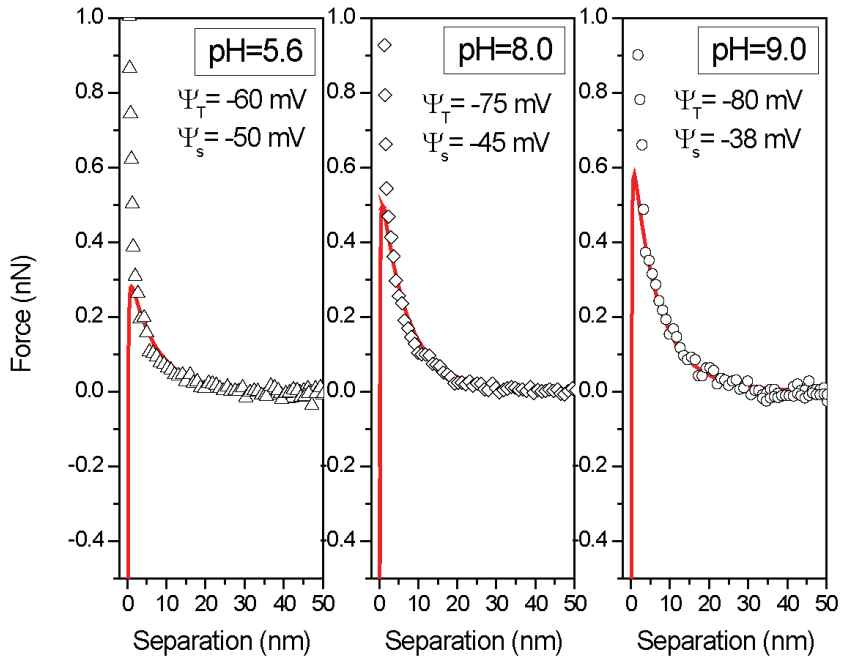

Figure 5. Interaction forces between a silicon nitride AFM tip and chlorite mica-like basal plane surface in 1 mM KCl at pH 5.6, 8.0, and 9.0. The solid lines represent the theoretical DLVO fit. Ψ_T is the surface potential of the silicon nitride AFM tip and Ψ_S is the surface potential of the chlorite mica-like surface.

between repeating chlorite units, which is ~1.4 nm, the results suggest that there are ~60 to 90 repeating units between two lines.

The surface-force measurements were performed at the well prepared chlorite edge surface using AFM. Representative surface-force curves between the silicon

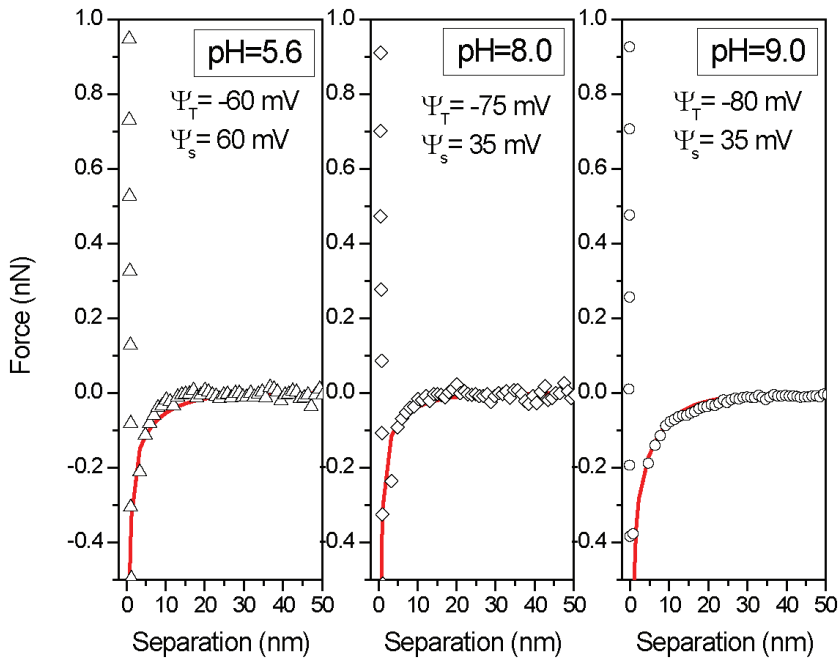

Figure 6. Interaction forces between a silicon nitride AFM tip and chlorite brucite-like basal plane surface in 1 mM KCl at pH 5.6, 8.0, and 9.0. The solid lines represent the theoretical DLVO fit. Ψ_T is the surface potential of the silicon nitride AFM tip and Ψ_S is the surface potential of the chlorite brucite-like surface.

nitride AFM tip and chlorite edge surface were acquired in 1 mM KCl with varying pH values (Figure 7).

The experimental data were fitted with the theoretical DLVO model and good agreement was observed. Though the DLVO model applies to a planar surface of infinite extent with uniform point charges, few substrates satisfy this condition. The fact that a nano-sized probe was used, which was smaller than the width of edges, should justify this approximation. This condition is not perfect as the tip is slightly smaller than the width of the edge but as a first approximation is acceptable. At pH 5.6 and 8.0, attractive interaction forces were found between the AFM tip and chlorite edge surface. When the pH value of the electrolyte was increased to pH 9.0, the interaction force became repulsive. As the silicon nitride AFM tip is negatively charged at all three pH conditions, these surface force results suggest that the chlorite edge surface is pH dependent. The chlorite edge surface is positively charged below pH 8.0 and negatively charged above 9.0, indicating that the IEP of the chlorite edge lies between pH 8.0 and pH 9.0.

Surface potential and surface-charge density

The magnitudes of surface-charge density and surface potential of the chlorite mica-like surface and brucite-like surface (Figure 8) were determined from fitting the experimental force curves to the DLVO model. At pH 5.6, 8.0, and 9.0, the mica-like face of chlorite is negatively charged, with the surface potential between −45 mV and −50 mV and the surface charge density between −5.8 mC/m^2 and −6.6 mC/m^2. The surface potential of the chlorite mica-like face was noted to be nearly constant over the pH range which confirms that the pH-insensitive surface-charge density is attributed to the presence of a permanent and fixed amount of isomorphous substitution of Si^{4+} by Al^{3+} in the chlorite mica-like face. The silica tetrahedral face, which has a hexagonal ring structure, is known to be difficult to protonate (Avena *et al.*, 2003). The charge deficiency caused by lattice substitution is, therefore, believed to account for the permanent negative charge on this basal plane. The results from characterization of the surface charging of muscovite and talc basal planes using AFM (Yan *et al.*, 2011) are compared in Figure 8b. Similar to the chlorite mica-like face, the basal planes for talc and muscovite are also negatively charged and the surface potentials are nearly constant. These results confirm the pH-insensitive nature of the silica tetrahedral face for phyllosilicate minerals. Note that the magnitude of the surface potentials for the basal planes of these three phyllosilicates are in a sequence of Ψ(talc) < Ψ(chlorite mica-like) < Ψ(muscovite), which may be due to the different levels of isomorphous substitution. In a perfect muscovite lattice, the isomorphous substitution should be 25%. In contrast, talc has a much smaller amount of isomorphous substitution (0.01−3.4%), which results in a smaller surface potential (Deer *et al.*, 1997). In the case of chlorite, Al^{3+} could be present in both the mica-like face and in the brucite-like face by isomorphous substitution. Thus, the level of substitution in the mica-

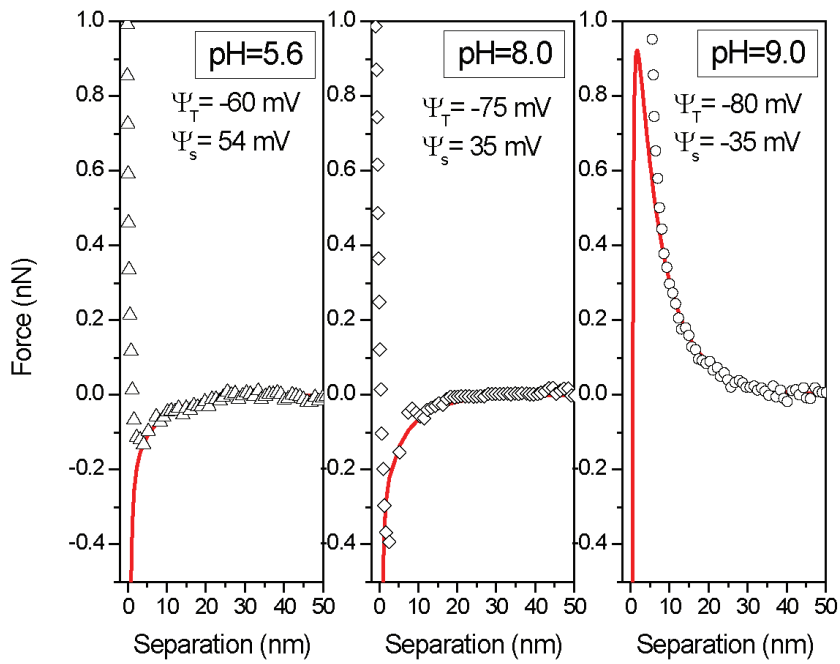

Figure 7. Interaction forces between a silicon nitride AFM tip and chlorite edge surface in 1 mM KCl at pH 5.6, 8.0, and 9.0. The solid lines represent the theoretical DLVO fit. Ψ_T is the surface potential of the silicon nitride AFM tip and Ψ_S is the surface potential of the chlorite edge surface.

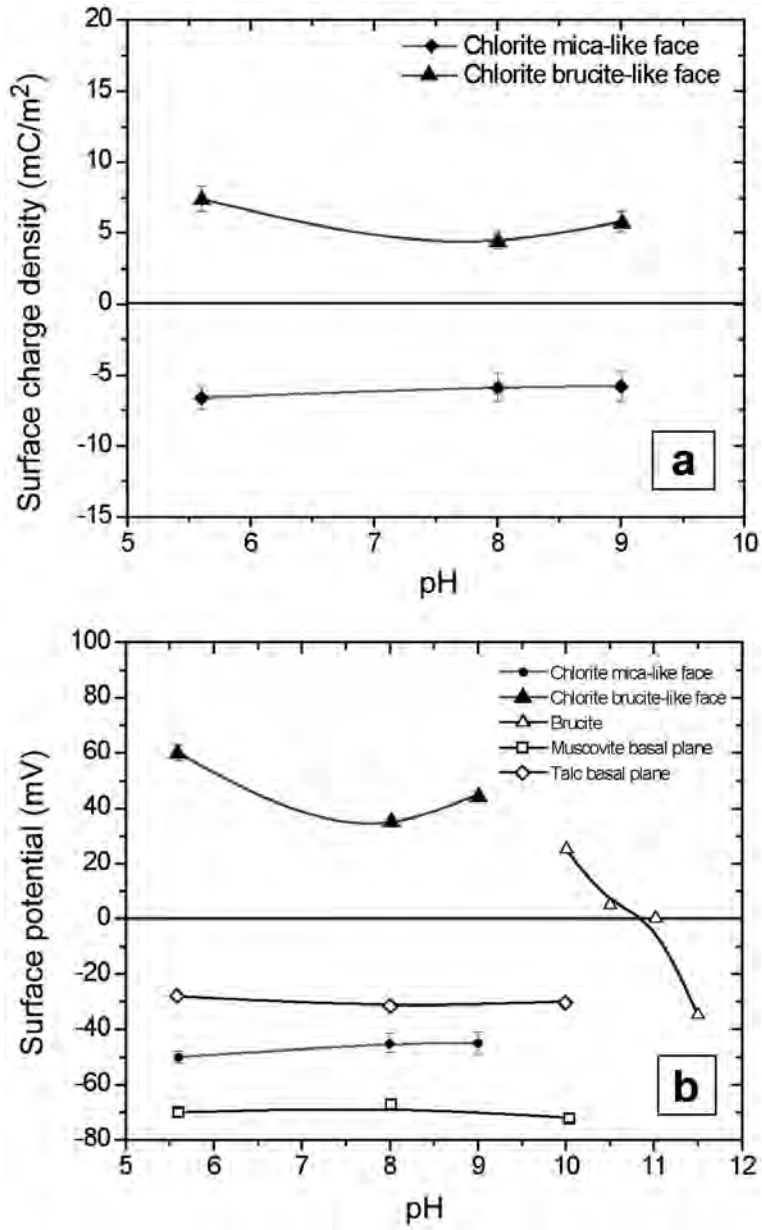

Figure 8. Surface charge density (a) and surface potential (b) of the chlorite mica-like basal plane surface and brucite-like basal plane surface as a function of pH. The error bars denote the standard deviation of multiple surface force measurements. The surface potentials of chlorite basal planes (Solid symbols) are compared with the literature results (plot with open symbols) (Pokrovsky and Schott, 2004; Yan *et al.*, 2011).

like face is difficult to estimate. Moreover, from the elemental composition analysis, note that other cations including Fe^{2+}, Cr^{2+}, and Na^{+} are also involved in the chlorite lattice. These cations will also affect the magnitude of the surface potential.

The surface-charge densities and surface potentials of the chlorite brucite-like face are also plotted in Figure 8. At all three pH values, the brucite-like face of chlorite is positively charged. The surface potentials are in a range of 35 to 60 mV and the surface-charge densities are between 4.5 and 7.5 mC/m^2. A slight decrease in surface potential with increasing pH was observed, suggesting that the brucite-like face of chlorite is slightly pH-dependent. This finding suggests that, compared with mica-like basal planes, the brucite-like basal planes are less resistant to hydrolysis, leading to pH-dependent ionization of hydrolyzed surface magnesium ions. In order to compare the surface charging behavior of chlorite brucite-like face and brucite, the surface potential of brucite particles from electrophoresis

measurements reported by Pokrovsky and Schott (2004) are also shown in Figure 8b. Below pH 11.0, the brucite particles are positively charged, which is similar to the chlorite brucite-like face. Nevertheless, as mentioned previously, the Al^{3+} cations are also present in the chlorite brucite-like sheet. Thus, the IEP of the chlorite brucite-like face could be <pH 11.0.

The surface-charge density and surface potential of the chlorite edge surface were measured in 1 mM KCl at pH 5.6, 8.0, and 9.0 (Figure 9). At pH 5.6 and pH 8.0, the surface potentials of the chlorite edge surface are positive with magnitudes of 54 and 35 mV, respectively. When increasing the pH value to pH 9.0, the surface potential is reversed to negative and the surface potential is −35 mV. These results suggest that the chlorite edge surface is strongly pH-dependent and the IEP is estimated to be ~pH 8.5.

The surface potentials of the chlorite edge surface are compared with the surface potential values of muscovite and talc edge surfaces from the literature (Yan *et al.*,

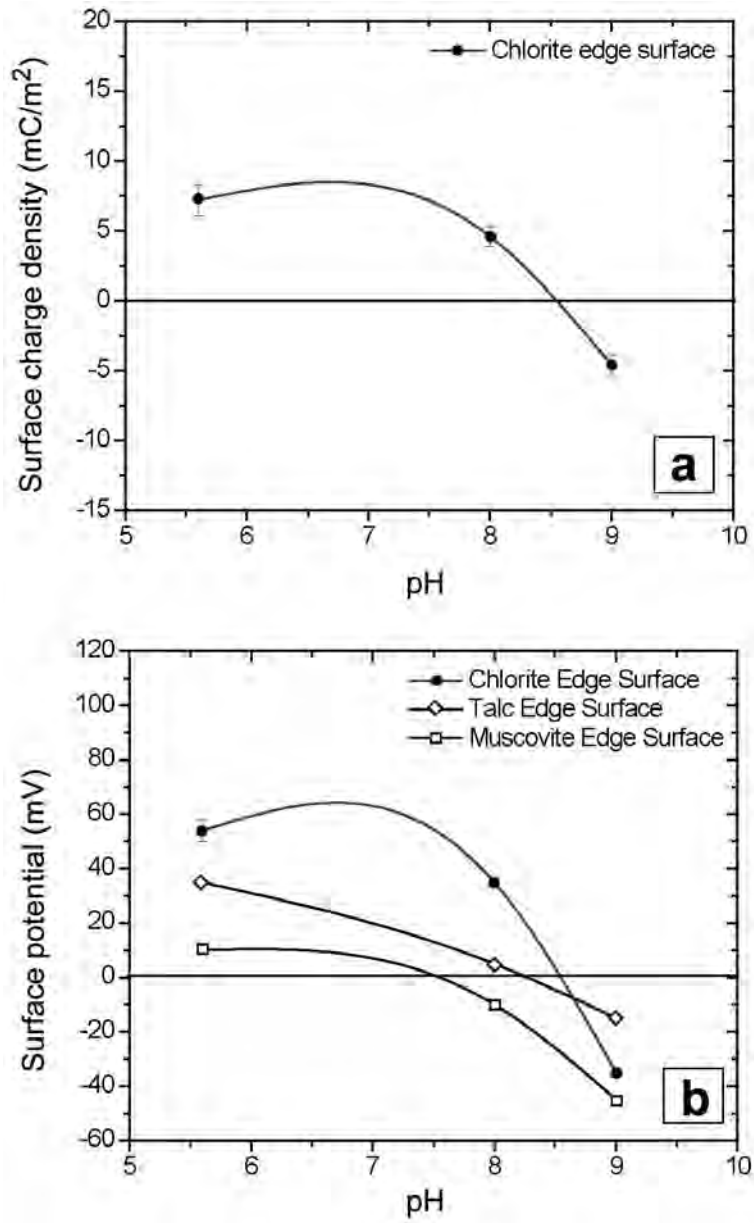

Figure 9. Surface charge density (a) and surface potential (b) of the chlorite edge surface as a function of pH. The error bars denote the standard deviation of multiple surface force measurements. The experimental results (plot with solid circle) are compared with the surface potentials of talc and muscovite edge surfaces from the literature (plot with open circle and open square) (Yan *et al.*, 2011).

2011) (Figure 9b). Note that the IEP of the chlorite edge surface (~pH 8.5) is greater than the IEP of muscovite edge surface (~pH 7.5) and close to the IEP of talc edge surface (~pH 8.1). The charges at the edge surface of phyllosilicates arise mainly from the protonation and deprotonation reactions of the broken bonds of the surface groups. The general reaction formula is given as:

$$A^x + H^+ = AH^{x+1}$$

where A^x represents a functional group with a charge of x and AH^{x+1} is the protonated form. Based on a Multi-Site Complexation model (MUSIC), the proton affinity of different surface groups at both basal and edge surfaces of phyllosilicates were studied (Nagashima and Blum, 1999; Avena *et al.*, 2003). The intrinsic protonation constants, K_H, of surface functional groups were calculated to describe the proton affinity (Table 1). Those authors found that the protonation constant for the siloxane group is very small (log K_H ~ −6.9), suggesting that the siloxane structure is difficult to protonate. On the contrary, the surface functional groups at edge surfaces are much more reactive and can be protonated in the normal pH range. The groups of Mg-$OH^{2/3-}$ and Al-$OH^{1/2-}$ were found to be the dominant charging groups at phyllosilicate edge surfaces and can be protonated and become positively charged through the following reactions:

$$MgOH^{-2/3} + H^+ = MgOH_2^{+1/3}$$
$$AlOH^{-1/2} + H^+ = AlOH_2^{+1/2}$$

The fact that the protonation constant for Mg-$OH^{2/3-}$ is greater than for Al-$OH^{1/2-}$ (Table 1) indicates that Mg-$OH^{2/3-}$ is easier to protonate (Avena *et al.*, 2003; Tournassat *et al.*, 2004) and also explains why brucite has a larger IEP than gibbsite. As the edge surfaces of muscovite and talc contain the Al-$OH^{1/2-}$ groups and Mg-$OH^{2/3-}$ groups, respectively, the talc edge surface should have a larger IEP than the muscovite edge surface. This theoretical analysis has been confirmed by the experimental AFM results from the literature (Yan *et al.*, 2011).

In the case of the chlorite edge surface, Mg-$OH^{2/3-}$ is the main charging functional group, although a small amount of Al-$OH^{1/2-}$ is present in the brucite-like sheet. Theoretically, the ratio of Mg to Al in the chlorite octahedral sheet (both mica-like layer and brucite-like sheet) is 5:1. Instead of interlayer cations, chlorite has an additional brucite-like sheet between two mica-like layers, leading to a larger amount of Mg-$OH^{2/3-}$. Based on the crystal structure information, the ratio of the amount of Mg-$OH^{2/3-}$ in talc to that in chlorite is 3:4. Therefore, the chlorite edge surface is expected to be more positively charged at a given pH.

Chlorite can float with both cationic collectors (alkyl amines, alkyl ether amines, and quaternary ammonium salts) and anionic collectors (alkyl phosphonic acids, oleic acids, and xanthate) (Silvester *et al.*, 2011). Although the results from electrophoresis measurement cannot fully explain these flotation results, the establishment of the anisotropic surface charging of chlorite may help to explain the observed flotation results. In a study on the flotation of chlorite as a single mineral system, chlorite was found to be floated using lauryl amine with the greatest extent of recovery (~50%) at between pH 7 and pH 9 (Zheng *et al.*, 2009). Chlorite can also be floated using oleic acid. The recovery of chlorite at pH 8 with oleic acid is similar to that for lauryl amine (~50%), suggesting that both the cationic collector and anionic collector can adsorb at the chlorite surface at pH 8. According to the results of this study, the chlorite mica-like basal plane surface is negatively charged at pH 8, whereas the brucite-like basal surface and the edge surface are positively charged. Therefore, under these conditions the adsorption of the lauryl amine could occur at the mica-like surface and the oleic acid could adsorb at the brucite-like basal plane surface and at the edge surface, leading to flotation by either cationic or anionic surfactants (collectors), as observed experimentally. Clearly, the fundamental information on anisotropic surface-charge characteristics of chlorite derived from this study will permit design of more effective flotation reagent systems for chlorite-containing mineral systems.

Table 1. The protonation constants (log K_H) of the surface groups in phyllosilicates (Yan *et al.*, 2011; Avena *et al.*, 2003; Tournassat *et al.*, 2004).

Surface group	Location	Log K_H^{int}
Al_2–OH	Basal surface	−1.5
Al_2–O^{1-}	Basal surface	12.3
Si_2-O	Basal surface	−16.9
SiAl–O^x	Edge surface	−16.9 to 12.3
Si–OH	Edge surface	−1.9
Si–O^{1-}	Edge surface	11.9
Al–$OH^{1/2-}$	Edge surface	7.9 to 9.9
Mg–$OH^{2/3-}$	Edge surface	10.0
Si–O–Al–OH	Edge surface	7.2 to 7.7
Si–O–Mg–OH	Edge surface	9.8

SUMMARY

The surface-charge properties of chlorite, which is a mixed-layer phyllosilicate, were characterized by measuring the surface forces between a silicon nitride tip and the chlorite surfaces using AFM. The mica-like face and brucite-like face of chlorite were prepared by splitting a chlorite crystal along its natural cleavage plane (001). Moreover, the chlorite edge surface was created using the ultramicrotome cutting technique. Both the basal-plane surface and the edge surface have a surface roughness of <1 nm, which should satisfy the requirement for AFM surface-force measurements.

The surface-force measurements were conducted in 1 mM KCl at pH 5.6, 8.0, and 9.0. The measured surface forces were fitted with the theoretical DLVO model. The surface potential and surface-charge density for chlorite basal-plane surfaces and edge surfaces were then determined from the fitting curve. A significant difference in charging behavior was observed for the chlorite mica-like face and the brucite-like face. At all three pH conditions, the chlorite mica-like face was negatively charged with the IEP <pH 5.6. In contrast, the chlorite brucite-like face is positively charged in this pH range and the IEP was >pH 9.0.

Surface charging of the chlorite edge surface was also examined. The transition from positive charge to negative charge was observed between pH 8.0 and pH 9.0. From the curve fitting, the IEP of the chlorite edge surface was estimated to be pH 8.5. This value was slightly greater than the IEP for muscovite and close to the IEP of talc-edge surfaces, which may be due to the greater number of magnesium hydroxide groups at the chlorite edge. Note that the term chlorite represents a group of minerals and contains many types of minerals which have the same structure but different chemical compositions. Therefore, different surface characteristics for different types of chlorite minerals can be expected and the values of the surface-charge density and surface potential obtained here may not be applicable to all of the minerals in the chlorite group.

The anisotropic surface characteristics of chlorite were also demonstrated. The surface-charging behavior of the chlorite basal plane surfaces and the edge surface was established as a function of pH. The results from the present research further established a better understanding of the charging behavior for phyllosilicates. The results are expected to provide a fundamental foundation for solving flotation issues, including collector adsorption, slime coating, and particle interactions.

ACKNOWLEDGMENTS

Financial support for XY, JL, and JDM from the Division of Chemical Sciences, Geosciences and Biosciences, Office of Basic Energy Sciences, of the U.S. Department of Energy through Grant Number DE-FG03-93ER14315 is gratefully acknowledged. The authors express their appreciation to the Alberta Center for Surface Engineering and Science (ACSES) for their help with the XPS measurements and support for LY and ZX from the Natural Sciences and Engineering Research Council of Canada (NSERC) under the industry research chair program in Oil Sands Engineering.

REFERENCES

Alvarez-Silva, M., Uribe-Salas, A., Mirnezami, M., and Finch, J. A. (2010) The point of zero charge of phyllosilicate minerals using the Mular–Roberts titration technique. *Minerals Engineering.* **23**, 383–389.

Assemi, S., Nalaskowski, J., Miller, J. D., and Johnson, W.P. (2006) Isoelectric Point of Fluorite by Direct Force Measurements Using Atomic Force Microscopy. *Langmuir.* **22**, 1403–1405.

Avena, M.J., Mariscal, M.M., and De Pauli, C.P. (2003) Proton binding at clay surfaces in water. *Applied Clay Science.* **24**, 3–9.

Butt, H.J., Graf, K., and Kappl, M. (2003) *Physics and Chemistry of Interfaces*. Wiley-VCH, Weinheim, Germany.

Deer, W.A., Howie, R.A., and Zussman, J. (1997) Rock Forming Minerals. *2nd ed.; The Geological Society*: London, Vol. 2B.

Drelich, J., Long, J., and Yeung, A. (2007) Determining Surface Potential of the Bitumen-Water Interface at Nanoscale Resolution using Atomic Force Microscopy. *The Canadian Journal of Chemical Engineering.* **85**, 625–634.

Drelich, J. and Wang, Y.U. (2011) Charge heterogeneity of surfaces: Mapping and effects on surface forces. *Advances in Colloid and Interface Science*, **160**, 91–101

Fornasiero, D. and Ralston, J. (2005) Cu(II) and Ni(II) activation in the flotation of quartz, lizardite and chlorite. *International Journal of Mineral Processing*, **76**, 75–81.

Fuerstenau, M.C., Jameson, G., and Yoon, R.H. (2007) *Froth flotation: A Century of Innovation*. Society for Mining Extraction and Exploration, Colorado, USA.

Fuerstenau, D.W. and Pradip (2005) Zeta potentials in the flotation of oxide and silicate minerals. *Advances in Colloid and Interface Science*, **114–115**, 9–26.

Gupta, V. and Miller, J.D. (2010) Surface force measurements at the basal planes of ordered kaolinite particles. *Journal of Colloid and Interface Science*, **344**, 362–371.

Gupta, V., Hampton, M.A., Stokes, J.R., Nguyen, A.V., and Miller, J.D. (2011) Particle interactions in kaolinite suspension and corresponding aggregate structures. *Journal of Colloid and Interface Science*, **359**, 95–103.

Harvey, C.C. and Murray, H.H. (1997) Industrial clays in the 21st century: A perspective of exploration, technology and utilization. *Applied Clay Science*, **11**, 285–310.

Isrealachvili, J.N. (1985) *Intermolecular and Surface Forces*. Academic Press, New York.

Leroy, P., Tournassat, C., and Bizi, M. (2011) Influence of surface conductivity on the apparent zeta potential of TiO_2 nanoparticles. *Journal of Colloid and Interface Science*, **356**, 442–453.

Long, J., Li, H., Xu, Z., and Masliyah, J.H. (2006) Role of colloidal interactions in oil sand tailings treatment. *AIChE Journal*, **52**, 371–383.

Mular, A.L. and Roberts, R.B. (1966) A simplified method to determine the isoelectric point of oxides. *Transactions of the Canadian Institute of Mining and Metallurgy*, **69**, 438–439.

Murray, H.H. (1991) Overview – clay mineral applications. *Applied Clay Science*, **5**, 379–395.

Murray, H.H. (2000) Traditional and new applications for kaolin, smectite, and palygorskite: a general overview. *Applied Clay Science*, **17**, 207–221.

Murray, H.H. and Kogel, J.E. (2005) Engineered clay products for the paper industry. *Applied Clay Science*, **29**, 199–206.

Nagashima, K. and Blum, F.D. (1999) Proton adsorption onto alumina: extension of multisite complexation (MUSIC) Theory. *Journal of Colloid and Interface Science*, **217**, 28–36.

Nalaskowski, J., Drelich, J., Hupka, J., and Miller, J.D. (2003) Adhesion between hydrocarbon particles and silica surfaces with different degrees of hydration as determined by the AFM colloidal probe technique. *Langmuir*, **19**, 5311–5317.

Nalaskowski, J., Abdul, B., Du, H., and Miller, J.D. (2007) Anisotropic character of talc surfaces as revealed by streaming potential measurements, atomic force microscopy, molecular dynamics simulations and contact angle measurements. *Canadian Metallurgical Quarterly*, **46**, 227–236.

Pokrovsky, O.S. and Schott, J. (2004) Experimental study of brucite dissolution and precipitation in aqueous solutions: surface speciation and chemical affinity control. *Geochimica et Cosmochimica Acta*, **68**, 31–45.

Silvester, E.J., Bruckard, W.J., and Woodcock, J.T. (2011) Surface and chemical properties of chlorite in relation to its flotation and depression. *Mineral Processing and Extractive Metallurgy*, **120**, 65–70.

Sondi, I. and Pravdić, V. (1996) Electrokinetics of natural and mechanically modified ripidolite and beidellite clays. *Journal of Colloid and Interface Science*, **181**, 463–469.

Sondi, I., Bišćan, J., and Pravdić, V. (1996) Electrokinetics of pure clay minerals revisited. *Journal of Colloid and Interface Science*, **178**, 514–522.

Sondi, I., Milat, O., and Pravdić, V. (1997) Electrokinetic potentials of clay surfaces modified by polymers. *Journal of Colloid and Interface Science*, **189**, 66–73.

Tournassat, C., Ferrage, E., Poinsignon, C., and Charlet, L. (2004) The titration of clay minerals II. Structure-based model and implications for clay reactivity. *Journal of Colloid and Interface Science*, **273**, 234–246.

Veeramasuneni, S., Yalamanchili, M.R., and Miller, J.D. (1996) Measurement of interaction forces between silica and α-alumina by atomic force microscopy. *Journal of Colloid and Interface Science*, **184**, 594–600.

Vincent, M.-M. and Jean Marc, D. (2007) Immersion of solids. *Encyclopedia of Surface and Colloid Science, Second Edition*, Taylor & Francis, pp. 2892–2905.

Vrdoljak, G.A., Henderson, G.S., Fawcett, J.J., Wicks, F.J., and Frederick, J. (1994) Structural relaxation of the chlorite surface imaged by the atomic microscope. *American Mineralogist*, **79**, 107–112.

Wallqvist, V., Claesson, P.M., Swerin, A., Schoelkopf, J., and Gane, P.A.C. (2006) Interaction forces between talc and hydrophobic particles probed by AFM. *Colloids and Surfaces A: Physicochemical and Engineering Aspects*, **277**, 183–190.

Wypych, F. and Satyanarayana, K.G. (2004) *Clay Surfaces: Fundamentals and Applications.* Academic Press, New York.

Yan, L., Englert, A.H., Masliyah, J.H., and Xu, Z. (2011) Determination of anisotropic surface characteristics of different phyllosilicates by direct force measurements. *Langmuir*, **27**, 12996–13007.

Yin, X. and Drelich, J. (2008) Surface charge microscopy: Novel technique for mapping charge-mosaic surfaces in electrolyte solutions. *Langmuir*, **24**, 8013–8020.

Zhang, J., Yoon, R.-H., and Eriksson, J.C. (2007) AFM surface force measurements conducted with silica in CnTACl solutions: Effect of chain length on hydrophobic force. *Colloids and Surfaces A: Physicochemical and Engineering Aspects*, **300**, 335–345.

Zhao, H., Bhattacharjee, S., Chow, R., Wallace, D., Masliyah, J.H., and Xu, Z. (2008) Probing surface charge potentials of clay basal planes and edges by direct force measurements. *Langmuir*, **24**, 12899–12910.

Zheng, G., Liu, L., Liu, J., Wang, Y., and Cao, Y. (2009) Study of chlorite and its influencing factors. *Procedia Earth and Planetary Science*, **1**, 830–837.

(*Received 11 September 2012; revised 15 March 2013; Ms. 712; AE: A. Thompson*)